MECHANICAL BEHAVIOUR OF VISCOELASTIC MATERIAL WITH CHANGING MICROSTRUCTURE

SANJAY K. SINGH

MECHANICAL BEHAVIOUR OF VISCOELASTIC MATERIAL WITH CHANGING MICROSTRUCTURE

Sanjay K. Singh, B.E., M.E.

A thesis submitted to the School of Graduate
Studies in partial fulfillment of the
requirements for the degree of
Doctor of Philosophy

Faculty of Engineering & Applied Science
Memorial University of Newfoundland
September 1993

St. John's, Newfoundland, Canada

Abstract

The observed response of a crystalline and brittle material to stress is the result of various micromechanical activities inside the material at the grain, or, at the constituent element scale. These activities include microcracking, pore formation and collapse, grain-boundary sliding, and phase change. In this thesis, such microstructural changes, and their effect on the response of viscoelastic materials are presented with reference to the behaviour of ice during its interaction with a structure.

During ice-structure interaction, zones of high pressure are formed at the structure interface. Extensive microcracking and other microstructural changes such as recrystallization in the ice occur in these zones. When the cracks coalesce, cavities are formed between junctions of weakly connected grains. This finely crushed material is finally extruded from the structure interface. The behaviour of ice and its damage depend on the rate of loading, the degree of confinement, the density of microcracks, grain boundaries, cavities and other microstructures. To further understanding in this area, triaxial tests were carried out on ice at different initial microstructure.

The process of material modelling is guided by the framework of thermodynamics. The internal variable approach provides a powerful method of incorporating the microstructures into a continuum theory. The changes in microstructures such as cracks and grain boundaries are modelled by a generalized J-integral, while change in the porosity is modelled by an approximate solution for creeping solids. To describe the various changes in the material two theories are developed. In the first theory, solutions for nonlinear elastic media are extended to nonlinear viscoelastic media using a correspondence principle. The second theory for viscoelastic behaviour is based on a mechanical model with nonlinear elements. Three components of deformation, i.e., the elastic, the delayed elastic, and the viscous creep are separately identified, and their changes with the extent of damage are modelled. The first theory is more systematic and requires fewer parameters. Both of these theories provided good predictions for strength tests. The dilatation of the cracking polycrystalline ice and the porous crushed ice is also modelled by the mechanical model.

A series of plane-strain extrusion tests were analyzed to understand the flow properties of crushed ice. A closed-form solution is presented for the nonlinear and viscous flow of crushed ice, and a finite element solution is also presented for the flow of crushed ice that is also undergoing compaction. These analyses provided a good agreement to the extrusion tests.

Acknowledgments

The Author would like to express his gratitude to his supervisor Dr. Ian J. Jordaan, for his advice and encouragement. His excellent support and willingness to allow the author to pursue own research interests was very helpful. Special thanks are also to the members of the supervisory committee comprising Dr. Garry Timco, National Research Council of Canada and Dr. John Molgaard, Faculty of Engineering, for their support during this study.

The author would like to gratefully acknowledge the financial support from the School of Graduate Studies, and the Faculty of Engineering and Applied Science of Memorial University, National Research Council of Canada, and Natural Sciences and Engineering Research Council of Canada.

Special thanks are due to Mr. Barry Stone for suggestions and assistance in experiments, and Dr. R.F. McKenna and Dr. K.S.R. Prasad for general discussions from time to time. The assistance of the staff at the Centre for Computer Aided Engineering, and technical services are also acknowledged.

Finally thanks to all friends and relatives for their cooperation extended beyond the academic boundaries.

Contents

List of Figures

List of Tables

Notations

$\hat{(.)}$	Laplace Transform of the argument
$\Delta(.)$	increment value of the argument
$(.)^I$	argument in the inclusion of composite
$(.)^M$	argument in the matrix of composite
A, A_m	crack surface area
A_p	cross-section area of the piston of triaxial cell
a	crack length; radius of pore
a_0	initial crack length
a_d	shift factor in Schapery's formulation for nonlinear materials
a_{ij}	stiffness tensor in Biot's formulation
a_T	exponent in Sinha's delayed elastic formulation
b	constant in creep compliance $D_0 + D_1 t^b + D_2 t$; delayed elastic constant in Sinha's equation
b_{ij}	viscosity tensor in Biot's formulation
b'_{ij}	viscosity tensor in Schapery's formulation for nonlinear materials
c	porosity
c_1	constant in Sinha's delayed elastic formulation
$C(.)$	relaxation modulus
C_{ijkl}, C^M_{ijkl}	elastic stiffness tensor of the material and the matrix
$C_{ijkl}(.)$	relaxation modulus
CPI	Confining Pressure Intensifier
CTC	Conventional Triaxial Test
$D(.), D_n(.)$	creep compliance
D_0, D_1, D_2	constant in creep compliance $D_0 + D_1 t^b + D_2 t$
D_{ijkl}	elastic compliance
$D_{ijkl}(.)$	creep compliance
d	deformed diameter of the sample
d_0	initial diameter of the sample
E, E_0	Young's modulus of damaged and virgin material
E_k, E_{k0}	stiffness of Kelvin element for damaged and virgin material
E_p	Young's modulus of porous material
E_R	Schapery's reference modulus

e, e^e, e^d, e^c	von Mises equivalent strain $(2/3e_{ij}e_{ij})^{1/2}$ for total, elastic, delayed elastic and creep components
e_{ij}	deviatoric strain tensor
e^e_{ij}	deviatoric pseudo-strain tensor
F	empirical function of time and stress
$f(.)$	function of the argument
F_i	body force per unit volume
f_1, f_2	constants
f_3	a function of confining pressure and the properties of the crack tip
f_m	thermodynamic force
G, G_0	shear modulus of damaged and virgin material
G_m	energy release rate
g, g_e	measure of accumulated damage in terms of stress and strain
h	length of sample in triaxial tests; half thickness of crushed ice layer
h_0	initial length of sample in triaxial tests
HC	Hydrostatic Compression
J	generalized J-integral
$J_D(.), J_V(.)$	creep and bulk compliances
K, K_0	bulk modulus of damaged and virgin material
k	exponent in crack growth
L	empirical function of time and stress; half width of crushed ice layer
L_p	displacement of piston in triaxial cell
LVDT	Linear Variable Displacement Transducer
MSP	modified superposition principle
n	power-law creep exponent
n_j	unit normals
N	cracks density per unit volume
p	hydrostatic pressure; pressure
p_0	pressure at exit in extrusion problem
p_a	atmospheric pressure
p_m	average pressure on the structure due to ice loading
q	stress power in the damage kinetics
Q	heat
Q_j	generalized forces
q_j	generalized displacement
r	exponent in power-law stress-strain relation
r, θ, ϕ	spherical coordinate
r_1	a constant to define crack tip properties f_3
R	radius of the matrix surrounding a pore
RST	Radial Strain Transducer

S_{ijkl}	Eshelby's tensor
S_m	microstructural parameters
S, S_1	surface of the representative volume
S, S_ϵ	microstructural parameter in terms of stress and strain
SS	Simple Shear
s	von Mises equivalent stress $(3/2s_{ij}s_{ij})^{1/2}$; frequency variable in Laplace transform; entropy production per unit mass
$\bar{s}$	effective von Mises stress in porous media
s_1	constant in Schapery's damage formulation
s_c	threshold stress for damage
s_d	von Mises equivalent stress in the dashpot of the Kelvin unit
s_I	entropy of the system
s_{II}	entropy of the surrounding
s_{ij}	deviatoric stress tensor
T	temperature in Kelvin
T_i	applied traction
t, t_i	time variables
t_f	failure time
U	internal energy
U_i	applied displacement vector
u_i	displacement vector
u_i^R	displacement vector in the reference elastic domain
u_r	radial displacement
V	representative volume; current volume of sample in triaxial tests
V_0	initial volume of sample in triaxial tests
V_i	volume of the confining pressure intensifier fluid
W	strain energy
W'	complementary energy
W^c	complementary pseudo-energy
W_F	body force potential
W_s	energy in irreversible processes
W_{se}	surface energy
W_T	Total energy
W'_T	Total complementary energy
W'_v	complementary energy due to pores
x	space vector
X_i	function of all quantities affecting irreversibility
α	triaxiality measure, $\alpha = 3/2(p/s)$
β_k	delayed elastic enhancement constant due to damage
β_s	creep enhancement constant due to damage
γ	shear strain
γ_m	surface energy per unit area of m^{th} crack

η, η_m	viscosity
η_k	viscosity of nonlinear dashpot in the Kelvin unit for given stress
δ_{ij}	Kronecker delta
ϵ, ϵ_1	axial strain
ϵ_3	radial strain
ϵ_0	constant in power-law stress-strain relation
ϵ_{ij}	strain tensor
$\bar{\epsilon}_{ij}$	averaged strain tensor in the regenerative volume V
ϵ_{ij}^R	strain tensor in the reference elastic domain
$\dot{\epsilon}_0$	constant in power-law creep relation
ϵ^c	secondary creep strain
ϵ^d	delayed elastic strain
ϵ^e	axial pseudo-strain
ϵ^{el}	elastic strain
ϵ_{ij}^e	pseudo-strain tensor
ϵ_{ij}^{el}	elastic strain tensor
ϵ_{ij}^p	irrecoverable strain tensor
ϵ_{k0}	primary creep reference rate
$\epsilon_r, \epsilon_\theta, \epsilon_\phi$	strains in spherical coordinates
ϵ_v	volumetric strain
λ	constant relating the damage function g to the damage parameter
λ_1	crack density parameter
λ_d	damage parameter in $E = E_0(1 - \lambda_d)$
ν	Poisson's ratio
ν_0	Poisson's ratio for virgin material
σ	uniaxial stress
σ'	proportionality constant
σ_0	constant in power-law stress-strain relation
σ_1	axial stress
σ_3	all-around pressure in triaxial test
σ_d	stress in the dashpot of Kelvin unit
σ_{ij}	stress tensor
$\bar{\sigma}_{ij}$	averaged stress tensor in the representative volume
σ_{ij}^R	stress tensor in the reference elastic domain
τ	time variable
ψ	reduced time

Chapter 1

Introduction

A theory of the deformation and flow of viscoelastic materials is essential in the understanding of a wide range of technical and scientific problems in areas such as soil and rock mechanics, powder and mineral processing, geophysics, and offshore engineering. Such problems include soil deformation, microcracking of rock, concrete, and flow of ice and snow avalanches. These examples may appear to be very disparate in nature involving different materials and phases, but the nature of microstructures and their mutual interaction is evident in all the problems.

In polycrystalline materials such as metals and ice in the undamaged state, crystals are packed together in a solid structure without visible pores or voids. Under deformation there is a little change in the density of the material. In materials with changing microstructures such as brittle and porous materials, density or porosity is sensitive to external loads or deformations. For example, for a given confining pressure, a loose material becomes compressed and its stiffness increases, while a dense material dilates and its stiffness degrades during axial loading (see Figure 1.1). Most of these materials never return to their initial state and show some time-dependent behaviour upon unloading. In materials at high homologous temperatures, e.g., ice

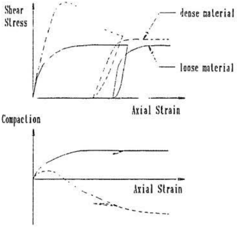

Figure 1.1: A typical deformation behaviour of particulate materials under cyclic loading.

and snow, the deformation at both loading and unloading is history-dependent.

Modelling of these aspects in a structured-continuum is a major task if the model parameters are required to be physically sound. In the present work, investigations are carried out in this direction. In this chapter, after outlining the objectives, material behaviour is reviewed in detail. A summary of the analysis procedure is presented, and finally the organization of the thesis is discussed.

1.1 Objective

In cold regions ice forces may form the most severe load case for ships and marine structures. During the process of ice-structure interaction, ice fails in brittle manner by continuous crushing and non-simultaneous failure by splitting, spalling and buckling. Polycrystalline ice near a structure undergoes extensive damage and crystals are broken into discrete pieces. The spalling of ice results in the formation of high

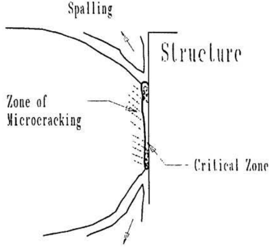

Figure 1.2: Ice-Structure Interaction.

pressure zones from which crushing and extrusion occur. The crushed particles form an interfacial layer between the intact ice mass and the structure (Figure 1.2). The thickness of this layer may vary spatially depending on the structure stiffness, ice inhomogeneity and velocity of the interaction, and it is associated with the ice forces and their variation (Jordaan and Timco, 1988; Singh et al., 1990).

Ice is a viscoelastic material, and the change in its microstructures such as cracking in polycrystalline ice, and sintering in snow and crushed ice, is history dependent. Similar behaviour can be observed in cracking of rocks, concrete, and porous materials such as clay and mineral powders. The behaviour of such materials depends on the current state of their microstructures and their change during the deformation. The objective of this thesis is to present a physically based model to describe changes during the deformation in the microstructures such as cracks and pores, in the framework of continuum mechanics.

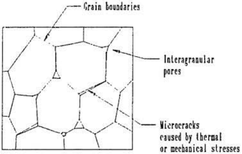

Figure 1.3: Microstructural features of polycrystalline materials

1.2 Review of Material Behaviour

1.2.1 Brittle Materials

In polycrystalline materials each grain is nearly perfect and meets its neighbors at grain boundaries. It may contain some flaws such as pores and microcracks (Figure 1.3). Such flaws weaken the material. When the material is stressed, some energy is stored due to the elasticity of material and in new surfaces, usually created at the flaws due to stress concentrations, while most of it dissipates due to friction at crack faces and in other inelastic deformations (Jordaan and McKenna, 1989, 1991). In a ductile material, these flaws increase the ductility of the material; whereas in a brittle material, brittleness is increased.

In tension, growth of a critical flaw is unstable. Under compression, cracks are initially less prone to propagate and the growth is stable. Many ductile and brittle materials such as copper and mild steel can fail in compression by the formation of tensile cracks normal to the direction of applied compression (Nemat-Nasser, 1989; Ashby and Hallam, 1986; Schulson, 1990). This is because of development of wing-cracks on pre-existing flaws in the material. At advanced stages of cracking, the

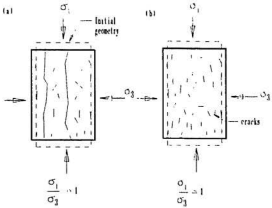

Figure 1.4: Failure in compression of a brittle material at (a) low and (b) high confining pressures.

loading rate and other environmental factors influence this process.

At low confining pressures, the crack growth is usually along the major principal axis (Figure 1.4a). Sometimes it may be localized along the maximum shear stress plane, while at high pressures such localization is suppressed, and cracking is uniformly distributed throughout the material (Figure 1.4b). Such uniformly cracked material under high pressure is essentially an isotropic and homogeneous ductile material. With an increase in the confining pressure, the strength and ductility of the material increases while the dilatation decreases (Figure 1.5a). In a rate-sensitive material, strength increases and the ductility decreases with an increase in the rate of loading (Figure 1.5b).

Elliott and Brown (1985) studied a highly porous limestone under confining pressures up to 30 MPa and observed similar changes in the material behaviour. At low confining pressures the failure was brittle and the material showed dilatation, which changed to ductile compaction by continuous pore collapse for high confinement.

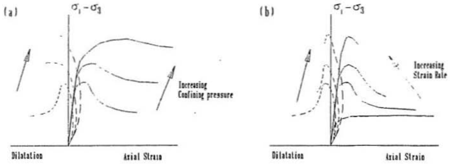

Figure 1.5: Effect of (a) confining pressure and (b) the rate of loading on the material behaviour.

1.2.2 Particulate Materials

Lade (1988) reviewed mechanical properties of frictional materials, and observed that stress and strain-rate are not co-axial at low stress levels. He also observed the transition to coincidence of strain-rate and stress axes at high stress levels. This suggests that frictional materials may behave like metals at high stresses. The inelastic deformation of frictional materials is dependent on the stress-path and its initial fabric. Oda (1972) and Oda et al. (1980) studied initial fabric and its change during the deformation of sand. The word fabric denotes the local granular structure, defined as the spatial arrangement and contact areas of solid particles and associated voids. The original distribution of fabric tends towards the direction of maximum principal stress. Rowe (1962) studied rigid spherical particles in contact and observed that strength and dilatancy behaviour of such an assemblage when sheared, depends on inter-particle friction, and the geometrical angle of packing that forms the initial fabric in the material. The path-dependence is more pronounced at high stress levels,

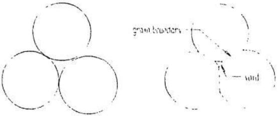

Figure 1.6: Sintering of grains

where inelastic strains are relatively large.

In materials at high homologous temperatures such as snow and ice, the densification rate is largely influenced by the temperature apart from the pressure dependency (Abele and Gow, 1975; Fukue, 1979). Ice grains or blocks stick together by neck growth while in contact (see Figure 1.6) and form a matrix of segregated material. The driving mechanism for this process is the surface energy available; this energy is larger for smaller grain size. The neck growth reduces the surface area, and thus the surface energy, and causes the material to compact. The process of sintering increases with the duration of loading and the amourt of applied hydrostatic pressure (Maeno and Ebinuma, 1983). The ambient temperature and the rate of loading also have a significant influence on such deformations. Under low rates the rheological properties of the material become important.

Gale et al. (1987) performed triaxial tests on particulate ice, which was isotropically compressed for a few hours, and observed a bi-linear deviatoric stress-strain behaviour. The initial branch rises rapidly and suddenly a break-over stress is reached followed by a hardening ductile phase. The break-over stress is highly dependent on the sustained confining pressure. Such brittle break-over is associated with the breaking of sintered bonds and cannot be interpreted as the yield stress of the bulk material. Gale et al. also compared the behaviour of crushed ice and loose sand.

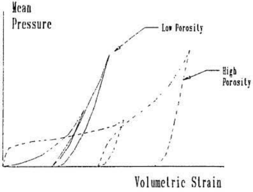

Figure 1.7: Compressible behaviour for materials of (a) low and (b) high porosities.

Both materials displayed broad similarity except for the break-over process. Steel et al. (1991) studied the effect of the rate of loading, temperature, and the confinement in triaxial tests on spray ice, and observed that the ductility of the material increases with an increase in temperature and confinement, and decreases with the rate of loading (Figure 1.5). Under high confining pressures sand also shows decrease in friction with increase in pressure (Vesic and Clough, 1968).

The volumetric behaviour of materials of various porosities is shown in Figure 1.7. In low porosity materials where the porosity is mainly due to microcracks, the loading and unloading curve is strongly nonlinear, and the deformation is largely recoverable (Johnson and Green, 1976). For materials of high porosities, pores first collapse and microcracks form at the grain-boundaries. These materials often show two peaks in strength tests.

Under very large confining pressure, particulate ice is expected to lose its discrete nature, and behave as polycrystalline ice. The grain size distribution also has significant effect on the failure mode. In a gap-graded particulate material, crushing of the grains occurs, while in a well-graded material, the behaviour is ductile at high pressures (Feda, 1982). The reduction in grain size increases the amount of surface energy, which in turn increases sintering.

1.3 Approach

During ice-structure interaction large local stresses may develop. In medium-scale indentation tests (Frederking et al., 1990), local stresses as high as 50 MPa were observed. These stresses develop near the centre of the critical zones (Figure 1.2), and are the result of large confinement. This zone is produced by extensive cracking and fragmentation of ice. The material in this zone is fine-grained, contains pores and its density is less than that of the parent polycrystalline ice. Outside this zone, confining stresses are small and tensile stresses may develop because of the geometry of ice and structure, and non-simultaneous failure (spalling) may occur. Though spalling may result in the reduction of ice forces in the spalling region, the total force on the structure is largely regulated by the flow of crushed ice from the critical zones, and the crushing near it. This is because most of the load is carried by these zones.

To investigate the crushing process in ice-structure interaction, triaxial strength and creep tests were conducted on polycrystalline and crushed ice. Tests were also conducted on pre-damaged samples. All samples were made in the laboratory from fresh-water. The confining pressures were up to 20 MPa and strain-rates were up to 2×10^{-2}/s at $-10°$ C room temperature.

The viscoelastic response of material with cracks and pores is presented using two theories: first, a theory based on the modified superposition method, and second, a mechanical method. In the modified superposition method, the changes in the microstructures, "internal variables," are modelled first for a nonlinear elastic material then the problem is transformed into the viscoëlastic domain using correspondence principles. In the mechanical model each constituent is identified separately, and the material is presented by combination of nonlinear springs and dashpots. This method provided more flexibility and the change in the internal variable affected various constituents separately. Both of these theories are developed based on thermodynamics foundations and the material is assumed to be statistically isotropic through the deformation process, i.e., the optical-axis, the grain-boundaries and cracks are randomly oriented in space.

1.4 Organization of the Thesis

This thesis is divided into eight chapters. In Chapter 1, the problem is identified with a brief introduction to the mechanical properties of particulate materials. A detailed review of the material behaviour and relevant constitutive theories to describe them is presented in Chapter 2. This includes the mechanical behaviour of elastic and viscoelastic continua with changing microstructure. The description includes a brief discussion on phenomenological and microstructural continuum theories. Finally, these theories are again discussed in particular for composite materials, damaging materials and porous materials.

In Chapter 3, the details of triaxial test-setup and procedure for crushed ice and polycrystalline ice are presented. The results of these tests are presented in Chapter 4, and the material behaviour and microstructural features are discussed.

In Chapter 5, a continuum theory to describe a material with growing damage due to microcracking is presented. The effect of individual microcracks and their growth is studied by averaging at a scale that is much larger than size of microstructures. For nonlinear viscoelastic problems, a method due to Schapery (1991) and based on modified superposition method is reformulated and validated for polycrystalline ice.

A mechanical method based on the reduced time characterization due to Schapery (1969) and Jordaan et al. (1992) is also presented. The developed theories are compared with the triaxial tests results.

In Chapter 6, a theory to describe the mechanical behaviour of crushed ice under high pressure is presented. A closed-form solution for elastic materials containing voids and obeying a power-law is also presented. The elastic results are then extended to predict the viscoelastic response of crushed ice.

In Chapter 7, the flow properties of crushed ice under plane-strain extrusion conditions are examined. Finite element analyses are conducted to compare the test results and the theoretical developments. A closed-form solution is also presented for the plane strain extrusion of viscous material following power-law nonlinearity.

Finally, the results of earlier chapters are summarized in Chapter 8, and recommendations are made for future study.

Chapter 2

Theory of Materials with Microstructure

2.1 Introduction

In this chapter, a thermodynamic theory for elastic and viscoelastic continua with changing microstructure is described. The description includes a brief discussion on phenomenological and microstructural continuum theories for elastic and viscoelastic materials. Many viscoelastic problems can be solved by analogy to elastic solutions. The correspondence principles are presented for such an analogy. Finally, particular aspects of composite materials, and the effect of microcracking and pore collapse on the stiffness of polycrystalline materials are discussed.

2.2 Equivalent Homogeneity

A constitutive theory for particulate materials can be based on phenomenological or microstructural principles. From the phenomenological viewpoint, these materials exhibit dilatancy, and are sensitive to hydrostatic stress. Since these characteristics are due to their microstructure, the microstructural definition is of fundamental importance. The microstructural approach is based on the interaction between fundamental constitutive units of the material. The geometric measure of the local granular structure is incorporated into the continuum theory. A constitutive relation for deformation of an assemblage of grains or crystals is developed, and the total behaviour is expressed in terms of volume-averaged quantities.

The elastic properties of composite materials are dependent on the elastic properties and the volume fractions of the matrix and the particulate phases. The geometric features of the microstructure can be the crystal grain structure in polycrystalline materials, where each grain is anisotropic and different grains have different orientation, or, ellipsoidal-shaped inclusions embedded in a continuous matrix phase as in composites. The microcracks can be considered as ellipsoidal inclusions where one dimension is very small. In porous materials, the inclusion phase lacks stiffness.

The presence of microstructure creates inhomogeneity in the material. To use the theory of elasticity, which is developed for homogeneous materials, state variables such as stress and strain need to be redefined. The scale of inhomogeneity is assumed to be orders of magnitude smaller than the characteristic dimensions of the problem of interest, such that there exists an intermediate dimension over which averaging can be legitimately performed. Figure 2.1 shows such representative volume with microstructures.

The validity of the phenomenological models is limited to the cases where the minimum dimensions of the sample are several times larger than the maximum dimensions of grains. The resulting homogeneous state of strain should be achieved during testing of the material. In fact, all tests on granular materials indicate the heterogeneous nature of the strain (Oda et al., 1980, Fukue, 1979). This makes phe-

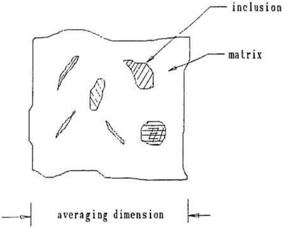

Figure 2.1: Volumetric averaging.

nomenological continuum theories dubious (Cowin, 1978), unless such heterogeneity is properly addressed.

2.3 Thermodynamic Constitutive Theory

The response of many materials depends to a large extent on their history. The inelastic deformation of metals, polymers, and frictional materials exhibit history-dependent behaviour, though with dissimilar patterns. In theories using internal variables, dependence on the history is represented by the variables describing the structure of the material elements. Some examples are changes in the crack and averaged micro-crack geometry, void ratio and dislocation arrangements.

In a thermodynamic system, the internal energy and forces are state functions of state variables such as temperature, and some measure of deformation, e.g., strain. The state variables serve to define the system, but are often insufficient to do so by themselves. In a reversible system the state is explicitly defined by external variables, but in an irreversible system some additional variables not available for macroscopic observations must be introduced to account for the loss of energy (Bridgman, 1950). These additional variables are referred as internal variables. The internal variable approach (Bridgman, 1950; Biot, 1954; Coleman and Gurtin, 1967; Schapery, 1969) is based on non-equilibrium thermodynamics. In this theory a free energy function is assumed to exist that is a function of all external and internal variables. Another approach in internal variable theory is due to Kestin and Rice (1970) and Rice (1971), who postulated that it is always possible to determine a finite set of internal variables so that their number is adequate to render the non-equilibrium state under consideration sufficiently close to a constrained state of the thermodynamic equilibrium. Both internal variable theories give the same result.

Rice (1971, 1975) formulated a thermodynamic theory based on microstructural features for crystalline slip, diffusion, and Griffith cracks. Hansen and Brown (1986, 1988) extended Rice's theory to granular snow, and identified the state variables at the granular level rather than the crystalline level in the Rice's work. Schapery (1990) presented the internal variable formulation for the deformation of non-linear elastic media with changes in micro-structures such as micro-crack growth, healing and transformations. This theory is reviewed in this section.

2.3.1 Strain Energy

A basic assumption for all the process of interest is that a strain energy function W exists. The strain energy is a function of all external variables, e.g., strain ϵ_{ij} and independent internal variables S_m,

$$W = W(\epsilon_{ij}, S_m). \tag{2.1}$$

The stress is defined as

$$\sigma_{ij} = \partial W / \partial \epsilon_{ij}. \tag{2.2}$$

The parameters S_m may define changes in microstructure, such as microcrack geometry, void volume and grain boundary sliding. When the S_m are constant the material is hyperelastic (Malvern, 1969), and the definition is not limited to linear elastic materials. For non-isothermal processes W is the Helmholtz free energy and is also a function of temperature. In the present developments only isothermal processes are considered. The free energy also contains surface energy (Rice, 1978) $W_{se} = 2\gamma_m A_m$, where γ_m is the surface energy per unit area of m^{th} crack with the surface area of A_m. The surface energy is reversible, and often negligible.

2.3.2 Work

The strain energy defined in Equation 2.1 is the work done when all S_m are constant. The work done in a real process in which S_m are not constant, is partially irreversible. The energy is irreversible due to the dissipative nature of friction, and the microcracking where the energy is dissipated in processes such as creep and plastic flow. The total work in a real process, and associated with σ_{ij} and ϵ_{ij} is

$$W_T = \int \sigma_{ij} d\epsilon_{ij}, \tag{2.3}$$

where the repeated indices follow the summation convention.

The strain energy and total work are interrelated. For an infinitesimal change in ϵ_{ij} the change in strain energy from Equation 2.1 is,

$$dW = \frac{\partial W}{\partial \epsilon_{ij}} d\epsilon_{ij} + \frac{\partial W}{\partial S_m} dS_m = \sigma_{ij} d\epsilon_{ij} - f_m dS_m, \tag{2.4}$$

where Equation 2.2 is used and f_m are thermodynamic forces defined as

$$f_m = -\partial W / \partial S_m. \tag{2.5}$$

The thermodynamic forces f_m produce changes in the microstructural parameters S_m. For a cracking material if S_m is surface area of a crack, the thermodynamic force is the energy release rate for crack propagation. If surface energy is also considered apart from other microstructural changes in the material during deformation, and crack growth is locally self-similar, then the increase in the surface energy due to crack growth is proportional to the amount of new free surface. Here the free energy is $W + W_{se}$ and the thermodynamic force responsible for cracking is

$$f_m = G_m - \partial W_{se}/\partial A_m, \tag{2.6}$$

where G_m is the energy release rate and A_m is the surface area.

The change of total work is obtained by integrating Equation 2.1 from any arbitrary state 1 with strain energy W^1 to the current state,

$$\Delta W_T = W - W^1 + \int_1 f_m dS_m, \tag{2.7}$$

where Equation 2.3 is used. Thus the total work done is separated into strain energy, which is reversible, and an irreversible energy $W_s = W_s(S_m)$, which can serve to define the evolution law

$$f_m = \partial W_s/\partial S_m. \tag{2.8}$$

For a process starting from the reference state at $t = 0$ where $W = W_s = 0$,

$$W_T = W + W_{se} + W_s \tag{2.9}$$

2.3.3 Thermodynamics

Materials should satisfy the second law of thermodynamics, besides the equilibrium equations and the constitutive assumptions. This law postulates the existence of entropy as a state function of all state variables including non-observable internal variables S_m (Malvern, 1969). The second part of this law states that the rate of entropy production per unit mass s of the universe is always positive. It is zero for reversible processes. Thus for all processes,

$$\dot{s} = \dot{s_I} + \dot{s_{II}} \geq 0, \tag{2.10}$$

where s_I is entropy of the system under consideration, and s_{II} is entropy of the surroundings. Now the system is brought in contact with a heat reservoir that is large enough to maintain the system at constant temperature T. If $\dot{Q}$ is rate of heat transferred from the system to the reservoir, using the definition of entropy from the first part of second law $\dot{s_{II}} = \dot{Q}/T$, Equation 2.10 becomes,

$$\dot{s} = \dot{s_I} + \frac{\dot{Q}}{T} \geq 0. \tag{2.11}$$

From the first law of thermodynamics, the rate of work done $\dot{W}_T = \sigma_{ij}\dot{\epsilon_{ij}}$ and the rate of change in internal energy $\dot{U}$ of the system are related to the rate of heat transfer $\dot{Q}$ as

$$\dot{U} = \sigma_{ij}\dot{\epsilon_{ij}} - \dot{Q} \tag{2.12}$$

Using the definition of strain energy $W = U - Ts_I$, the second law (Equation 2.11) becomes

$$T\dot{s} = \sigma_{ij}\dot{\epsilon_{ij}} - \dot{W} \geq 0. \tag{2.13}$$

Biot (1954) used this form of second law to derive the theory of viscoelasticity. This work is reviewed in Section 2.3.

Using Equation 2.4, Equation 2.13 can be presented as

$$T\dot{s} = f_m\dot{S_m} \geq 0. \tag{2.14}$$

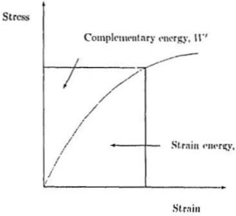

Figure 2.2: Stress-strain curve

2.3.4 Force-Based Formulation

In the formulation of the last section, strain was taken as an independent state variable. Material properties are often evaluated in such a way by constant strain-rate tests. In force-controlled processes, which are common in hard solids such as metals, the flexibility of test frames makes strain-controlled deformations difficult, an alternative approach where the stress is the independent state variable may be more suitable. For this case the constitutive equation can be formulated in terms of complementary strain energy W' (see Figure 2.2) defined as,

$$W' = \sigma_{ij}\epsilon_{ij} - W \tag{2.15}$$

The differential of W' is obtained by using Equation 2.4 as,

$$dW' = \epsilon_{ij}d\sigma_{ij} + f_m dS_m \tag{2.16}$$

Thus, the functional form for W' is,

$$W' = W'(\sigma_{ij}, S_m). \tag{2.17}$$

The strain ϵ_{ij} and the thermodynamic force f_m is defined by Equation 2.16 as,

$$\epsilon_{ij} = \partial W' / \partial \sigma_{ij}, \tag{2.18}$$

$$f_m = \partial W' / \partial S_m, \tag{2.19}$$

or, in the functional form as,

$$\epsilon_{ij} = \epsilon_{ij}(\sigma_{ij}, S_m), \tag{2.20}$$

$$f_m = f_m(\sigma_{ij}, S_m). \tag{2.21}$$

Using Equation 2.8 and 2.19,

$$\partial W' / \partial S_m = \partial W_s / \partial S_m \tag{2.22}$$

The total complementary work W_T' is defined as,

$$W_T' = \sigma_{ij}\epsilon_{ij} - W_T, \tag{2.23}$$

and can be separated into complementary strain energy W' and the irreversible energy W_s as,

$$W_T' = W' + W_s \tag{2.24}$$

The incremental form of Equation 2.20 is

$$d\epsilon_{ij} = \frac{\partial \epsilon_{ij}}{\partial \sigma_{ij}} d\sigma_{ij} + \frac{\partial \epsilon_{ij}}{\partial S_m} dS_m. \tag{2.25}$$

Using Equation 2.18 and 2.19,

$$d\epsilon_{ij} = D_{ijkl} d\sigma_{kl} + \frac{\partial f_m}{\partial \sigma_{ij}} dS_m \tag{2.26}$$

where D_{ijkl} is the compliance tensor given by

$$D_{ijkl} = \frac{\partial^2 W'}{\partial \sigma_{ij} \partial \sigma_{kl}} \tag{2.27}$$

At constant temperature and at current value of S_m, and when the load is removed, i.e., $\sigma_{ij}=0$, the remaining strain is inelastic strain associated with a state S_m. The strain increment can be divided into an elastic or recoverable part $d\epsilon_{ij}{}^{el}$, and an irrecoverable part $d\epsilon_{ij}{}^{p}$ as,

$$d\epsilon_{ij} = d\epsilon_{ij}{}^{el} + d\epsilon_{ij}{}^{p} \tag{2.28}$$

where

$$d\epsilon_{ij}{}^{el} = D_{ijkl} d\sigma_{kl}$$

$$d\epsilon_{ij}{}^{p} = \frac{\partial f_m}{\partial \sigma_{ij}} dS_m.$$

Rice (1971) related the irreversible strain increment to a plastic flow potential as in the theory of plasticity. This review is restricted to elastic and viscoelastic theories.

The selection of suitable internal variables representing the microstructure is very important, and should be based on experimental observations. The number of internal variables should be large enough (within the limit of practical applicability) to represent the material behaviour under desired conditions. Simultaneously, they should have physical significance so that they can be measured directly or indirectly. At least one internal variable is desired to present history dependence in the material, but more may be needed for non-linear response characterization.

2.4 Viscoelastic Theory

In this section viscoelastic theories for material with microstructure is discussed. First, linear viscoelastic theory based on irreversible thermodynamics is presented in brief. This is followed by a review of nonlinear viscoelastic theories. Finally correspondence principles are described to obtain viscoelastic solutions from solutions for elastic materials.

2.4.1 Linear Theory

For linear viscoelastic materials stress $\sigma_{ij}(t)$ can be expressed in most general form using the Boltzmann superposition principle as

$$\epsilon_{ij}(t) = \int_0^t D_{ijkl}(t-\tau)\frac{d\sigma_{kl}(\tau)}{d\tau}d\tau, \tag{2.29}$$

where $D_{ijkl}(t)$ is creep compliance and τ is any arbitrary time between 0 and t. The creep compliance is defined as the creep strain resulting from the application of unit stress. This is also a memory function that describes the stress-history dependency of the strain.

Biot (1954) derived the evolution Equation 2.29 using the thermodynamics described in Section 2.3.3. The theory was presented in generalized coordinates. The generalized forces, $Q_j,\ j = 1, 2, ..n$ include external forces $Q_j,\ j = 1, 2, ..k$, and thermodynamic forces $Q_j,\ j = k+1, k+2, ..n$. The corresponding generalized displacements, $q_j,\ j = 1, 2, ..n$ include external displacements $q_j,\ j = 1, 2, ..k$, and hidden displacements (internal variables) $q_j,\ j = k+1, k+2, ..n$. Equation 2.13 can be written as

$$T\dot{s} = X_j\dot{q}_j \geq 0 \tag{2.30}$$

where the coefficients X_j are functions of all quantities affecting irreversibility of the process and are defined as

$$X_j = Q_j - \frac{\partial W}{\partial q_j}. \tag{2.31}$$

If the phenomenological laws connecting X_j and the velocity $\dot{q}_j$ are linear so that

$$X_j = b_{ji}\dot{q}_i, \tag{2.32}$$

the evolution Equation 2.30 can be written as

$$T\dot{s} = b_{ij}\dot{q}_j\dot{q}_i \geq 0. \tag{2.33}$$

The coefficients b_{ij} are viscosity terms, and are symmetric ($b_{ij} = b_{ji}$) due to the Onsager's principle (Fung, 1965). Substituting Equation 2.32 in Equation 2.31, the governing equation of equilibrium is

$$\frac{\partial W}{\partial q_j} + b_{ij}\dot{q}_i = Q_j. \tag{2.34}$$

The strain energy is expanded in quadratic form

$$W = \frac{1}{2}a_{ij}q_jq_i, \tag{2.35}$$

where the coefficients a_{ij} are symmetric and are defined as

$$a_{ij} = \frac{\partial^2 W}{\partial q_i \partial q_j}. \tag{2.36}$$

Thus, Equation 2.34 can be put in the form

$$a_{ij}q_i + b_{ij}\dot{q}_i = Q_j. \tag{2.37}$$

The solution of this equation was obtained by eliminating hidden displacements; this was accomplished by using the fact that all thermodynamic forces vanish for all indices corresponding to hidden displacements. The influences of the internal variables are to reveal the hereditary character of the material. The solution of Equation 2.37 is analogous to a mechanical model made of several Maxwell type materials plus a spring and a dashpot all in parallel (see Figure 2.3a). This mechanical model is theoretically equivalent to the generalized Voigt model as shown in Figure 2.3b.

The solution of the mechanical model described in Figure 2.3 for uniaxial creep test is

$$D(t) = \frac{1}{E_m} + \sum_{i=1}^{n} \frac{1}{E_i}[1 - e^{-t/t_i^c}] + \frac{t}{\eta_m}, \tag{2.38}$$

where $t_i^c = \eta_i/E_i$ is i^{th} retardation time. The three different terms in Equation 2.38 are the elastic, the delayed elastic and the steady state flow compliances. Equation 2.38 is

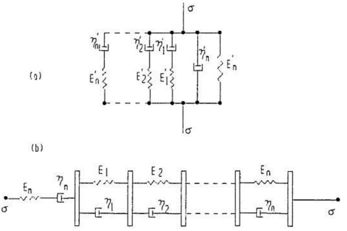

Figure 2.3: (a) Mechanical model suggested by Biot (1954). (b) Generalized Voigt model.

most general form of time-dependence that is physically possible. In practice a chain of Maxwell or Kelvin units is needed, which is represented by the summation term in Equation 2.38. This leads to a large number of parameters that must be evaluated. For many viscoelastic materials, the summation term can be approximated into a power-law term. In such cases the compliance is

$$D(t) = D_0 + D_1 t^b + D_2 t, \tag{2.39}$$

where D_0, D_1, D_2 and b that is $0 < b < 1$ are material constants. It should be noted the unlike Equation 2.38, which is unbounded in time scale, Equation 2.39 is valid for a limited (often large) time.

The inverse of Equation 2.29 in terms of relaxation moduli C_{ijkl} are

$$\sigma_{ij}(t) = \int_0^t C_{ijkl}(t-\tau)\frac{d\epsilon_{kl}(\tau)}{d\tau}d\tau, \tag{2.40}$$

The relaxation moduli and creep compliances as in Equation 2.29 and 2.40 are components of fourth-order tensors. These tensors are symmetric due to the Onsager's principle. Since creep and relaxation phenomena are two aspects of the same viscoelastic behaviour of materials, they should be related. Such relation is obtained by applying the Laplace transform to Equations 2.29 and 2.40. The result in terms of the transformed variable s is:

$$\hat{\epsilon}_{ij}(s) = s\hat{D}_{ijkl}(s)\hat{\sigma}_{kl}(s), \tag{2.41}$$

$$\hat{\sigma}_{ij}(s) = s\hat{C}_{ijkl}(s)\hat{\epsilon}_{kl}(s), \tag{2.42}$$

where $\hat{\epsilon_{ij}}$ represents Laplace transform of the quantity ϵ_{ij}. From Equations 2.41 and 2.42

$$\frac{\hat{\sigma}_{ij}(s)}{\hat{\epsilon}_{kl}(s)} = s\hat{C}_{ijkl}(s) = \frac{1}{s\hat{D}_{ijkl}(s)}, \tag{2.43}$$

or

$$\hat{D}_{ijkl}(s)\hat{C}_{ijkl}(s) = \frac{1}{s^2}. \tag{2.44}$$

Applying the inverse Laplace transform to Equation 2.44 yields

$$\int_0^t D_{ijkl}(t-\tau)C_{ijkl}(\tau)d\tau = t \tag{2.45}$$

Equation 2.45 defines the relationship between the creep compliances D_{ijkl} and the relaxation moduli C_{ijkl} for linear elastic materials.

The form of Equations 2.41 and 2.42 is analogous to Hooke's law. A solution using this analogy is presented in Section 2.4.5.

2.4.2 Multiple-Integral Representations

For large strains most viscoelastic materials exhibit nonlinear behaviour. A generalization of linear viscoelastic theory for such cases is possible by using multiple integrals (Green and Rivlin, 1957). The stress relaxation was formulated in terms of

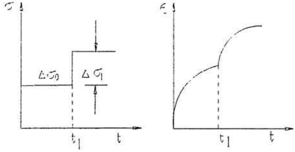

Figure 2.4: Creep response to multiple step of stress

a tensor functional of strain history based on invariants. The current stress at a point is not only a function of current deformation, but also the deformation gradients at all previous times. A simple explanation as given by Findley et al. (1976) is presented here.

A nonlinear viscoelastic material is subjected to a constant stress $\Delta\sigma_0$ at time $t = 0$ and $\Delta\sigma_1$ is additionally applied at time $t = t_1$ as shown in Figure 2.4. The time-dependent strain resulting from this stress is presented in polynomial form

$$\begin{aligned}\epsilon(t) &= (\Delta\sigma_0)D_1(t) + (\Delta\sigma_0)^2 D_2(t,t) + \\ &\quad +(\Delta\sigma_1)D_1(t-t_1) + (\Delta\sigma_1)^2 D_2(t-t_1, t-t_1) + \\ &\quad +2(\Delta\sigma_0)(\Delta\sigma_1)D_2(t, t-t_1), \end{aligned} \tag{2.46}$$

where the D_n are time-dependent material functions. Only second order terms are considered in this equation. The time function $D_n(t)$, $D_n(t,t)$ are the same in this equation. The first two terms in the right hand side in Equation 2.46 are due to stress $\Delta\sigma_0$, the next two due to stress $\Delta\sigma_1$ and the last term comes from the interaction of the two stresses. If N load steps are applied in this manner, the response is

$$\epsilon(t) = \sum_{i=0}^{N}(\Delta\sigma_i)D_1(t-t_i) + \sum_{i=0}^{N}\sum_{j=0}^{N}(\Delta\sigma_i)(\Delta\sigma_j)D_2(t-t_i, t-t_j) + ... \tag{2.47}$$

For arbitrary varying stress history, Equation 2.47 can be presented in the form

$$\epsilon(t) = \int_0^t D_1(t-\tau_1)\dot{\sigma}(\tau_1)d\tau_1 + \int_0^t\int_0^t D_2(t-\tau_1, t-\tau_2)\dot{\sigma}(\tau_1)\dot{\sigma}(\tau_2)d\tau_1 d\tau_2 + ... \quad (2.48)$$

For generality, this theory requires several functions with higher order stress terms to describe creep behaviour satisfactorily. This representation is suitable for all class of materials and can be approximated to the desired degree of nonlinearity. The experimental determination of kernel functions D_n is most difficult in this method, and requires a large set of creep data. For strong nonlinear cases it becomes impractical to use this approach.

2.4.3 Characterization Using Reduced Time

Schapery (1969) derived a simple method to account for nonlinearity using the thermodynamics of irreversible processes (see Section 2.3). The linear law of Equation 2.32 was replaced by a nonlinear law:

$$X_j = b'_{ji}\dot{q}_i, \quad (2.49)$$

where

$$b'_{ij} = a_d b_{ij}. \quad (2.50)$$

The function a_d is non-negative. The coefficients b_{ij} are still a constant matrix corresponding to the linear response in the neighborhood of the reference equilibrium state. Thus the governing Equation 2.34 becomes

$$\frac{\partial W}{\partial q_j} + a_d b_{ij}\frac{dq_i}{d\psi} = Q_j. \quad (2.51)$$

The "reduced time" $\psi(t)$ is an implicit function of state variables such as stress in the creep formulation, and is defined as

$$\psi(t) = \int_0^t \frac{d\tau}{a_d[\sigma(t)]}. \quad (2.52)$$

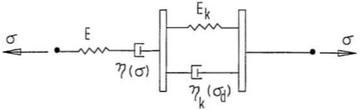

Figure 2.5: A mechanical model for reduced time characterization.

The resulting theory is similar to Equation 2.29. The shift factor can be a function of other nonlinear effects, e.g., temperature and aging. The integral form for uniaxial stress-state is

$$\epsilon(t) = \int_0^t D[\psi(t) - \psi(\tau)] \frac{d\sigma(\tau)}{d\tau} d\tau. \tag{2.53}$$

Jordaan and McKenna (1988) have successfully employed this theory in the creep prediction of ice. The function a_d was considered as a stress-dependent viscosity. For a power law creep material, $\dot{\epsilon} = (\sigma/\sigma_0)^n \dot{\epsilon}_0$, the shift factor is given as,

$$a_d = \eta(\sigma) = \frac{\sigma_0^n}{\sigma^{n-1} \dot{\epsilon}_0} \tag{2.54}$$

where σ_0 and $\dot{\epsilon}_0$ are reference stress and strain-rate respectively. This model can be presented mechanically as in Figure 2.5. This theory is general for nonlinear viscoelastic materials without changes in the micro-structure during the deformation.

2.4.4 Modified Superposition Principle

Another generalization of the linear theory for nonlinear materials is the "modified superposition principle" (MSP) (Findley et al., 1976). For uniaxial stress-state,

$$\epsilon = \int_0^t L(\sigma, t - \tau) \frac{dF(\sigma, \tau)}{d\tau} d\tau, \tag{2.55}$$

where F and L are empirical functions of time and stress. MSP is an approximate method, which uses the kernel function determined from one step creep test to describe nonlinear creep behaviour under arbitrary stress-history. The accuracy of description depends on the material and type of stress history. This theory is not general enough to describe all materials with memory, but it is simple to use for some nonlinear materials under quasi-static loading.

Schapery (1981, 1991) has used a form of Equation 2.55, where the function L is independent of stress and is a linear creep compliance $L = D(t)$ in Equation 2.29, and reflects creep behaviour over some useful stress range. All non-linearity of the material was addressed by the stress function $F(\sigma, t)$,

$$\epsilon = \int_0^t D(t-\tau)\frac{dF(\sigma,\tau)}{d\tau}d\tau, \tag{2.56}$$

where $F(0) = 0$. Mechanically, Schapery's model can be presented as in Figure 2.3, with $F(\sigma)$ replacing σ, all other components remain same and describe the linear compliance D of Equation 2.56. The springs and dashpots are linear, unlike the model presented in Figure 2.3. For example, for a power-law viscous material ($\dot{\epsilon} = D_2\sigma^n$), $F(\sigma) = \sigma^n$ and $D(t) = D_2 t$, which is linear.

The modified superposition principle provides a simple method for predicting viscoelastic response from elastic solutions, when generalized to three-dimensional loading. Following Schapery (1981), the modified superposition method as presented in Equation 2.56 can be extended to include changes in the microstructure. The nonlinear function $F(\sigma)$ is also a function of randomly distributed and time-dependent microstructural parameters ($S_m, m = 1, 2, ..$). The uniaxial constitutive relation is

$$\epsilon(t) = E_R\int_0^t D(t-\tau)\frac{d\epsilon^e(\sigma,S)}{d\tau}d\tau, \tag{2.57}$$

where the quantity ϵ^e is referred to as pseudo-strain and is explicit function of stress, spatial coordinates and time. The coefficient E_R is a free constant and is termed the reference modulus and introduced to give ϵ^e the unit of strain. For an elastic material with constant $S, E_R = 1/D$ and $\epsilon = \epsilon^e$. Thus ϵ^e is the strain that exists in an elastic material with the same set of microstructural parameter S_m as the viscoelastic material.

Prediction of material behaviour using this method requires determination of the quantity ϵ^e that is a function of the stress-field and microstructural parameters S_m. For many cases one structural parameter is often sufficient, but when there are complex changes in the microstructure, more than one microstructural parameter may be required for different physically identified characteristics. For a material like crushed ice, one measure of microstructure may be for densification due to pressure, while the other may include grain boundary sliding under shear. These features are discussed in detail in Chapters 5 and 6. The form of the function ϵ^e can be obtained by inverting Equation 2.57:

$$\epsilon^e(t) = \frac{1}{E_R}\int_0^t C(t-\tau)\frac{d\epsilon(t)}{d\tau}d\tau, \tag{2.58}$$

where $C(t)$ is the relaxation modulus.

If $\epsilon^e = \sigma/E_R$, linear viscoelastic theory is recovered. As the function $D(t)$ is independent of state variables and the value E_R is a constant, the theory expressed in Equation 2.57 imposes a qualification that Poisson's ratio is constant during the process. The representation of nonlinearity and damage in a single function ϵ^e imposes some restrictions on the material type represented. If a power-law is used for material representation, all components of creep compliance, i.e., elastic, anelastic and steady-state creep, should follow same power-law. In ice, elastic behaviour is linear, while delayed-elastic and creep terms follow separate type of power-laws in time and stress; the applicability of single power law based model cannot cover all these features. However, in some cases where creep component may be dominant and elastic component may be negligible, this theory is expected to provide good results.

For multiaxial behaviour the constitutive law is,

$$\epsilon_{ij} = E_R \int_0^t D(t-\tau)\frac{d}{d\tau}(\frac{\partial W^c}{\partial \sigma_{ij}})d\tau, \tag{2.59}$$

where W^c is complementary pseudo-energy, which defines pseudo-strain ϵ^c_{ij} as,

$$\epsilon^c_{ij} = \frac{\partial W^c}{\partial \sigma_{ij}} \tag{2.60}$$

2.4.5 Correspondence Principles

For many viscoelastic problems, the time variable can be removed by taking the Laplace transform of the governing field and boundary equations with respect to time, thus reducing them to mathematically equivalent elastic problems. This analogy is called the correspondence principle, and implies that elastic analysis methods can be used to derive the referred viscoelastic problem (Lee, 1955; Christensen, 1971; Findley et al., 1976).

The relationship between shear stress τ and shear strain γ in linear elasticity, and shear strain-rate $\dot{\gamma}$ in Stokes' flow laws are given by

$$\tau = G\gamma \tag{2.61}$$

$$\tau = \eta\dot{\gamma} \tag{2.62}$$

where G and η are the shear modulus and the coefficient of viscosity, respectively. An analogy between these equations exits, and viscous solutions can be obtained by replacing shear strain in an elastic solution with the shear strain-rate. In a similar way an analogy between steady-state creep and nonlinear elasticity can be established. Let the nonlinearity be expressed by power law, elastic equation is

$$\gamma = \epsilon_0(\tau/\sigma_0)^n, \tag{2.63}$$

and the steady-state creep be defined by

$$\dot{\gamma}^c = \dot{\epsilon}_0(\tau/\sigma_0)^n, \tag{2.64}$$

where $\sigma_0, \epsilon_0, \dot{\epsilon}_0$ and n are material constants. Comparing Equations 2.63 and 2.64, if a nonlinear elastic solution for ϵ_0, n and γ is available, these can be switched to $\dot{\epsilon}_0, n$ and $\dot{\gamma}^c$ to obtain the solution for creep. Equation 2.61 and 2.62 are special cases of Equations 2.63 and 2.64 when the power n is 1.

Linear Viscoelastic Stress Analysis

Let $\sigma_{ij}(t)$ and $\epsilon_{ij}(t)$ be the stress and the strain tensor, and $u_i(t)$ be the displacement vector in the material at the position x and time t, the equations of equilibrium are

$$\sigma_{ij}(t)_{,j} + F_i(t) = 0. \tag{2.65}$$

where F_i are the body forces. The notation $\sigma_{ij,j}$ denotes the partial derivative of σ_{ij} with respect to the position vector x_j. The strain-displacement relations are

$$\epsilon_{ij}(t) = \frac{1}{2}\left[u_i(t)_{,j} + u_j(t)_{,i}\right]. \tag{2.66}$$

These strains satisfy the compatibility relations

$$\epsilon_{ij,kl}(t) + \epsilon_{kl,ij}(t) - \epsilon_{ik,jl}(t) - \epsilon_{jl,ik}(t) = 0 \tag{2.67}$$

Let the boundary S is divided into a region S_T and a complementary region $S_u = S - S_T$. On S_T, external loading T_i are prescribed as

$$\sigma_{ij}(t)n_j = T_i(t). \tag{2.68}$$

On S_u, the surface displacement U_i is prescribed as

$$u_i(t) = U_i(t). \tag{2.69}$$

These field equations together with the constitutive Equations 2.29, or, 2.40 form a complete set for linear viscoelastic stress analysis.

Solution Using Correspondence Principle

The Laplace transforms of Equations 2.65 to 2.69 yield

$$\hat{\sigma}_{ij}(s)_{,j} + \hat{F}_i(s) = 0, \tag{2.70}$$

$$\hat{\epsilon}_{ij}(s) = \frac{1}{2}\left[\hat{u}_i(s)_{,j} + \hat{u}_j(s)_{,i}\right]. \tag{2.71}$$

$$\hat{\epsilon}_{ij}(s)_{,kl} + \hat{\epsilon}_{kl}(s)_{,ij} - \hat{\epsilon}_{ik}(s)_{,jl} - \hat{\epsilon}_{jl}(s)_{,ik} = 0 \tag{2.72}$$

$$\hat{\sigma}_{ij}(s) n_j = \hat{T}_i(s) \tag{2.73}$$

$$\hat{u}_i(s) = \hat{U}_i(s). \tag{2.74}$$

The Laplace transform of the constitutive Equation 2.40 is presented in Equation 2.42.

These transformed equations are similar to elasticity equations, where elastic constants $s\hat{C}_{ijkl}(s)$, body forces $\hat{F}_i(s)$, external forces $\hat{T}_i(s)$ on S_T and external displacements $\hat{u}_i(s)$ on S_u are functions of the transformed parameters. After the associated elastic problem is solved for $\hat{\sigma}_{ij}(s)$ and $\hat{u}_i(s)$, the inverse Laplace transform gives the time-dependent solutions for $\sigma_{ij}(x,t)$ and $u_i(x,t)$. A closed-form inverse transform is not always possible, and one has to resort to approximate and numerical solutions.

This analogy often provides an easy tool for linear viscoelastic materials. In this approach of solution, some limitations on the boundary conditions apply. The boundaries at which stresses and displacements are prescribed should be independent of time. However these condition themselves can be time-dependent (Findley et al. 1976). Furthermore the correspondence principles are limited to quasi-static considerations, where the inertia terms in the equation of motion are neglected.

Nonlinear Viscoelastic Materials

The analogy between elastic theory and viscoelastic theory provides an easy tool for linear viscoelastic materials, while for non-linear materials some restrictions apply.

For nonlinear problems, time and space dependence of prescribed functions should appear as separate factors as in Section 2.4.4. Schapery (1981) has presented correspondence principles for the analysis of viscoelastic cracked bodies. An analogy between nonlinear elastic and viscoelastic media with stationary and growing crack was derived. In the equivalent elastic state, the strain is replaced by pseudo-strain using Equation 2.57. The principle is shown in Figure 2.6.

From Schapery (1981), a reference elastic solution $\sigma_{ij}^R, \epsilon_{ij}^R$ and u_i^R are stress, strain and displacement tensors corresponding to the case in which $1/D(t-\tau) = E(t-\tau) = E_R$ (see, Section 2.4.4). These solutions follow the field Equations 2.70 to 2.72 and boundary conditions as given in Equations 2.73 and 2.74.

When the prescribed surface traction $T_i = \sigma_{ij}n_j$ on surface S and body forces F_i on volume V be specified functions of time and position, the nonlinear viscoelastic solutions based on Equation 2.57 are

$$\sigma_{ij} = \sigma_{ij}{}^R, \tag{2.75}$$

$$\epsilon_{ij} = E_R \int_0^t D(t-\tau)\frac{d\epsilon_{ij}{}^R}{d\tau}d\tau \tag{2.76}$$

$$u_i = E_R \int_0^t D(t-\tau)\frac{du_i^R}{d\tau}d\tau. \tag{2.77}$$

When displacements $U_i^R = u_i^R$ and traction $T_i = \sigma_{ij}{}^R n_j$ are prescribed on the boundary S_u and S_T respectively, and body forces F_i on volume V, the nonlinear solutions are

$$\sigma_{ij} = \sigma_{ij}{}^R, \tag{2.78}$$

$$\epsilon_{ij} = E_R \int_0^t D(t-\tau)\frac{d\epsilon_{ij}{}^R}{d\tau}d\tau \tag{2.79}$$

$$u_i = E_R \int_0^t D(t-\tau)\frac{du_i^R}{d\tau}d\tau. \tag{2.80}$$

Harper (1986) and Jordaan et al. (1992) have validated this theory of deformation of ice.

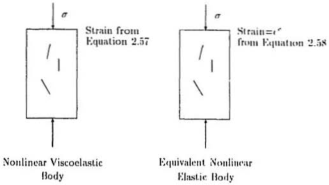

Imposed Traction, $T(t)$

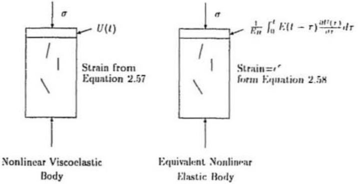

Imposed Displacement, $U(t)$

Figure 2.6: Correspondence principles (Schapery, 1981). Stresses in the viscoelastic and elastic bodies are equal.

2.5 Particular Aspects

The generalized theory discussed earlier in this chapter is applicable to a variety of problem involving changes in microstructures. The internal state variable in the theory may serve to define microcracking by the geometry of cracks and their orientation, pore-fraction and its variation, crystalline slip, grain size and its distribution, diffusion and phase changes. In this section, particular aspects of some of these microstructural features are discussed.

2.5.1 Composite Materials

Composite material consists of two or more different materials, which are usually firmly bonded together. There are many materials in this class, such as: concrete, alloys, porous and cracked media, polycrystalline materials, reinforced rubber, fibrous composites. The behaviour could be anisotropic because of alignment of some phases in certain direction. However in the present work only isotropic composites–more specifically statistically isotropic–are considered. Some examples in this class are: matrix containing spherical or randomly oriented and elongated particles, polycrystalline composites, porous materials, and matrix with randomly oriented cracks.

Following Christensen (1979), average stress and strain are

$$\bar{\sigma}_{ij} = \frac{1}{V}\int_V \sigma_{ij}(x_i)dV, \tag{2.81}$$

$$\bar{\epsilon}_{ij} = \frac{1}{V}\int_V \epsilon_{ij}(x_i)dV, \tag{2.82}$$

where x_i is the location in the body V. The effective behaviour of the heterogeneous media can be defined using linear moduli C_{ijkl}.

$$\bar{\sigma}_{ij} = C_{ijkl}\bar{\epsilon_{kl}} \tag{2.83}$$

To perform the averaging as in Equations 2.81 and 2.82, exact solutions for the field variables are required. This averaging is general and does not imply restriction on the geometry of the inclusion.

Let the superscript I represent the inclusion and M represent the matrix phase. The isotropic relationship for the inclusion and the matrix is

$$\sigma_{ij} = C^{I}_{ijkl}\epsilon_{kl} \text{ in } I \tag{2.84}$$

$$\sigma_{ij} = C^{M}_{ijkl}\epsilon_{kl} \text{ in } I \tag{2.85}$$

where C^I_{ijkl} and C^M_{ijkl} are elastic constants for inclusion and matrix. If there are N inclusions of volume $V_1, V_2, ...V_n$ in the representative volume V, the average stress is

$$\bar{\sigma}_{ij} = \underbrace{\frac{1}{V}\int_{V-\sum_{n=1}^{N} V_n} \sigma_{ij} dV}_{\text{in matrix}} + \underbrace{\frac{1}{V}\sum_{n=1}^{N}\int_{V_n} \sigma_{ij} dV}_{\text{in inclusion}}. \tag{2.86}$$

Using Equations 2.83 to 2.85, Equation 2.86 can be manipulated to provide

$$C_{ijkl}\bar{\epsilon}_{kl} = C^{M}_{ijkl}\bar{\epsilon}_{kl} + \frac{1}{V}\sum_{n=1}^{N}\int_{V_n}(\sigma_{ij} - C^{M}_{ijkl}\epsilon_{kl})dV. \tag{2.87}$$

The first term of Equation 2.87 shows conditions in matrix due to externally applied averaged stresses $\bar{\sigma}_{ij}$, while the second term shows the conditions within the inclusions with some unknown state σ_{ij} and ϵ_{ij}. If the conditions within inclusions can be obtained, the moduli of the composite C_{ijkl} can be estimated.

A review of various micromechanical models is presented in Christensen (1979, 1990), Mura (1982) and Hashin (1983). These are the equivalent inclusion method (Eshelby, 1957), composite-sphere method (Hashin, 1962), the self-consistent methods (Budiansky, 1965; Hill, 1965), the generalized self-consistent method (Christensen and Lo, 1979) and equivalent inclusion methods (Eshelby, 1957; Mura, 1982). For dilute composites, these methods give similar results; while for high concentration composites, the generalized self-consistent method gives best performance. For dilutely porous materials, such as compacted crushed ice, any of these methods is expected to provide good results.

Equivalent Inclusion Method

The equivalent inclusion method is based on Eshelby's (1957) solution for a uniformly stressed infinite continuum containing an ellipsoidal inclusion. The stress disturbance in the applied stress due to the inclusion is obtained by solving an equivalent homogeneous problem. For the problem of a composite material in which the particulate phases are surrounded by a homogeneous matrix, each particulate phase is considered to be an isolated ellipsoidal inclusion. The interaction of inclusions is neglected in this approach. This method is presented in detail in Appendix B.

Self-Consistent Methods

The self-consistent methods (Budiansky, 1965; Hill, 1965) provide an approximate but reliable estimate of bulk and shear moduli in polycrystalline materials. In the problem of a composite material in which the particulate phases are surrounded by an effective and homogeneous matrix, each particulate phase is considered to be an isolated ellipsoidal inclusion. The inclusion is assigned the properties and orientation of the particulate phase and the matrix properties coincides with that of the composite material (Figure 2.7a). Such mapping of the composite material is possible as the mean stress and displacements at its boundary are equal to those at the boundary of the equivalent idealized continuum. The consistency condition refers to unchanged density and displacement at the outer boundary. This results in a condition from which the isotropic effective properties can be obtained by solving coupled equations. This method is good when the inclusion concentration is dilute. At higher concentra-

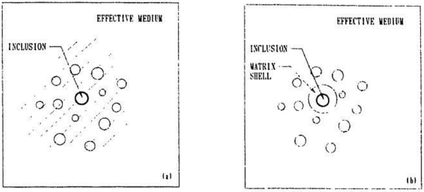

Figure 2.7: (a) Self-consistent and (b) the generalized self-consistent methods.

tions results are only useful when the moduli of the matrix and the inclusion phases are nearly identical (Christensen, 1982).

Christensen and Lo (1979) formulated a problem for composites in which the inclusion is embedded in a matrix shell that is embedded in the effective medium (Figure 2.7b). This three-phase problem is also called the generalized self-consistent method, and overcomes the drawback of classical self-consistent method.

2.5.2 Microcracking and Loss of Stiffness

In the last section, cracks with other microstructures were considered as inclusion in the material, to determine its elastic response. Here some theories for cracking solid are reviewed in general. Due to presence of these cracks the stiffness of the material is reduced significantly. Brittle materials such as concrete, rock, ceramics, and ice when loaded develop microcrack system and new microcracks could be nucleated. When the damage growth is stable, the density of cracks increases, and the elastic stiffness of the material degrades. Krajcinovic (1989) has presented a review of damage mechanics.

A simple elastic damaging material was presented by Dougill (1976). For uniaxial loading, Young's modulus E in Hooke's law, $\sigma = E_0\epsilon$ was presented as

$$E = E_0(1 - \lambda_d), \tag{2.88}$$

where λ_d is a damage parameter. The two extreme value of λ_d were defined as: $\lambda_d = 0$, material lacks damage, while $\lambda_d = 1$ represents total failure of stiffness in the material. As λ_d varies with the progress of damage, Hooke's law is presented in the rate form, and an evolution equation for the growth of damage is needed. This simple model does not account for any permanent deformation, thus, when unloaded strain vanishes.

Budianski and O'Connell (1976) have presented a self-consistent formulation to include microcracks. Planar and penny-shaped cracks were analysed as ellipsoidal inclusions in a homogeneous isotropic medium. This work has set the tone for great advancements in this area. Horii and Nemat-Nasser (1983) rederived this problem using fracture mechanics equations (Rice, 1968) of velocity field at the crack tip. They also included friction at the crack interface. Ashby and Hallam (1986) have presented a damage theory based on fracture mechanics and a beam theory by considering cracks in compression as wing cracks. Laws and Brockenbrough (1987) have presented solutions for the loss of stiffness in cracking solids for various cracks geometries. Often, the application of these models is restricted to the dilute concentration for microcracks. For large populations of microcracks, formulations based on the generalized self-consistent methods are appropriate. Schapery (1990a) has presented the response of cracking composites using this procedure. The popularity of these models is attributed to their clarity and efficiency in considering microcracks, and relating the response of the material to microstructures.

Chen and Orgon (1979) extended solution for linear elastic materials to obtain the responses of heterogeneous alloys following power-law creep, using an incremental method. At each increment of stress, linear theory was employed to determine stress-strain relationships. Nonlinear viscoelastic materials also can be presented by identifying various mechanisms in the material during deformation. Then a mechanical model can be presented. Jordaan and MaKenna (1991) and Jordaan et al. (1992) extended Schapery's reduced time formulation for nonlinear viscoelastic materials to include damage in ice using Budianski and O'Connell's (1976) isotropic crack density as a measure of damage. The elastic components in Figure 2.5 followed the damage theory, and the effective viscosities of the viscous components were enhanced based on experimental observation of Stone et al. (1989).

Based on the observation that the first grain-facet size cracks form in a polycrystalline material when the average grain-boundary sliding displacement reaches a critical value, Sinha (1989) formulated a kinetic equation for damage with the cracks density as its measure. The viscous component was then enhanced linearly with the number of cracks according to Weertman's (1969) formulation. Strong dependence of damage and the grain-size was observed.

A rational formulation of kinetic equations for microcracking can be presented using J-integral (Schapery, 1984, 1986). This formulation generalized the J-integral of discrete fracturing solids (Rice, 1968), and a distributed damage model was presented in the framework of the thermodynamic theory presented earlier in this chapter. The details of this theory are presented in Chapter 5.

2.5.3 Porous Materials

Porous materials are highly inelastic. With both hydrostatic and shear loading they undergo volumetric deformations, inelastically. These properties were reviewed in Chapter 1 in detail. Here various constitutive models that account for pores microstructuraly are reviewed. Some examples of porous materials are granular materials such as sand, and crystalline materials where pores are created during the process of sintering and failure. Feda (1982), Mróz (1980) and Johnson and Green (1976) have presented reviews of various models for porous materials.

The theory of plasticity has been used extensively in most phenomenological models of porous materials. Generally, the material is assumed to be elastic until a yield point is reached, as described by a yield surface in stress space. Then, further deformation is prescribed by a flow rule, and is a combination of elastic and plastic strains. As porous materials are sensitive to hydrostatic pressure and exhibit work-hardening or softening, and dilatation upon shear, the yield surface and the hardening rule depend on porosity, pressure and shear (Mróz, 1980). A model, which accounts for these features, the "cam-clay" model (Schofield and Wroth, 1968) and its variant the "cap model" (DiMaggio and Sandler, 1971), is widely used in soil mechanics.

The theory of plasticity provides solutions for many metals and geomaterials, but the phenomenological nature of this theory created need for more direct models with better understanding of micromechanics. By the virtual work principle, for a rigid and cohesionless granular assemblage, Christoffersen at al. (1981) established a general representation for the macroscopic stress in terms of the volume average of the product of contact forces and the vectors connecting the centroid of contacting grains. Mehrabadi and Nemat-Nasser (1983) concentrated on the fabric and its relation to applied stresses. They included statistical distribution of the contact forces and branches in Christoffersen's material description. Nemat-Nasser and Mehrabadi (1984) used kinematics of crystalline materials to model the deformation of granular materials.

A set of micromechanical models for porous materials can be obtained by considering pores as inclusions in the material, and the theories discussed in Appendix B can directly be used by setting the stiffness of the inclusion zero. Cracks can be considered as one population of pores, and were reviewed in the last section. Other population of pores consists of nearly spherical pores. Mackenzie (1950) has presented a self-consistent estimate of elastic modulus for spherical pores. Carroll and Holt (1972) have extended this model for elastic-plastic materials.

The response of viscous materials can be obtained from the elastic response in some cases using correspondence principles. Budianski et. al. (1982), Duva and Hutchinson (1984) and Cocks (1989) have presented solutions for nonlinear viscous materials. The extension of this work for nonlinear viscoelastic materials is presented in Chapter 6.

2.6 Summary

In this chapter, a review of elastic and viscoelastic materials with changing microstructure was presented with special attention given to cracking materials and porous materials. A thermodynamic theory based on internal variable approach was presented in detail. This theory provided a systematic framework for the analysis of materials with changing microstructure. Linear viscoelastic theory based on irreversible thermodynamics was presented. For nonlinear viscoelastic materials a single integral formulation is based on modified superposition method was presented, and correspondence principles were presented. Finally, particular aspects of microcracking and pore collapse on the stiffness of polycrystalline materials were discussed.

Chapter 3

Triaxial Tests

3.1 Introduction

Triaxial tests were conducted to investigate the mechanical properties of fresh-water ice in various damage states. During ice-structure interaction, zones of high pressure as mentioned in Section 1.3 are formed. The ice in these zones is subjected to high confining pressure as well as intense shear. This resulted in modifications in the microstructure. The triaxial tests were designed to investigate this process. The changes in the microstructure were determined from thin sections before and after tests. The behaviour of ice can be investigated in controlled laboratory conditions by loading an initially intact polycrystalline ice specimen, and then subjecting it to an appropriate stress-strain history. This method suitable is for peak stress evaluation. At advanced damage states failure occurs due to the instability created by sudden propagation of critical cracks. This problem was resolved by testing samples prepared from crushed ice by moulding.

The basic principle of the triaxial test is that a cylindrical sample is compressed axially while the hydrostatically applied lateral stress is held constant, or varied

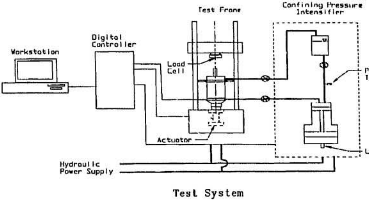

Figure 3.1: Test Apparatus.

depending on the stress path. In the present setup independent control of axial stress and pressure was possible.

3.2 Test Setup

The outline of the test apparatus is shown in Figure 3.1 and the details of sample instrumentation inside the cell are shown in Figure 3.2. The test frame has a capacity of 500 kN and the triaxial cell has a capacity of 70 MPa. The axial actuator and the confining pressure intensifier were controlled independently through a digital controller. This control allowed independent variation of axial and lateral stresses. The complete test system except for the control center was located in a cold room in the Thermal Laboratory at the Faculty of Engineering, Memorial University.

Axial force was measured by a 500 kN capacity load cell mounted between the piston and the cross-head. The axial stress was deduced by dividing the axial force by the actual cross section area obtained from the radial displacement. The confining

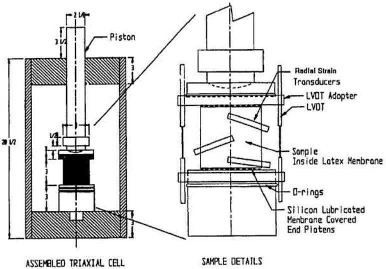

Figure 3.2: Triaxial Test Setup.

pressure intensifier was instrumented with a linear variable displacement transducer (LVDT) at its piston and a pressure transducer. These transducers were used to measure the triaxial pressure and the sample volume change.

Two LVDTs of 12.5 mm range were mounted diagonally at the top and the bottom platens of the specimen. The signals from LVDTs were amplified separately and an averaging circuit was used to obtain an average axial displacement. This procedure reduced the error caused due to tilting of the top platen during the deformation. Axial strain was defined using logarithmic law as,

$$\epsilon_1 = \ln(h/h_0) \tag{3.1}$$

where, h_0 and h are initial and current length of the sample. Details of other measurements and characteristics of the triaxial apparatus are described in the following sub-sections.

3.2.1 Triaxial Cell

The cell was made of nickel-plated high-strength alloy steel. This was the modified version of Rockcell Model 10 triaxial cell. The modifications were made to adapt the cell to the test frame and to increase safety. The bottom of the cell rests on the actuator and the top was screwed on it after installing the sample. All transducers in the cell were wired through high pressure connections. The piston is not attached to the top platen of the sample, but through a ball-socket arrangement (see Figure 3.2). This provided freedom for rotation in the sample. To handle the cell that weighed about 110 kg, the cross-head of the test frame was used as a lift. Figure 3.3 shows this arrangement.

A silicon fluid with a viscosity of 20 cs and a specific gravity of 0.949 at 25°C, was used to pressurize the triaxial cell through the confining pressure intensifier (CPI). The triaxial cell had a fluid capacity of about 18 litres, and it took about 20 minutes to fill it, through an air driven pump from the external reservoir.

3.2.2 Volumetric Strain Measurement

The volumetric strain of ice is an important parameter in ice- structure interaction. For crushed ice, where large volumetric deformation occurs due to pore collapse under high pressure, this parameter has an added significance. In these tests, volumetric strains were deduced by either the fluid displacement method or the radial displacement method.

Fluid Displacement Method

The volumetric strain is often determined from the volume of the fluid displaced from the triaxial cell. For this purpose an LVDT, which was built into the confining

Figure 3.3: Triaxial Cell.

pressure intensifier was used. The LVDT was calibrated to provide the volume of fluid in the intensifier. The fluid displacement method requires complete understanding of the response of the confining fluid and the triaxial cell under variable pressure. The problem could be further complicated by presence of air in the triaxial cell and the pressure intensifier, and inhomogeneous deformation in the sample. Thus, this method is more useful for tests in which confining pressure is constant. For variable confining pressure tests, the radial displacement method was preferred.

The volumetric strain is obtained as,

$$\epsilon_v = \ln(V/V_0), \tag{3.2}$$

where V_0 is the initial volume and V is the current volume of the sample. V was obtained from the intensifier volume change ΔV_i, and the displacement of the piston (cross-sectional area, A_p) of the triaxial cell ΔL_p as,

$$V = V_0 - \Delta V_i + A_p \Delta L_p.$$

Radial Displacement Method

The radial strains were recorded by specially designed radial strain transducers (RST). The RSTs were double cantilever beams mounted with strain gauges. The gauge length of these transducers could be varied to apply a gentle pressure on the sample for mounting. They were further secured on the sample by rubber bands. A change in the sample diameter caused a change in the curvature that was measured in the local strain gauges.

RSTs were mounted at three places, at 1/6, 1/2 and 5/6 height of the sample. An average value was used to obtain the radial strain. The radial strain is defined using logarithmic law as,

$$\epsilon_3 = \ln(d/d_0) \tag{3.3}$$

where d_0 and d are the initial and the deformed diameter of the sample. The volumetric strain as defined in equation 3.2 is,

$$\epsilon_v = \epsilon_1 + 2\epsilon_3. \tag{3.4}$$

3.2.3 Test Control and Data Acquisition

Data from all transducers were conditioned before passing through the MTS digital controller. The controller also had conditioning circuits for system transducers, i.e., the load cell, the pressure transducer and LVDTs in the actuator and the pressure intensifier. The LVDTs and radial transducers mounted on the sample had external conditioning circuits. In total, nine channels of data were recorded, including a time channel. The sampling frequency varied from 10 Hz to 50 Hz for different tests and the stage in the test. For creep tests, the level-crossing method was used with the axial displacement in the sample as the master channel. In the level-crossing method, data are recorded only when the reading of the master channel changes by a pre-defined amount. This reduced greatly the amount of data while preserving all important characteristics.

3.2.4 Lubricated End Platen

Conventionally, in the triaxial tests, the sample contacts the end platens directly. In this arrangement the friction at the platens restricts the lateral deformation in the sample, especially near the ends. This leads to the violation of the basic assumption of uniform and homogeneous deformation in the sample. This can be largely overcome by lubricated end platens. This provides a homogeneous deformation in the sample (Raju et al., 1972). For the present tests on crushed ice, a thin layer of high vacuum silicon grease was applied on the steel platens. The grease was covered by a 0.3 mm thick latex disk. This method reduced the end friction such that the deformation in the sample was nearly homogeneous. The bottom platen contained a vent-hole that was used to apply vacuum in the sample after its preparation.

As the axial deformations were measured between the platens, a bedding error is created by compression of the latex disks. The amount of error depends on the applied pressure. Kolymbas and Wu (1990) have reported compression of latex disks to about 30% for normal stress up to 5 MPa. At higher stresses it is nearly incompressible. In present tests, during shearing, the axial stress was higher than 5 MPa; thus the effect of the bedding error on the sample deformation was neglected.

3.3 Specimen Preparation

3.3.1 Crushed Ice Samples

Crushed ice was produced by crushing ice made from deaerated distilled water. The material below 1.0 mm and above 2.0 mm was rejected. This provided a nearly uniform grain size. The samples of 70 mm diameter and 75 mm length were prepared in a specially designed split mould. Thin latex disks were placed on the silicon-greased lubricated platens. A latex membrane was placed inside the mould. A vacuum was applied between the mould and the membrane to keep it tight during the formation of the sample. The crushed ice was then placed in the mould in four lifts, and compacted by tamping mildly with a steel rod of 38 mm diameter, to reach the target density of 550 kg/m^3. To control the density, the correct mass corresponding to the volume of the mould was measured and used in the preparation of the sample. The top platen was placed on the mould and the membrane was secured on both platens by O-rings. A vacuum of 5 mm mercury was applied, through the vent in the bottom platen, before removing of the mould. This was necessary for the stability of the sample. The vacuum was maintained until the triaxial cell was completely assembled for filling with the confining fluid. The complete process of sample preparation was carried out insitu, on the lower platen of the triaxial cell, mounted on the test frame in the cold room.

In field tests, densities of the order of 750 kg/m^3 are expected, but such high values are unlikely for single-grain material obtained by compaction without breaking or creeping the grains. In the tests the density increased to the level of field tests by application of hydrostatic pressure.

3.3.2 Polycrystalline Ice Samples

To prepare polycrystalline ice samples, the method outlined in Stone et al.(1989) was followed. The seed ice, i.e., crushed ice, was prepared as discussed in the last section. This ice was placed in an air-sealed acrylic mould and was subjected to vacuum of 200 Pa for 2 hours. The mould was then flooded from the bottom with deaerated distilled water cooled at 0°C. After 3 days, the ice was removed from the mould and machined into samples of 71 mm diameter and 96 mm length. Again the lubricated end platens were used. The sample was covered with a latex membrane and secured on both platens by O-rings.

3.4 Test Procedure

Tests were conducted at strain rates in the range 1×10^{-4}/s to 2×10^{-2} /s and confining pressure up to 20 MPa. All tests were conducted at -10°C. The sample was instrumented with a pair of axial LVDTs radially placed across the end platen, and the RSTs at 1/6, 1/2 and 5/6 height of the sample as shown in Figure 3.4. The LVDTs were mounted on the platen by a collar assembly. The averaged output from these LVDTs provided sample displacement, and was sometimes used to control the servo-valve. The confining pressure at the intensifier, the axial force, the axial displacement, the radial displacement, the axial stroke and the amount of displaced fluid were recorded. These values were also displayed on the computer, and provided a clear picture of the state of sample during the test.

The top of the cell was lowered and screwed on the bottom. The high pressure hoses from the pressure intensifier were attached to the triaxial cell and the cell was filled with the confining fluid. Care was taken to expel air from the triaxial cell and the pressure intensifier. In most tests the confining pressure was applied first and then, depending on the stress path, axial compression was applied after 20-30 s. In strain control triaxial tests, a firm contact of the piston on the top platen of the sample is very important. For a compacting material such as crushed ice, this aspect is crucial. The desired confinement was first applied and then the actuator was slowly positioned until a change in the sample height was observed. The average time duration between the sample preparation and testing was about 45 minutes.

3.4.1 Stress Paths and Test Matrix

The effect of stress-path was examined. This is important especially at high stresses when the material ceases to behave as a granular medium. Tests on crushed ice were conducted for hydrostatic compression (HC), conventional triaxial compression (CTC) and simple shear (SS) paths. For polycrystalline ice only CTC and uniaxial tests were done. The test matrix of the program is shown in Table 3.1.

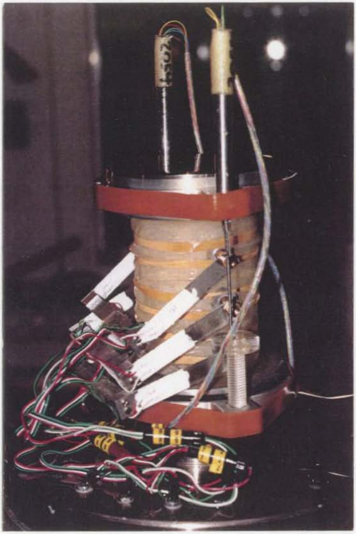

Figure 3.4: Sample with Instrumentations.

Table 3.1: Test Matrix

Test	Material	Path	$\dot{\epsilon}$ /s	σ_3 (MPa)	Comments
1	Ice	CTC	1×10^{-2}	20	no volumetric measurements
2	Ice	CTC	1×10^{-2}	10	no volumetric measurements
3	Ice	CTC	5×10^{-3}	10	
4	C. Ice	CTC	5×10^{-3}	20	loss of control
5	C. Ice	CTC	5×10^{-3}	20	
6	C. Ice	CTC	2×10^{-2}	20	data partially good
7	C. Ice	CTC	5×10^{-3}	5	
8	C. Ice	HC		varied	triangular pulses @ 1 MPa/s
9	C. Ice	HC		varied	20 MPa @ 5 MPa/s loading
10	C. Ice	SS		mean 20	load control loading/unloading
11	C. Ice	SS		mean 20	load control loading/unloading
12	C. Ice	SS		mean 5	load control loading/unloading
13	C. Ice	CTC	2×10^{-2}	5	
14	C. Ice	HC		varied	10 MPa @ 1 MPa/s loading
15	C. Ice	CTC	2×10^{-2}	10	data partially good
16	Ice	CTC	5×10^{-3}	0	sample failure
17	Ice	CTC	1×10^{-4}	0	sample failure by splitting
18	C. Ice	CTC	5×10^{-3}	20,10	load/unload
Data were	also		available for	the	following tests
DT030892	Ice	CTC	1×10^{-4}	0,10	2% uniaxial, creep tests
DT110393	Ice	CTC	1×10^{-4}	20	
DT190393	Ice	CTC	1×10^{-4}	10	

C. Ice = Crushed Ice

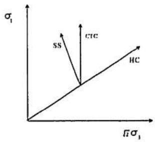

3.4.2 Example Measurements

A sample of measured quantities, for Test 5, i.e. stroke, averaged axial and three radial displacements, axial force, confining stress and displaced fluid volume is shown in Figure 3.5. In this test 20 MPa confining stress was applied and this was followed by axial loading of the sample in stroke control. The soft sample of crushed ice underwent large axial and radial deformation under hydrostatic compression. This caused loss of contact between the sample and the piston. Contact was made during the subsequent axial loading. During this period fluid was displaced from the triaxial cell while keeping the cell pressure constant. Finally a quick unloading in about 0.01 s was done by bringing the stroke down and releasing the confinement.

3.4.3 Volumetric Strains

Two methods of measuring volumetric deformations, i.e., first from the radial and the axial displacements in the sample, and the second, using the fluid displacement from the pressure intensifier are discussed in Section 3.2.2. For Tests 3 and 5 the volumetric strains from these methods are presented in Figure 3.6 for comparison. The sign convention for volumetric strain is that the compaction is positive in Figure 3.6 and in all future references. Both methods have captured the trend in the volumetric deformation for loading in these CTC tests, but the quick unloading was shown only by the first method. The volumetric strain in this thesis is evaluated from radial and axial displacements unless otherwise stated. The delay in fluid response to sudden piston movement made the fluid displacement method unreliable in those conditions; this method was used as a backup measurement.

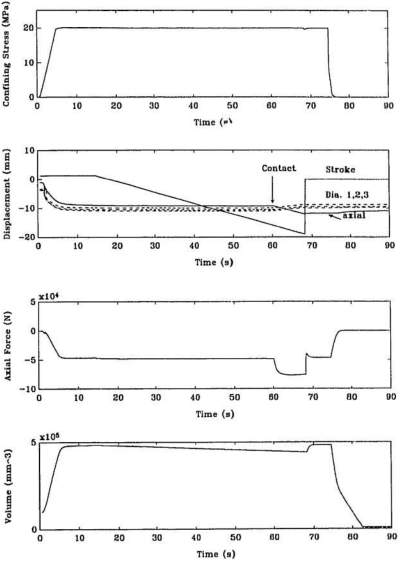

Figure 3.5: Details of measured quantities for test 5.

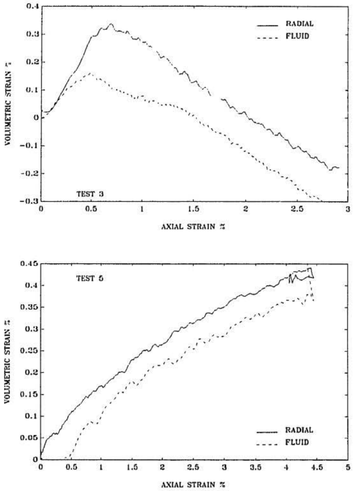

Figure 3.6: Volumetric strain from the radial displacements and the displaced fluid volume for tests 3 and 5.

3.5 Microstructural Observations

In this section a method of characterizing the structure of the tested materials is discussed. The micro-structures were observed in thin sections before and after the tests. Thin sections were prepared by sectioning and microtoming at -10°C. The sample was sectioned and frozen on a glass plate using cold water drops. The surface was shaved until it was smooth. The section was then scraped and refrozen upside down on another glass plate for final shaving until the thickness was about 0.2 mm. A thin section of polycrystalline ice before a test is shown in Figure 3.7. Using the line counting method, average grain size is 2.5 mm.

3.5.1 Crushed Ice

Due to the weakness of inter-granular bond between crushed ice particles, especially when the material is not compressed at high pressure, sectioning of the sample is not feasible. Some filler liquid is required to strengthen the structure. The general requirement for the filler is that it should be water-insoluble liquid, supercooled a few degrees below the matrix (ice) melting point and melt above laboratory temperature (Perla, 1982). Diethyl phthalate, a colourless liquid, melting point -3°C, which may be supercooled more than 5 degree, satisfies these requirements.

The cold room temperature was set at -10°C. The ice specimen was placed in a tray and the liquid filler (supercooled at the cold-room temperature) was poured into the tray. When the specimen is fully saturated, the cold room temperature is reduced to -20°C. The filler hardened when nucleated with some frozen scrap particles of the filler liquid. The sample solidified in less than two hours. First time, high degree of supercooling was required to freeze the filler. This was achieved by placing the tray in liquid nitrogen.

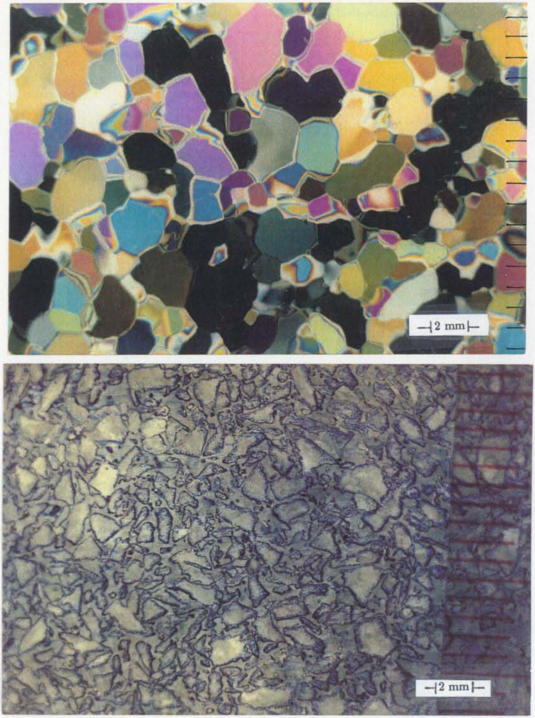

Figure 3.7: Thin sections before a test of (top) polycrystalline ice observed through cross polaroids, and (bottom) crushed ice observed in direct light.

The sectioning and microtoming was done in the cold room at temperature of about -15°C. The sample was sectioned and frozen on a glass plate. The surface of the section was shaved for smooth appearance and polished gently with a high quality lens cleaning tissue. This was left undisturbed at laboratory temperature for about 10 minutes so that the sublimation of the ice etches an observable boundary around the ice filler interface. The gentle polishing is an essential step for removing surface asperities for the enhanced contrast.

The contrast for photomicrography of the polished surface was improved by gently painting through a water insoluble marker pen. The surface is gently polished again with a lens tissue. This process causes trapping of ink in the crevices at the ice-filler boundary, thus increasing the contrast. A thin section prepared by this method for crushed ice before test is shown in Figure 3.7. The average grain size of 0.6 mm was obtained by the line counting method.

3.6 Summary

Triaxial strength and creep tests were conducted on fresh water polycrystalline ice and crushed ice. These two materials represent various states in ice failure and flow during ice-structure interaction. The axial force, the axial and radial deformations in the sample, the confining pressure, and the flow of fluid from the pressure intensifier were measured. Specially designed end-platens were used to ensure homogeneous deformation in the sample. The crushed ice samples were prepared in a split mould, while polycrystalline ice samples were prepared by machining. Tests were conducted at confining pressure up to 40 MPa and strain rate up to 2×10^{-2}. This sections were made from samples before and after tests.

Chapter 4

Results of Triaxial Tests

4.1 Introduction

In this chapter, the results of the triaxial tests described in the last chapter are presented. First, homogeneous and isotropic conditions in the sample during testing are examined. This is followed by triaxial test results and basic interpretations of the material responses of crushed ice, polycrystalline ice and damaged polycrystalline ice. Thin sections from various samples after tests are also presented. Compressive stresses and strains are taken as positive. The axial strains are positive and the radial strains are negative. The positive volumetric strains show compaction. The stress difference is difference between the axial stress σ_1 and the confining pressure σ_3.

4.2 Homogeneity and Isotropy

In the present test program, special care was taken to ensure homogeneous deformation in the sample. The success of the test set-up can be observed by the measured quantities during the test and final sample dimensions. The axial and three radial

Table 4.1: Sample dimensions after tests (in mm)

	Test 5	Test 3
Initial dimensions:		
Length	75	96
Diameter	70	71
Final dimensions:		
Length	64.5, 64.3, 64.6	94.2, 94.1, 94.1
Diameter at 1/6	60.3, 59.6, 60.5	71.7, 71.8, 71.7
Diameter at 1/2	60.5, 58.8, 60.5	71.7, 71.7, 71.7
Diameter at 5/6	61.6, 59.6, 60.0	71.8, 71.8, 71.8

strains are presented in Figure 4.1 for a crushed ice test and a polycrystalline ice test. The three radial strains were nearly identical for the crushed ice test. This confirms the homogeneous and the isotropic deformation in the sample. In the polycrystalline ice sample, the latex disk on the platen seems to cause at the ends. This was critical in uniaxial tests where at high strains samples failed by splitting.

After the test, sample dimensions were measured at about 120° apart for length and three diameters (1/6, 1/2 and 5/6 of length from top). The result presented in Table 4.1 show homogeneous deformation. Other test samples also deformed homogeneously. Photographs of samples after a test are presented in Appendix A.

4.3 Crushed Ice

The triaxial tests on crushed ice were conducted at hydrostatic compression, conventional triaxial compression, and simple shear stress-paths. In this section, the results of these tests are presented and the material behaviour in general is discussed.

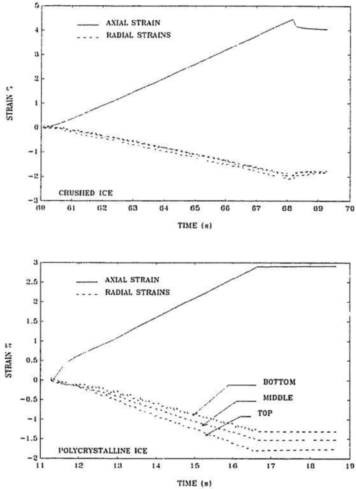

Figure 4.1: The axial and radial responses of crushed ice and polycrystalline ice.

4.3.1 Hydrostatic Compression

The low density of crushed ice (550 kg/m^3) makes it very sensitive to hydrostatic compression. The response of the material to hydrostatic loading is presented in Figure 4.2. In this test triangular pressure pulses of 20 s duration interval were applied on the sample at 200 seconds interval. The loading rate was 1 MPa/s, and was followed by unloading in 0.01 sec. Figure 4.2 shows pressure volumetric response and break-up of this response in the axial and the radial strains obtained from the measured displacements. At initial crush-up strength of about 0.5 MPa, large deformations occur in the sample. This is because of fracture of pre-existing sintered bonds in the material. This crush-up behaviour is commonly observed in sintered-porous materials such as sandstone and metals (Johnson and Green, 1976).

Although the loading path is hydrostatic compression (HC), i.e., $\sigma_1 = \sigma_2 = \sigma_3$ axial strain is not equal to the radial strain, especially at low pressures. This initial anisotropy is due to the method of sample preparation. The crushed ice is stiffer in the axial direction than in the radial direction. Similar results have been reported for loose sand (Oda, 1972; Kolymbas and Wu, 1990). At higher pressures, the sample deformation is nearly isotropic. The pressure-volume relation is highly non-linear, where the bulk modulus also increases with compaction.

Figure 4.2 also shows volumetric relaxation after unloading. This shows that the deformation also has some component of delayed elastic deformation, besides elastic and irrecoverable deformations. Figure 4.3 shows time-dependent volumetric deformation obtained from hydrostatic compression for various triaxial tests. The samples were hydrostatically compressed at certain loading rates and then the pressure was held constant. This figure also shows good repeatability in present tests.

A thin-section of test 8 after loading is shown in Figure 4.4. Due to extensive crushing, the average grain size has reduced greatly from the original size of 1 mm,

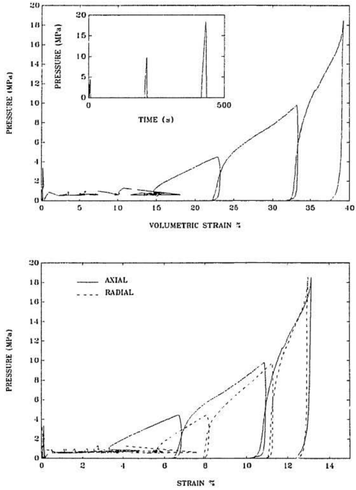

Figure 4.2: Response of crushed ice due to hydrostatic loading (Test 8). The applied pressures are shown inset.

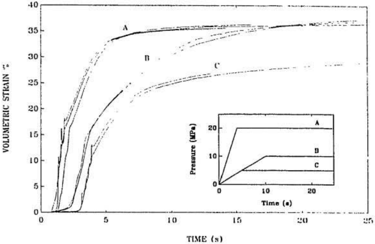

Figure 4.3: Response of crushed ice due to hydrostatic loading. The applied pressures are shown on at the bottom.

except in some islands of original grains. An enlarged section is also shown in this figure. It seems that the larger grains are protected by fine grains that were created by crushing of critical grains. The pores are entrapped at the triple points of some larger grains and at their grain-boundaries. These thin-sections are very similar to those obtained from medium-scale indentation tests (Standler et al., 1993).

4.3.2 Conventional Triaxial Compression

In a conventional triaxial compression (CTC) test, hydrostatic stress is applied first and held constant throughout the test. The sample is then axially deformed, or stressed. In the present tests, samples were axially deformed at a constant strain rate starting 30 seconds after the desired hydrostatic pressure had been reached. This allowed minimization of volumetric creep in the sample without excessive sintering of grains.

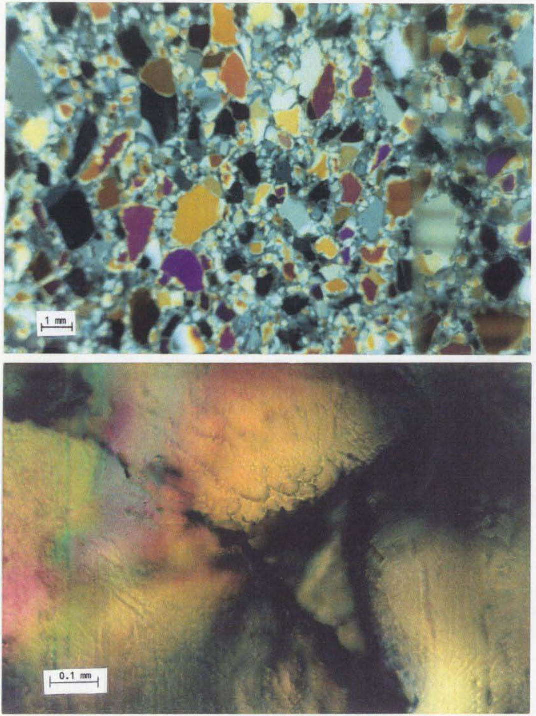

Figure 4.4: Thin-section of crushed ice sample after a hydrostatic test (top) and enlarged section (bottom) of a typical triple junction showing pores. The average grain size has reduced from the original size of 1 mm.

The responses of crushed ice for CTC tests are shown in Figures 4.5-4.7 for various confinements and strain rates. In the slower tests the material undergoes large compaction during axial loading, while in the faster test, the effect of compaction is reduced by dilatation caused by brittleness in the material. The rate effect is clearly visible for low strains. The material behaviour is highly nonlinear. The Young's modulus at loading is about 4.54 GPa for 20 MPa tests and 4.3 for 5 MPa tests.

Test 18 and test 5 were conducted at the same strain rate and confinement, but at different time at which axial load was applied. In test 18 axial load was applied after 20 minutes compared to 30 seconds in test 5 and other tests. More sintering resulted in a strong material, with the strengths comparable to that of polycrystalline ice.

4.3.3 Tests in Octahedral Plane

In CTC tests, as discussed in the last section, the confining pressure is held constant while the axial stress is increased. This leads to an increase in mean stress, $p = (\sigma_1 + 2\sigma_3)/3$ on the sample. The material is subjected to both shear and a change in pressure. For a time-dependent pressure-sensitive material like crushed ice, CTC tests are complex tests for theoretical modelling. To isolate the shear response, simple shear (SS) tests are suitable. These tests are in the octahedral plane. The hydrostatic pressure $(\sigma_1+2\sigma_3)/3$ is maintained constant. The sample is loaded by increasing axial stress by $\delta\sigma$, while the lateral stress is reduced by $\delta\sigma/2$.

Figure 4.8 shows a strength test and Figure 4.9 show creep tests in this plane. Again as in CTC tests, the volumetric response to shear is compaction. This is due to the porous nature of the material; shear leads to better packing of grains. At unloading the material shows delayed-elastic relaxation. The relaxation is larger in test 12 than in test 11. Due to larger mean pressure in test 11 and shear stresses, grains were crushed into fine powder, and the deformation had a large viscous component.

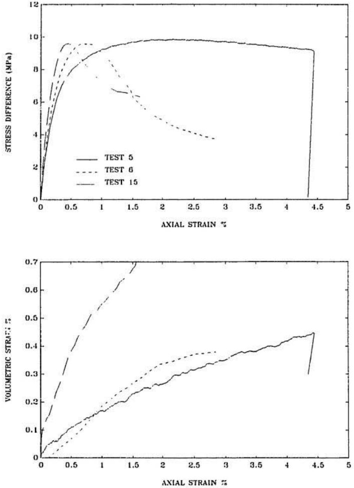

Figure 4.5: Stress-strain response of crushed ice to conventional triaxial compression (Test 5: strain rate 0.005/s, σ_3=20 MPa, Test 6: strain rate 0.02/s, σ_3=20 MPa, and Test 15: strain rate 0.02/s, σ_3=10 MPa).

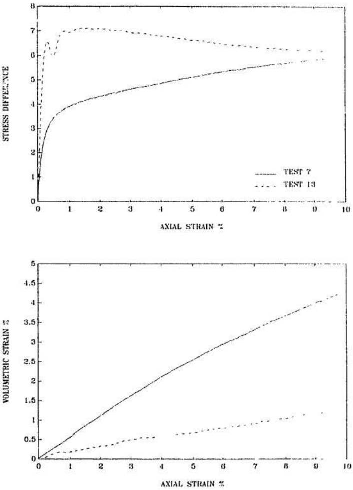

Figure 4.6: Stress-strain response of crushed ice to conventional triaxial compression (Test 7: strain rate 0.005/s, σ_3=5 MPa, and Test 13: strain rate 0.02/s, σ_3=5 MPa).

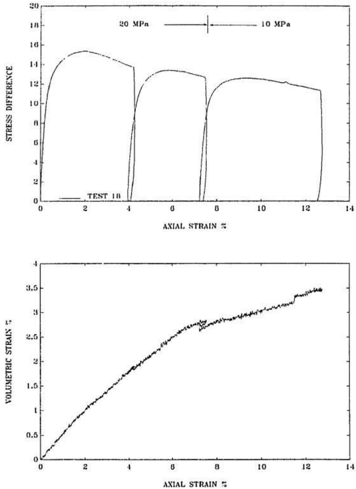

Figure 4.7: Stress-strain response of crushed ice to conventional triaxial compression at strain rate 0.005/s, and confining pressures 20 MPa and 10 MPa.

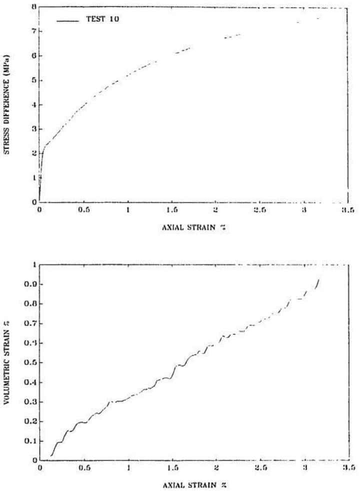

Figure 4.8: Stress-strain response of crushed ice at simple shear path with the mean pressure of 20 MPa.

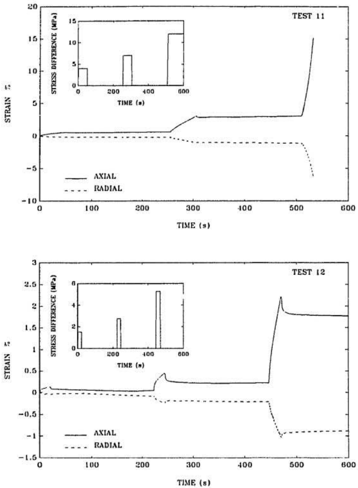

Figure 4.9: Creep response of crushed ice at simple shear path with mean pressure of 20 MPa in test 11, and 5 MPa in test 12. The applied stress difference is shown inset.

This can be observed from the thin-sections of these tests as shown in Figure 4.10.

The calculated volumetric-strains from Figure 4.9 for test 11 are presented in Figure 4.11. The compaction increases with the application of shear stress, though the mean pressure is constant. Similar observation can made from Figure 4.8. These results show that the pressure volume relationship depends on the stress-path. In other words, the volumetric response depends on the shear stresses applied on the sample apart from hydrostatic stresses.

4.3.4 Strength of Crushed Ice

Based on the CTC tests, the strength profile for various confining pressures can be constructed. Figure 4.12 shows the peak deviatoric stress and mean pressure relationship for two strain rates. In the test range, the strength is independent of rate of deformation of the sample. The strength is strongly pressure-dependent for pressures lower than 10 MPa. This is consistent with other frictional materials. For higher pressures, the strength is pressure independent as in metals.

4.4 Polycrystalline Ice

Uniaxial and triaxial strength tests of polycrystalline ice at constant strain rate are presented in Figures 4.13 and 4.14 respectively. The material first compresses due to an increase in hydrostatic pressure caused by increase in axial stresses. When shear stress is large, cracks are formed, which lead to dilatation. Based on the initial loading, the elastic modulus is 9.7 GPa and Poisson's ratio 0.33.

In Figure 4.15, the creep response of polycrystalline ice for 10 MPa and 20 MPa confining pressure is shown. It should be noted that the stresses are not very high, and changes in the microstructure of polycrystalline ice are suppressed by large con-

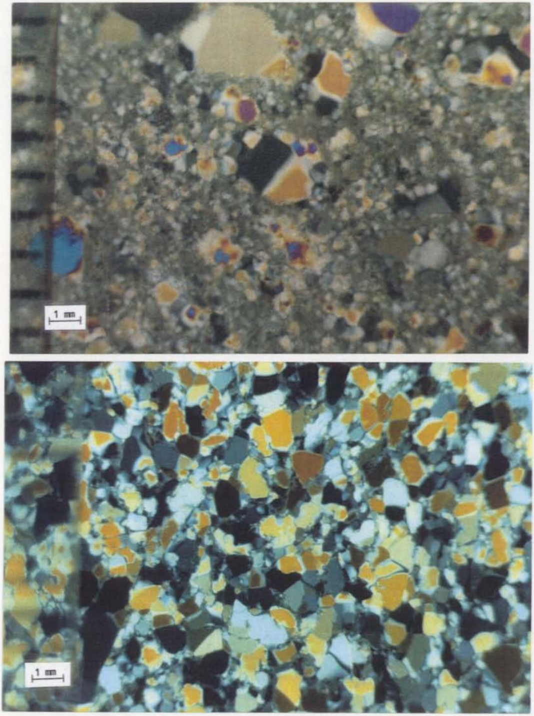

Figure 4.10: Thin-sections of samples after test 11 (top) and test 12 (bottom). Large shear stress and confining pressure in test 11 caused crushing of ice into fine grains similar to those observed in field.

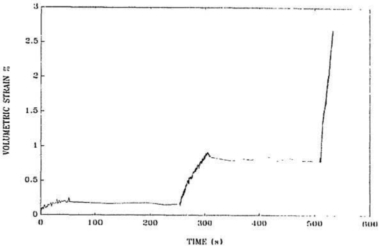

Figure 4.11: Effect of shear stresses on the volumetric response of crushed ice in simple-shear stress-path (test 11).

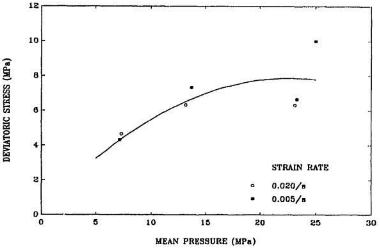

Figure 4.12: Strength of crushed ice.

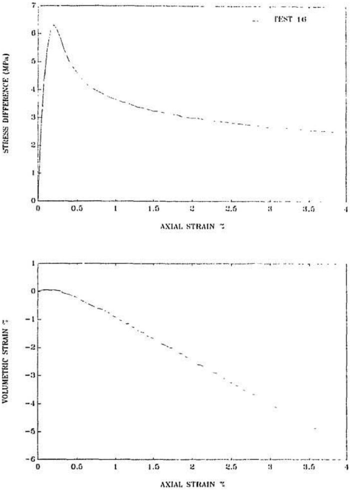

Figure 4.13: Stress-strain response of polycrystalline ice under uniaxial loading at 1×10^{-4}.

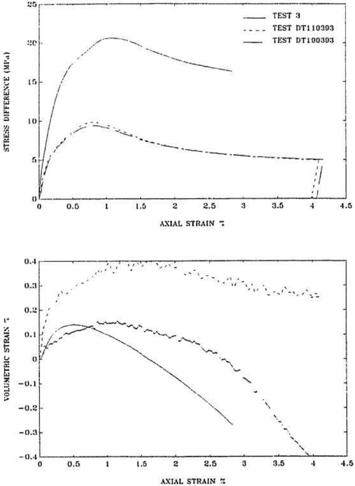

Figure 4.14: Stress-strain response of polycrystalline ice under triaxial loading (Test 3: σ_3=10 MPa, strain-rate 0.005/s, Test DT190393: σ_3=10 MPa, strain-rate 1×10^{-4}/s, and Test DT110393: σ_3=20 MPa, strain-rate 1×10^{-4}/s).

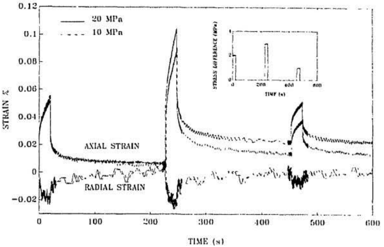

Figure 4.15: Creep response of polycrystalline ice at 10 MPa and 20 MPa confining pressure. The applied stresses are shown inset.

fining pressures. This can be verified from the radial strains that are always less than half the axial strains. The elastic response, as expected, does not change with the confinement, but the creep strains increase with increasing confinement. This is completely opposite to triaxial creep behaviour of other materials such as steel and rocks (McCormick and Ruoff, 1971), which shows decrease in creep strains with increase in the confinement. This behaviour in these materials is attributed to a decrease in the grain boundary sliding with increase in the confinement.

The minimum creep rate for material under pressure is often assumed to follow the equation

$$\dot{\epsilon}_{\text{min}} \propto \exp[-(Q_d + pV_d)/kT] \tag{4.1}$$

where Q_d is the activation energy, p is the hydrostatic pressure, V_d is the activation volume, k is Boltzmann's constant, and T is absolute temperature. This equation can estimate creep under pressure for many geological materials and metals, for which under normal working conditions, the activation energy and volume do not vary greatly with temperature and pressure. Such materials include limestone, rock salt, tin and zinc (McCormick and Ruoff, 1971).

The major difference between ice and other materials is that ice is normally at high homologous temperature. In the present work, and often in the field, the ambient temperature is about 0.96 times the melting temperature in Kelvin. High pressures result in large activation energies, and a decrease in the activation volume. Jones and Chew (1983) have estimated these physical parameters for ice for pressures up to 60 MPa. Such change causes an increase in both the grain-boundary sliding and intra-granular deformation in crystals. As pressure is applied, there is a transient increase in the temperature of ice (Gagnon and Sinha, 1991). This may increase creep strains, but cannot solely explain the increase in creep strains.

Rigsby (1958) studied the effect of confining pressure on the creep behaviour of single crystals, and observed that the creep strain-rate increased with pressure. He attributed this change to the reduction of melting point at high confining pressure. Polycrystalline ice samples have also shown similar behaviour (Haefeli et al., 1968, as reported by Jones, 1982). Jones and Chew (1983) observed that minimum strain rate decreases slightly as hydrostatic pressure is increased from 0 to 15 MPa, then increases more rapidly from 30 to 60 MPa. These high pressure creep observations were done for secondary creep, and not for primary creep which is of main concern here. A confining pressure of 20 MPa decreases the melting point only by 1.5°C. At some critical locations, e.g., where there are large stress concentrations, large changes to the melting temperature may occur.

Creep tests were also conducted on pre-damaged ice samples, where pre-damaging was done uniaxially at a constant strain-rate by applying 2% strain at the strain rate of 1×10^{-4}/s. The result of this test is presented in Figure 4.16. Dilatation of about

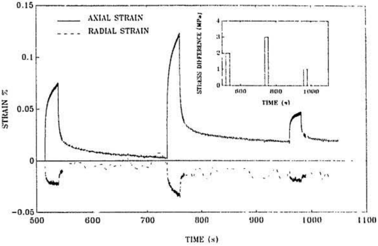

Figure 4.16: Creep response of pre-damaged ice at 10 MPa confining pressure. The applied stresses are shown inset (Test DT030892.)

3% was observed during the predamaging process. Upon the application of confining pressure, closing of cracks was not instantaneous, but rather time-dependent. When axial stresses were applied the rate of densification and axial creep strain-rate were enhanced. This behaviour is similar to that of crushed ice.

Thin sections of ice after tests DT030892 and 3 is presented is Figure 4.17 and 4.18. The appearance of the damaged ice resembles to that of crushed ice sample after test. Here again islands of big grains are surrounded by finely-crushed grains that were recrystallized by pressure-sintering. Cracks are formed at critical inhomogeneity such as grain-boundaries. This can be observed from these thin-sections, though sections are taken after axial strain of about 4%.

Under uniaxial stresses, ice is very brittle. The high rate of damage results in lower strength of ice. Cracks are open and aligned to the maximum principle stress-direction by extending several grains. The cracked material is highly anisotropic at

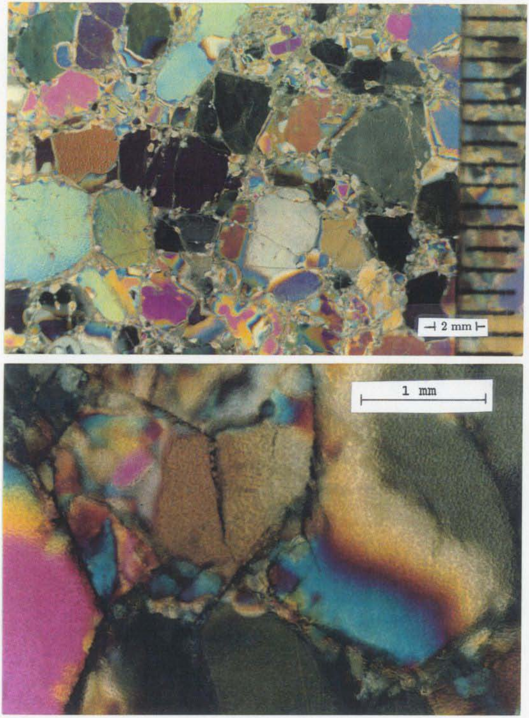

Figure 4.17: Horizontal thin-sections after test DT030892 (top). The enlarged section (bottom) shows cracking and micro-crushing between crack surfaces.

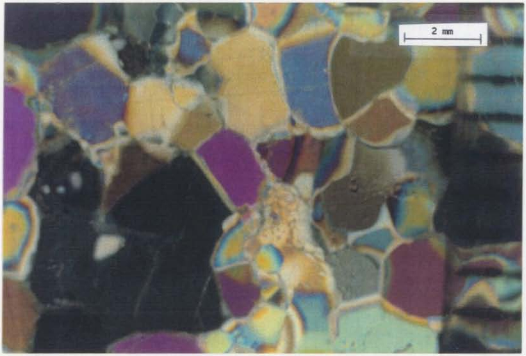

Figure 4.18: Vertical thin-sections after test 3. Because of damaging in triaxial state, there are fewer cracks than Figure 4.17 with no preferred orientation.

large strains. Failure is usually by axial splitting in the sample due to extension of one or many critical cracks.

When confining pressure is also applied, cracks are arrested in regions of higher fracture toughness, or, lower stress. Cracks are distributed uniformly (Figure 4.18), and the material behaviour is nearly isotropic. The average length of crack is of the order of the grain size. Further damage is more stable than uniaxial case. After certain confinement, the strength curve seems independent of confinement, e.g., at the strain-rate of 1×10^{-4} test DT110393 and DT190393 show similar response, but different from the uniaxial response in Figure 4.13. The difference is in dilatation that was suppressed by larger confinement.

4.5 Summary

This compaction of crushed ice is time-dependent, and is enhanced several fold when shear stresses are applied. In the slower tests, material undergoes large compaction during axial loading, while in the faster test, the effect of compaction is reduced by dilatation caused by brittleness in the material. The rate effect is clearly visible for low strains. The strength is strongly pressure-dependent for pressures lower than 10 MPa. For higher pressures, the strength is pressure-independent as in metals.

Under uniaxial stresses, polycrystalline ice is very brittle. Cracks are open and aligned to the maximum principle stress-direction by extending several grains. Failure is usually by axial splitting in the sample due to extension of one or many critical cracks. When confining pressure is applied, cracks are arrested at natural boundaries such as triple junctions. This resulted in an increase in strength. Cracks are distributed uniformly, and the material behaviour is nearly isotropic. Further damage is more stable than in the uniaxial case. For confining pressure more than 10 MPa, the strength is independent of confinement.

Thin-section studies of samples after tests show that due to extensive crushing, the average grain size has reduced greatly from the original size. The larger grains are protected by fine grains that were created by crushing of critical grains.

Chapter 5

Theory of Growing Damage

5.1 Introduction

In this chapter, a continuum theory to describe a material with growing damage due to microstructural changes in presented using generalized J-integral. The effect of individual microstructures and their growth is studied by averaging at a scale that is much larger than the size of microstructures such as grains and microcracks themselves. In viscoelastic materials damage can be nearly time-independent when loading is fast, but at slow loading it is dependent on time (Leckie, 1978; Schapery, 1981; Cocks and Leckie 1987). For nonlinear viscoelastic problems, a method due to Schapery (1991) and based on a modified superposition method is validated for polycrystalline ice. A mechanical method based on the reduced time characterization due to Schapery (1969) and Jordaan et al. (1991) is also presented.

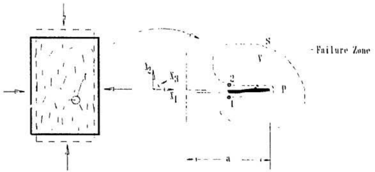

Figure 5.1: Geometry of a microcrack.

5.2 Growth of Microcracks

A theory of material with distributed cracks can be obtained by modelling growth of microcracks (Schapery, 1981). High stresses cause damage and failure of the material at the crack tip. To model this process, the highly damaged material at the crack tip need not to be modelled explicitly, but emphasis can be laid on the continuum surrounding the crack tip, the conditions of which can predict stress and deformation at the crack tip.

5.2.1 Generalized J-Integral

For linear elastic and elastoplastic fracturing solids, J-integral theory (Rice, 1968) has been successfully applied to initiation of crack growth. The J-integral is a basic crack-growth controlling parameter, and accounts for the geometry of cracks and applied load. Schapery (1984, 1986) has presented a parameter analogous to the J-integral for crack growth in nonlinear elastic and nonlinear viscoelastic materials.

An idealized crack geometry is shown in Figure 5.1. In the unstrained state, the crack surfaces near the tip are assumed to be planar and coincide with the local x_1x_3

plane, a plane perpendicular to the page. It is further assumed that the crack tip P is straight and parallel to the x_3 axis, i.e., it is in plane strain state. If the tractions T_i on the surface S shown in Figure 5.1, and body forces per unit volume F_i produce the displacement response u_i in a body, the equilibrium equations are

$$\frac{\partial \sigma_{ij}}{\partial x_j} + F_i = 0, \tag{5.1}$$

where stresses σ_{ij} and surface traction T_i are related through the unit normals n_i by

$$T_i = \sigma_{ij} n_j. \tag{5.2}$$

A potential function W and a body force potential W_F are assumed to exist with the property that

$$\sigma_{ij} = \partial W / \partial u_{i,j} \tag{5.3}$$

$$F_i = -\partial W_F / \partial u_i. \tag{5.4}$$

To meet the requirements of continuum theory, the material enclosed within the arbitrary surface S of Figure 5.1 should not contain any cracks. To achieve a path-independent integral that is useful in fracture analysis, the body is assumed homogeneous with respect to local x_1 axis. Multiplying Equation 5.1 by $-\partial u_i / \partial x_1$, and integrating over volume V, the result is

$$d \equiv \int_V \left[\frac{\partial}{\partial x_1}(W + W_F) - \frac{\partial}{\partial x_j}\left(\sigma_{ij} \frac{\partial u_i}{\partial x_1} \right) \right] dV. \tag{5.5}$$

Changing the volume integral to surface integral over the surface S, and using Equation 5.2, the resulting equation is

$$d \equiv \int_S \left[(W + W_F) n_1 - T_i \frac{\partial u_i}{\partial x_1} \right] dS. \tag{5.6}$$

Let the crack tip P (the leading edge of the highly damaged mass) be straight and parallel to x_3 axis for a short distance l_3. The contribution of potential energy from the crack surface other than zones in contact is zero, thus the energy contribution of any surface of length l_3 outside the damaged zone is equal to the value

$$J \equiv (1/l_3) \int_{S_1} \left[(W + W_F) n_1 - T_i \frac{\partial u_i}{\partial x_1} \right] dS, \tag{5.7}$$

where S_1 is the portion of S not included along the failure zone over the length l_3. In the region of cracks, highly damaged material may be present. Tractions may be on crack surfaces as friction, or it may be open. This is unlike Rice's J-integral where crack surfaces were assumed to be traction free. Equation 5.7 reduces to Rice's J-integral by omitting body forces.

5.2.2 Power-Law Materials

Power-law nonlinearity of stress and strain often represents realistic behaviour in some materials. The complementary energy per unit volume for a power-law material is

$$W'(\sigma' \sigma_{ij}) = |\sigma'|^{r+1} W'(\sigma_{ij}), \tag{5.8}$$

where σ' and r are constants. The linear theory results with $r = 1$. The stresses σ_{ij} in this equation are for a reference state $\sigma' = 1$. Stresses in other states are obtained as

$$\sigma_{ij}' = \sigma' \sigma_{ij}, \tag{5.9}$$

thus, by the definition, strains are

$$\epsilon_{ij}' = \frac{\partial W'(\sigma' \sigma_{ij})}{\partial \sigma_{ij}'} \tag{5.10}$$

or,

$$\epsilon_{ij}' = \text{sign}(\sigma') \sigma'^{r} \frac{\partial W'(\sigma_{ij})}{\partial \sigma_{ij}} = \text{sign}(\sigma') |\sigma'|^{r} \epsilon_{ij}. \tag{5.11}$$

These equations are also valid for cracking solids. When tractions on crack faces are not zero they must vary with σ' in the same way as the stress distribution, e.g., friction force should be proportional to normal force.

For power-law materials, Schapery (1986) derived an equation for quasi-static crack growth as

$$\frac{da}{dt} = f_1 J^k, \tag{5.12}$$

where k is a positive constant and f_1 reflects the properties of the crack-tip material. The J-integral is equal to the strain energy release rate:

$$J = -\frac{\partial W}{\partial A}, \tag{5.13}$$

where A is area of the crack surface. Using the definition of the complementary energy, $W' = \sigma_{ij}\epsilon_{ij} - W$, J can be presented as

$$J = \frac{\partial W'}{\partial A}. \tag{5.14}$$

Using Equations 5.8 and 5.14, 5.12 is written as

$$\frac{da}{dt} = f_1 |\sigma'|^{k(r+1)} \left(\frac{\partial W'}{\partial A}\right)^k. \tag{5.15}$$

For penny-shaped crack of radius a, $\partial W'/\partial A = f_2 a$, where f_2 is a constant. The integration of Equation 5.15 yields

$$a^{1-k} - a_0^{1-k} = (1-k) f_2^k \int_0^t f_1 |\sigma'|^{k(r+1)} dt, \tag{5.16}$$

where a_0 is the initial crack radius. If $k > 1, a \to \infty$ at time $t = t_f$ (failure time), then

$$\frac{a_0^{1-k}}{(k-1) f_2^k} = \int_0^{t_f} f_1 |\sigma'|^{k(r+1)} dt. \tag{5.17}$$

Using this equation, the failure time t_f of a crack can be found implicitly.

In a polycrystalline material, microcracks are arrested at a length equal to the grain size. This causes a sudden decrease in the growth rate when the crack tip reaches a grain that lies across the crack plane. Though Equation 5.17 does not reflect the arrest, no assumptions are needed regarding the crack geometry. This is because the propagation of crack occurs at high-speed, and the time spent in the propagation is negligible compared to the failure time t_f.

The left side of Equation 5.17 may vary from crack to crack, thus producing different failure times. For i^{th} crack, let the left side is denoted by S_i and the resulting failure time by t_i as

$$S_i = \int_0^{t_i} f_1 |\sigma'|^{k(r+1)} dt. \tag{5.18}$$

Schapery (1991) has described the cracking process using Equation 5.18. A crack is assumed to have no effect until it has reached its arrested size, then sudden softening in the material occurs. To account for the effect of microcracking, complementary energy is also function of S_i, i.e., $W' = W'(\sigma_{ij}, S_i)$. The increase in W' increases with the increase in S_i as shown in Figure 5.2. There are so many closely spaced microcracks that the curve in Figure 5.2 may be smoothened out, and S_i can be taken as a smooth function S, as

$$S = \int_0^t f_1 |\sigma'|^q d\tau, \tag{5.19}$$

where $q = k(r+1)$.

Instead of using the mechanism of crack growth as described by Equation 5.12, Equation 5.19 can be derived for a general state of damage. Let the phenomenological law for the m^{th} change in microstructure be

$$\frac{da_m}{dt} = f_1 |\sigma'|^q F_m(a_m), \tag{5.20}$$

where F_m is function of a_m, which represents any microstructural parameter, e.g., size of a cavity, number of cracks or broken bonds, that accounts for failure. From Equation 5.20

$$\int_0^t \frac{da_m}{F_m(a_m)} = \int_0^t f_1 |\sigma'|^q dt = S, \tag{5.21}$$

which is same as Equation 5.19.

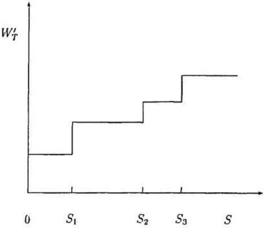

Figure 5.2: Effect of sudden growth and arrest of microcracks on the complementary density.

5.2.3 Material Under Axial Deformation and Pressure

Following Schapery (1990a), the theory developed in the last section can be specialized for a prismatic cylindrical specimen subjected to confining pressure σ_3 and axial strain ϵ. Here it is desirable to define the strain energy in terms of the volumetric strain ϵ_v and axial strain ϵ. If ϵ_v is the dilatation and $S_m (m = 1, 2, ..)$ are damage parameters, the von Mises stress $s = (3/2s_{ij}s_{ij})^{1/2}$ can be defined, as in Chapter 2 by the strain energy $W = W(\epsilon, \epsilon_v, S_m)$ as

$$s = \frac{\partial W}{\partial \epsilon}, \tag{5.22a}$$

and the mean stress p as

$$p = \frac{\partial W}{\partial \epsilon_v}. \tag{5.22b}$$

Let a dual energy density $W_d = W_d(\epsilon, p, S_m)$ be defined as

$$W_d = W + p\epsilon_v. \tag{5.23}$$

This definition of the dual energy is useful in extending the results from proportional loading such as uniaxial tests to triaxial tests where the all-around pressure σ_3 remains constant. Equation 5.23 can be differentiated as

$$\frac{\partial W_d}{\partial \epsilon} d\epsilon + \frac{\partial W_d}{\partial p} dp + \frac{\partial W_d}{\partial S_m} dS_m = \frac{\partial W}{\partial \epsilon} d\epsilon + \frac{\partial W}{\partial \epsilon_v} d\epsilon_v + \frac{\partial W}{\partial S_m} dS_m + p d\epsilon_v + \epsilon_v dp, \quad (5.24)$$

and the axial stress and dilatation can defined in terms of the dual energy by comparing Equations 5.22 and 5.24 as

$$s = \frac{\partial W_d}{\partial \epsilon}, \quad (5.25a)$$

and

$$\epsilon_v = \frac{\partial W_d}{\partial p}. \quad (5.25b)$$

In this theory dilatation is related to the area under the strain-strain curve. This can be shown by differentiating Equation 5.25a with respect to p and Equation 5.25b with respect to ϵ and equating them to yield

$$\frac{\partial s}{\partial p} = \frac{\partial \epsilon_v}{\partial \epsilon}, \quad (5.26)$$

or,

$$\epsilon_v = \frac{\partial}{\partial p} \int_0^{\epsilon} s d\epsilon. \quad (5.27)$$

As pointed out by Schapery (1990a), the applicability of Equation 5.27 for predicting dilatation depends on the existence of the potential W_d exactly, regardless of the number of structural parameters.

In some materials the effect of large confinement is to reduce damage. Ice is one such material (see Chapter 4). Here the J-integral of Equation 5.13 for penny-shaped cracks of radius a is proportional to $f_3 a$, where f_3 is also a function of the confining pressure apart from the properties of the crack tip material. Following the procedure of the last section, a relation for the damage function S can be obtained as

$$S = \int_0^t f_3 |\sigma'|^q d\tau. \quad (5.28)$$

The function f_3 is determined experimentally.

5.3 Viscoelastic Media

Using the correspondence principle described in Chapter 2, a theory for polycrystalline ice can be developed. The change of microstructure due to cracking, as formulated in the last section for nonlinear-elastic materials, is equally valid for viscoelastic materials when strains in the reference elastic problem are

$$\epsilon_{ij}^{e} = \frac{1}{E_R}\int_0^t C(t-\tau)\frac{d\epsilon_{ij}}{d\tau}d\tau, \tag{5.29}$$

where $C(t)$ is the relaxation modulus and is related to the creep function $D(t)$ of the virgin material through Laplace transform. The reference strains $\epsilon_{ij}{}^{e}$, which are also denoted as pseudo-strains depend on material properties and are defined by the complementary pseudo-energy W^e as,

$$\epsilon_{ij}^{e} = \frac{\partial W^e}{\partial \sigma_{ij}}. \tag{5.30}$$

Stresses in reference elastic problem and viscoelastic problem are the same. The inverse of Equation 29 is

$$\epsilon_{ij} = E_R\int_0^t D(t-\tau)\frac{d\epsilon_{ij}{}^{e}}{d\tau}d\tau. \tag{5.31}$$

The material nonlinearity and damage both enter in Equation 5.29 via the pseudo-strain ϵ_{ij}^{e} while the creep compliance $D(t)$ is assumed to be linear over useful stress range. This analysis is based on Schapery's (1981) modified superposition principle (MSP).

For proportional loading and power-law cracking the pseudo-strain follows the power-law relationship in stress and a measure of damage $g(S)$. For the uniaxial loadings

$$\epsilon^{e} = \text{sign}(\sigma)\left|\frac{\sigma}{\sigma_0}\right|^{r} g(S), \tag{5.32}$$

where $\sigma = \sigma(t)$ is the axial stress and σ_0 is a positive constant. The microstructural parameter S is the same as that described in Equation 5.19 and is written as

$$S = \int_0^t f_1 \left(\frac{\sigma}{s_1}\right)^q d\tau \tag{5.33}$$

where $q = k(r+1)$, and s_1 is a positive constant. The parameter f_1 accounts for complexities at crack tips such as changes in temperature and hardening. For many brittle failure cases f_1 can be taken as unity. The linear elastic relationships are recovered when r=1, $g(S)$=1 and $D = 1/E_R$. When r=1, but $g(S) \neq 1$ the nonlinearity is introduced by the damage function. For $r \neq 1$, the representation of elastic behaviour by Equation 5.29 is nonlinear.

Equations 5.31 to 5.33 can be used to predict strain or stress in terms of the other variable. In the following sections various material parameters required in this theory are obtained using experimental data presented in Chapter 4.

5.4 Polycrystalline Ice

Polycrystalline ice is brittle and exhibits nonlinear viscoelastic deformation for a wide range of engineering applications. When this material is stressed, some energy is stored due to elasticity in the material and new surfaces created by microcracking, while most of it is dissipated in inelastic deformations. Microcracks of grain size are formed initially along the grain boundary when loaded. For sustained loadings the density of cracks increases, and they are also observed across the grain. This microstructural process increases the material compliance. The theory described in this section and used for predicting the behaviour of polycrystalline ice is due to Schapery (1991).

5.4.1 Creep Compliance and Nonlinearity

The viscoelastic response of polycrystalline ice without damage can be written in terms of three components, the elastic component, the delayed elastic component, and the steady state creep component. For creep of ice a widely used formulation is due to Sinha (1979), and is presented as follows.

$$\epsilon(t) = \frac{\sigma}{E} + \frac{c_1}{a}\left(\frac{\sigma}{E}\right)\left(1 - e^{-(a_T t)^b}\right) + \dot{\epsilon}_0(\sigma/\sigma_0)^n t \tag{5.34}$$

where σ is the uniaxial creep stress, E is the modulus of elasticity, a is the grain size, a_T and $\dot{\epsilon}_0$ are functions of temperature, and c_1, b, σ_0 and n are constants. The grain size in the present tests is 2.5 mm, and $\sigma_0 = 1$. Other material constants used are the same as given by Sinha. The first term in this equation is linear elastic strain. The second term is the delayed elastic strain, which is associated with grain boundary sliding. This component is responsible for time-dependent relaxation in ice. The third is viscous flow caused by dislocation movements and crystalline slip.

Equation 5.34 is not in the framework of the viscoelasticity theory as presented in Chapter 2. This is due to the nonlinearity caused by the constants b and n. The material behaviour is highly nonlinear for sustained long-term loads, although for high-rate tests, which are of primary concern in this analysis, nonlinearity is not expected to be a major factor. The creep compliance of the form

$$D(t) = D_0 + D_1(t/t_0)^b + D_2(t/t_0), \tag{5.35}$$

is used in the viscoelastic theory of ice described earlier. In Equation 5.35, D_0 is inverse of elastic modulus of ice, and D_1, D_2 and b are positive constants. The term t_0 is used here for dimensional purposes. The creep compliance $D(t)$ can be determined by constant-stress tests on ice. As this component does not contain the effect of damage, tests should be conducted at stresses low enough to avoid microcracking in the material. In the present analysis $D(t)$ is determined by fitting Equation 5.35 in Equation 5.34, which is well established for the uniaxial creep response of polycrystalline ice, and the parameters defining $D(t)$ are obtained as $D_0 = 1/9500/\mathrm{MPa}$, $D_1 = 2 \times 10^{-5}/\mathrm{MPa}$, $b = 0.28$ and $D_2 = 2 \times 10^{-6}/\mathrm{MPa}$. The short-term creep of ice is independent of the state of stress.

The nonlinearity parameter r of Equation 5.32 can be obtained by fitting Equation 5.35 in 5.34 for some useful stress ranges. Its value is highly dependent on stress range and the time of loading and varies from one, i.e., linear, for time ≤ 20 s to three for long term loadings. Thus, if the short-term response is of main concern, e.g., peak stress in constant strain rate tests, r can be taken as unity. It should be noted that $r = 1$ does not mean that the material response is linear. Nonlinearity can still be introduced by the damage function, which indirectly is nonlinear function of stress (see the theory presented in the last section).

5.4.2 The Damage Function

The final stage in the modelling is to determine the damage function $g(S)$ in Equation 5.32 and the constants s_1 and q to describe the microstructural parameter S defined in Equation 5.33. Schapery (1991) has presented a procedure to determine of these values. Creep tests can again be used to determine this function using Equations 5.32 and 5.33, but here the damage parameter also should change; in other words tests should be conducted at high stresses. Another approach is to use results of constant strain-rate tests.

If the strain history is known, Equation 5.32 can be inverted to give the stress history for uniaxial tests as

$$\sigma = \mathrm{sign}(\epsilon^e)\frac{\sigma_0(\epsilon^e)^{1/r}}{g^{1/r}} \tag{5.36}$$

Now differentiating Equation 5.33 and substituting σ from Equation 5.36, the result is

$$\frac{dS}{dt} = \left(\frac{\sigma_0}{s_1}\right)^q \frac{(\epsilon^e)^{q/r}}{g^{q/r}}, \tag{5.37}$$

or,

$$\int_{S_0}^{S} g^{q/r} dS = \left(\frac{\sigma_0}{s_1}\right)^q \int_0^t (\epsilon^e)^{q/r} d\tau = S_\epsilon, \tag{5.38}$$

where S_0 is initial damage in the material. For an initially undamaged material $S_0 = 0$. The parameter S_ϵ replaces S as the microstructural parameter. The corresponding value of the damage function $g_\epsilon(S_\epsilon)$ is obtained from Equation 5.36 as

$$g_\epsilon = g^{-1/r} = \frac{\sigma}{\sigma_0}(\epsilon^e)^{-1/r}. \tag{5.39}$$

For constant strain-rate $\dot{\epsilon}$, Equation 5.29 and Equation 5.38 become

$$\epsilon^e = \dot{\epsilon} h_1 \tag{5.40}$$

$$S_\epsilon = \left(\frac{\sigma_0}{s_1}\right)^q \dot{\epsilon}^{q/r} h_2, \tag{5.41}$$

where h_1 and h_2 are given as

$$h_1 = \frac{1}{E_R}\int_0^t C(t) dt \tag{5.42a}$$

$$h_2 = \int_0^t h_1^{q/r} dt. \tag{5.42b}$$

The parameters σ' and E_R are taken as unity. The relaxation modulus $C(t)$ was obtained numerically by the deconvolution of $D(t)$.

Using test results, the function $g_\epsilon(S_\epsilon)$ from Equation 5.39 and S_ϵ from Equation 5.41 can be evaluated. At least two tests at different rates are required for evaluation of the damage function. From Equation 5.41

$$\log S_\epsilon = \log\left[\left(\frac{\sigma'}{s_1}\right)^q \dot{\epsilon}^{q/r}\right] + \log h_2. \tag{5.43}$$

Since g_ϵ is function of S_ϵ, the value of g_ϵ for tests at different speed will be same. Thus, a curve of $\log g_\epsilon$ verses $\log h_2$, for each strain rate, will differ from another by a horizontal translation equal to the first term on right hand side of Equation 5.43. For a curve, if s_1 is selected such that the term in the square bracket is unity, then other curves can be brought on this curve by moving them by a horizontal distance $-\log\left(\frac{\dot{\epsilon}}{\dot{\epsilon}_R}\right)^{q/r}$. An iterative method is then used to obtain the quantity q.

5.4.3 Uniaxial Tests

For a general representation, the function $g(S)$ is needed to be explicitly defined. An exponential function of the form

$$g = e^{\lambda(S+S_0)}, \tag{5.44}$$

where λ is a positive constant and S_0 is the initial damage, is considered for prediction. This function is simple to use, and reflects softening due to damage. Using Equations 5.38 and 5.39, g_ϵ can be obtained as

$$g_\epsilon = \left[\frac{\lambda q}{r} S_\epsilon + e^{\lambda S_0 q/r}\right]^{-1/q}. \tag{5.45}$$

For constant-strain rate tests, stresses are obtained using Equations 5.39 and 5.40 as

$$\sigma = \sigma_0 g_\epsilon (\dot{\epsilon} h_1)^{1/r} \tag{5.46}$$

The predicted stress-strain response of uniaxial tests at two strain rates is presented in Figure 5.3 along with the measured responses. The value of the parameters used in this analysis are presented in Table 5.1. From Figure 5.3, it can be seen that the theory can model the material behaviour in the strength tests.

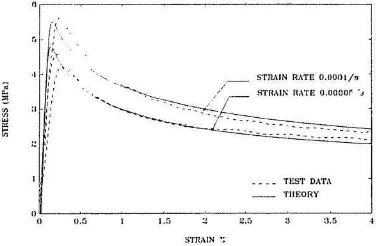

Figure 5.3: The measured and predicted uniaxial response of polycrystalline ice in constant strain-rate tests.

Table 5.1: Material constants for polycrystalline ice to be used with the modified superposition method.

$s_1 = 1$; $\sigma_0 = 1$; $E_R = 1$; $r_1 = 1$;

$q = 5$; $r = 1$; $\lambda = 1.2 \times 10^{-5}$; $S_0 = 0$;

For uniaxial Tests:

$D_0 = 1/9500/\text{MPa}$; $D_1 = 2 \times 10^{-5}/\text{MPa}$; $D_2 = 2 \times 10^{-6}/\text{MPa}$; $b = .28$;

For triaxial Tests:

$D_0 = 1/9500/\text{MPa}$; $D_1 = 5 \times 10^{-5}/\text{MPa}$; $D_2 = 5 \times 10^{-6}/\text{MPa}$; $b = .28$;

5.4.4 Triaxial Tests

The triaxial response of polycrystalline ice is different from that under uniaxial conditions. This difference is mainly caused by cracking-induced anisotropy under uniaxial stress states. At low confinement, cracks are oriented along the maximum principal stress. In some cases the cracking may be localized along the maximum shear stress plane. Further, in uniaxial tests, large dilatation occurs in the post-peak regime. The effect of dilatation is to increase compliance in the material. Under large triaxial stresses, localization of cracks is suppressed and cracks are uniformly oriented in all directions, overall damage is less, and the material is essentially isotropic and homogeneous.

In Figure 5.4, the creep response compiled from Figure 4.15 of polycrystalline ice for 10 MPa and 20 MPa confining pressure is shown with the predicted response based on Equation 5.34. For uniaxial response, Sinha's equation for creep, which is comprehensively established for polycrystalline ice is also presented. It should be noted that the applied creep stresses are not very high, and changes in the microstructure of polycrystalline ice is suppressed by large confining pressures. The elastic response, as expected, does not change with the confinement, but the creep strains increase with increasing confinement (also see Chapter 4). For the present work, the creep coefficients as required in Equation 5.35 under triaxial conditions are obtained as $D_0 = 1/9500/\mathrm{MPa}$, $D_1 = 5 \times 10^{-5}/\mathrm{MPa}$, $D_2 = 5 \times 10^{-6}/\mathrm{MPa}$ and $b = 0.28$.

The nonlinearity parameter r in Equation 5.32 can be estimated by creep tests on virgin or predamaged ice (predamaging of ice was done by loading it uniaxially at a constant strain rate of 1×10^{-4} /s to 2% axial strain). Again the stresses should be low enough so that the damage state in the material does not change during the creep process. Figure 5.5 shows strains from triaxial creep response (adopted from Figure 4.16) at 10 MPa confining pressure on a pre-damaged ice sample. As in uniaxial

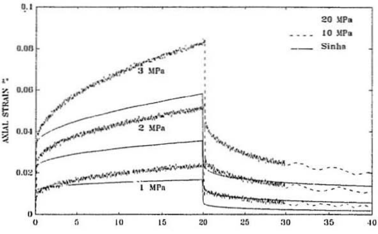

Figure 5.4: Creep behaviour of polycrystalline ice at various confining pressure, and prediction based on Equation 5.34. The applied creep stresses are shown for each set.

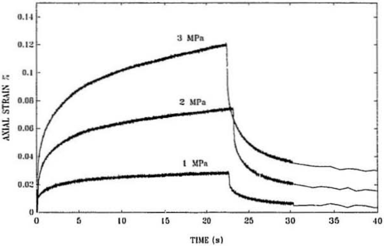

Figure 5.5: Creep behaviour of pre-damaged polycrystalline ice at 10 MPa confining pressure. The applied creep stresses are shown.

tests, the nonlinearity may vary with stress and duration of a test. From Figures 5.4 and 5.5 and the creep compliance of Equation 5.35, the parameter r can be found. For present analysis r is taken as unity. It is noted that the presented creep tests are short-term tests, do not present highly nonlinear behaviour of polycrystalline ice. In long-term creep tests, microstructural changes such as void formation along the grain boundaries and recrystallization occurs, thus creep and damage are inseparable.

In Section 5.2.3 a theory for a material undergoing axial deformation while subjected to confining pressure was presented. Let the pressure-dependence of the parameter f_3 in Equation 5.28 be represented as

$$f_3 = f_1(p_a/\sigma_3)^{r_1}, \tag{5.47}$$

where p_a is the atmospheric pressure and r_1 is a constant. When $\sigma_3 = p_a$, Equation 5.47 reduces to the uniaxial relation. For triaxial tests, the lower value of f_3 results in less damage in the material. The predicted behaviour for a triaxial test is presented in Figure 5.6 along with the test results. As it can be seen from Figure 5.6, the theory is in good agreement with the experimental data.

5.5 A Mechanical Model

In this section an alternative theory to characterize polycrystalline ice is presented. This theory is due to Schapery (1969) and Jordaan and McKenna (1988), and is derived using the thermodynamics of irreversible processes (see Section 2.5.3). The nonlinearity is contained in a "reduced time" $\psi(t)$, which is an implicit function of stress in the creep formulation. The resulting theory is similar to linear viscoelastic theory. The shift factor can be function of other nonlinear effects, e.g., temperature

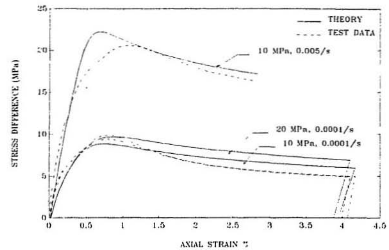

Figure 5.6: The measured and predicted triaxial response of polycrystalline ice. The applied strain rates and the confining pressures are shown for all tests.

and aging. The integral form for uniaxial stress-state is

$$\epsilon(t) = \int_0^t D[\psi(t) - \psi(\tau)] \frac{d\sigma(\tau)}{d\tau} d\tau. \tag{5.48}$$

The reduced time is defined as

$$\psi(t) = \int_0^t \frac{d\tau}{a_d[\sigma(t)]} \tag{5.49}$$

The function a_d is a shift factor and can be considered as a stress-dependent viscosity. The variation of this function is shown in Figure 5.7. For a power-law creep material, $\dot{\epsilon} = (\sigma/\sigma_0)^n \dot{\epsilon}_0$, the shift factor is given as,

$$a_d = \eta(\sigma) = \frac{\sigma_0^n}{\sigma^{n-1}\dot{\epsilon}_0} \tag{5.50}$$

where σ_η and $\dot{\epsilon}_0$ are reference stress and strain-rate respectively.

An approximate mechanical model of ice behaviour as given in Equation 5.34 can be presented in the Burgers model of Figure 5.8, which is combination of Maxwell unit

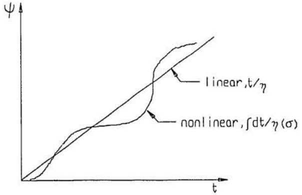

Figure 5.7: Schematic variation of reduced time.

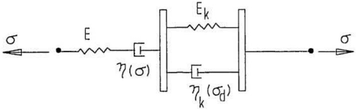

Figure 5.8: A mechanical model.

and Kelvin unit in series (Jordaan and McKenna, 1988). Note that the nonlinearity is preserved by making viscosity of the dashpot stress-dependent as in Equation 5.50. The spring elements are linear in this model. The delayed elastic terms in Equation 5.34 is shown by the Kelvin unit in Figure 5.8. The total strain from this model can be presented as summation of three components as

$$\epsilon = \epsilon^{el} + \epsilon^{d} + \epsilon^{c}, \tag{5.51}$$

where the three components are instantaneous elastic ϵ^{el}, delayed elastic ϵ^{d} and steady-state creep ϵ^{c} terms respectively.

If the mechanical model is subjected to a creep stress σ applied at t=0, and stress in the dashpot in the Kelvin unit is σ_d, the resulting strain ϵ_k in the Kelvin unit is

$$\epsilon_k(t) = \frac{\sigma}{E_k}\left[1 - \exp(-\int_0^t \frac{E_k}{\eta_k(\sigma_d)} d\tau)\right], \tag{5.52}$$

where $\eta_k(\sigma_d)$ is defined by Equation 5.50 with $\sigma_d = \sigma$.

For triaxial stress-states, Equation 5.48 can be presented in terms of shear and hydrostatic components as,

$$e_{ij} = \frac{1}{2}\int_0^t J_D[\psi(t) - \psi(\tau)]\frac{\partial s_{ij}}{\partial \tau} d\tau \tag{5.53a}$$

$$\epsilon_{kk} = \int_0^t J_V[\psi(t) - \psi(\tau)]\frac{\partial \sigma_{kk}}{\partial \tau} d\tau \tag{5.53b}$$

where J_D and J_V are shear and bulk creep function respectively. The stress and strain are decomposed in deviatoric and volumetric components as

$$\sigma_{ij} = s_{ij} + \frac{1}{3}\delta_{ij}\sigma_{kk} \tag{5.54a}$$

$$\epsilon_{ij} = e_{ij} + \frac{1}{3}\delta_{ij}\epsilon_{kk} \tag{5.54b}$$

In Equation 5.53, ψ is obtained by Equation 5.49, where the uniaxial stress σ is replaced by von Mises stress s defined as

$$s = \left(\frac{3}{2}s_{ij}s_{ij}\right)^{1/2}. \tag{5.55a}$$

Similarity equivalent shear strain is defined as

$$e = \left(\frac{2}{3}e_{ij}e_{ij}\right)^{1/2}. \tag{5.55b}$$

von Mises stress and equivalent shear strain reduce to axial stress and shear strain for uniaxial stress-state. For proportional loadings, the deviatoric stresses and strains are related through von Mises stress and equivalent strain as

$$e_{ij} = e\frac{s_{ij}}{s} \tag{5.56}$$

5.5.1 Damage Model

Each strain component in Equation 5.51 is influenced by the presence of microcracks. The elastic and delayed elastic strains dominate the early stage of damage during rapid loading, while for the long-term events the permanent deformations dominate. The basic assumption of the damage model is that the material is homogeneous and isotropic, and remains so throughout the damaging process.

Elastic Strain

Budiansky and O'Connell (1976) have derived the moduli of the damaged material using a self-consistent method, in terms of the crack density. The material is assumed to contain a population of randomly-oriented penny-shaped cracks. Cracking leads to degradation in the modulus of the material. Let an internal state variable λ_d represent the accumulation of damage; the Young's modulus E of the damaged material is given by,

$$E = E_0(1 - \lambda_d) \tag{5.57}$$

where E_0 is the Young's modulus of the virgin material.

The damage parameter λ_d is related to the degraded Poisson's ratio ν and a crack density parameter λ_1 through

$$\lambda_d = \frac{16(1-\nu^2)(10-3\nu)}{45(2-\nu)}\lambda_1. \tag{5.58}$$

An approximate relation between Poisson's ratio of the damaged material, and that of virgin material, ν_0 is

$$\nu \approx \nu_0(1 - \frac{16}{9}\lambda_1). \tag{5.59}$$

Once ν is evaluated from Equation 5.59, the damage parameter λ_d can be obtained from Equation 5.58, and the Young's modulus of the damaged material can be estimated. The corresponding relation of Equation 5.57 for the bulk modulus K of the cracked material is

$$\frac{K}{K_0} = 1 - \frac{16(1-\nu^2)}{9(1-2\nu)}\lambda_1, \tag{5.60}$$

where K_0 is the bulk modulus of the virgin material. The crack density parameter λ_1 is related to the number of cracks N and the average crack length a as

$$\lambda_1 = Na^3. \tag{5.61}$$

The crack density parameter λ_1 is a state variable and can be described by external variables such as stress and strain. In Chapter 4, it was observed that changes in microstructure at large strains are due to breaking of grains into fine grains. This continuous crushing process results in an enhanced inelastic activity and there is no significant change in elastic stiffness of the material. The crack density in a sample can be estimated for small strains, especially for pre-peak behaviour by direct observation, but for advanced damage processes, the crack and grain-boundary densities are inseparable. Here a state variable more general in nature than crack density is needed. For the present analysis, the state variable λ_1 is considered as a measure of damage whose change causes change in the material stiffness according to Equations 5.57-5.59.

An expression similar to that of the damage parameter defined in Equation 5.28 can be assumed for change in λ_1 as

$$\dot{\lambda}_1 = f_3 \left(\frac{s}{s_1}\right)^q . \tag{5.62}$$

where f_3, q and s_1 are constants and s is equivalent shear stress. Equation 5.62 assumes that crack density increases at any stress. This may be true to for a predamaged material. In polycrystalline ice a threshold value of stress s_c is needed to initiate cracks. When stresses are lower than s_c, deformation does not contain contributions from damage. Further, test results presented in Chapter 4 show that strength of the material increases with an increase in hydrostatic pressure. Equation 5.62 can be modified to account for hydrostatic pressure and the threshold stress as

$$\dot{\lambda}_1 = f_3(p) \left(\frac{s - s_c}{s_1}\right)^q , \quad s > s_c \tag{5.63}$$

where parameter f_3 is a function of hydrostatic pressure p. The threshold stress depends on grain size and the degree of confinement. Based on experimental data, Kalifa et al. (1989) observed that s_c is related to the confining pressure σ_3 as

$$s_c = 2.47 + 0.4\sigma_3 \tag{5.64}$$

Equations 5.57 and 5.60 are derived for interacting tensile cracks. Cracks are assumed to be open; this is not so in mode II cracks with friction at their surfaces under compressive stresses. However, as the cracking events are directly associated with the dilatation, the assumption of an open crack is not far from the reality. Nemat-Nasser (1989) has noted that ductile materials develop extensive tensile cracks due to wing cracking even in the absence of any overall tensile loads.

Delayed-Elastic Strain

The equivalent delayed-elastic strain rate for the nonlinear Kelvin unit as presented by Jordaan and McKenna (1991) is given by

$$\dot{e}^d = \frac{s^d}{\eta_k(s^d)} \exp(\beta_k \lambda_d), \tag{5.65}$$

where the viscosity η_k is function of the internal stress s^d as defined by Equation 5.50 by substituting s^d for σ. The internal stress depends on the accumulated delayed-elastic strain $e^d = \int_0^t \dot{e}^d dt$. The creep rate is enhanced exponentially by the product of a constant β_k and the damage parameter λ_d. This enhancement is the result of increase in the grain-boundary density due to damage. If the stiffness of the spring in the Kelvin unit is E_k, the internal stress can be obtained as

$$s^d = s - E_k e^d. \tag{5.66}$$

The stiffness E_k is the degraded stiffness and is related to the spring stiffness in the Kelvin unit of the virgin ice according to Equations 5.57 as $E_k = E_{k0}(1 - \lambda_d)$.

Secondary Creep

Cracking enhances secondary creep, the third component in Equation 5.51. Experimental results of Stone et al. (1989) suggest that creep increases exponentially with damage, and can be presented by power law relation between shear stress and shear strain-rate. The multiaxial relation is

$$\dot{e}_{ij} = \dot{\epsilon}_0 \left(\frac{s}{\sigma_0}\right)^{n-1} s_{ij} \exp(\beta_s \lambda_d), \tag{5.67}$$

where β_s is a creep enhancement parameter.

Dilatation

Volumetric deformation due to cracking is the volume occupied by cracks. After cracking as the material undergoes large inelastic deformation, the effect of dilatation in ice is nearly irreversible. Only a fraction of volumetric change is recovered due to elasticity. The confining pressure, if present, tends to suppress opening of cracks, and thus the dilatation.

The dilatation can be obtained by the procedure described in Section 5.2.3, where it was presented as a function of the mean stress, shear stresses and damage parameters (Equation 5.27). Total volumetric strain is assumed to be the sum of the dilatation due to inelastic deformations and the bulk elastic compaction ϵ_v^e as

$$\epsilon_v = \frac{f_d}{p} \int_0^{\epsilon^p} s d\epsilon^p - \epsilon_v^e, \tag{5.68}$$

where f_d is a constant, and ϵ^p is inelastic strain. Equation 5.68 assumes that a work potential exists for inelastic deformations. The second term in Equation 5.68 produces compaction while the first term causes dilatation.

5.5.2 Prediction of Test Results

The predicted results for uniaxial tests are shown in Figure 5.9. The value of the constants used in this analysis are presented in Table 5.2. For a triaxial test the predicted and measured response of polycrystalline ice is presented in Figure 5.10. A good correlation of both the shear and the volumetric response can be observed for the uniaxial test. In the triaxial test (Figure 5.10), the model is able to capture the trend in the behaviour. The difference is in the initial compaction part. The dilatation model was based on the flow deformation, which develops after peak strength. The ability to predict dilatation shows that a work potential exists approximately during damage in ice.

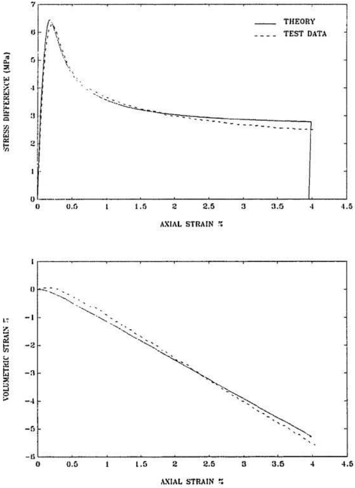

Figure 5.9: Response of polycrystalline ice obtained from the mechanical model when loaded uniaxially at constant strain-rate of 1×10^{-4}. The compaction is positive.

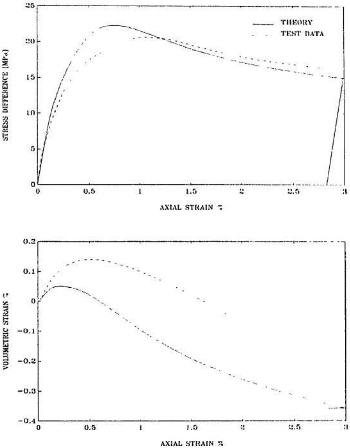

Figure 5.10: Response of polycrystalline ice obtained from the mechanical model and subjected to 0.005 /s strain-rate and 10 MPa confining pressure. The compaction is positive.

Table 5.2: Model Parameters

Elastic Modulus	E_0	9500 MPa
Poisson's Ration	ν	0.3
Elastic Modulus in Kelvin Spring	E_{k0}	$0.8E_0$
Reference Stress	s_0	1 MPa
Damage parameters	q	2
	f_3	$1.5 \times 10^{-3}/p$
Grain size	a	2.5 mm
Secondary Creep Reference Rate	$\dot{\epsilon}_0$	1.76×10^{-7}
Primary Creep Reference Rate	$\dot{\epsilon}_{k0}$	$15 \times \dot{\epsilon}_0$
Creep Exponent	n	3
Creep Enhancement Constant 1	β_s	40
Creep Enhancement Constant 2	β_k	20
Dilatation constant	f_d	0.35

5.6 Summary

In this chapter, two theories to describe the damage in viscoelastic materials were presented. In the first theory, the damage was described by generalized J-integral for nonlinear elastic media, which was extended to nonlinear viscoelastic media using Schapery's correspondence principle. The second theory was based on a mechanical model, which is a Burgers viscoelastic model with nonlinear elements. These theories compared well with the measured response of polycrystalline ice. The first theory is more systematic, has a rigorous basis, and requires fewer parameters. The main disadvantage of this theory is the universality of the nonlinearity. This shortcoming is addressed by the second theory, the mechanical model, which gives a physical description of various components.

Chapter 6

Theory of Crushed Ice

6.1 Introduction

The behaviour of crushed ice is different from that of the parent ice mass due to the larger degree of freedom at the grain boundary and the presence of pores. The discrete nature of the material results in large contact pressures at grain boundaries that in turn may lead to phase change and further crushing of grains. The shear strength of this material is largely dependent on the degree of confinement. At low pressures, crushed ice is similar in behaviour to snow, and can be modeled as a frictional material (Finn et al. 1989; Sayed and Frederking, 1992). Like snow, crushed ice grains stick together by neck growth while in contact with each other and form a matrix.

Under large confinement, the particulate ice looses its discrete and granular nature. Large pressures cause pore collapse and reduced localized shearing deformation due to sintering of the grains. This results in deformation in the grain itself besides grain boundary sliding, and the behaviour of the material is similar to that of polycrystalline ice. The isotropic behaviour of crushed ice can be idealized into a material where uniformly distributed pores and grain boundaries are embedded in an isotropic matrix

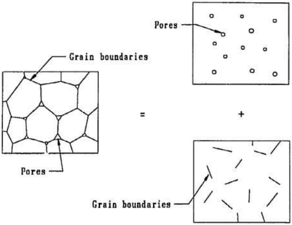

Figure 6.1: The microstructure of crushed ice. The pores and the grain-boundaries are distributed in 3-D space.

as shown in Figure 6.1. The geometry of pores is idealized as spherical, and grain-boundaries are idealized as thin circular disks. It is further assumed that the pores and the grain boundaries do not interact with each other. This condition is applicable for dilute concentrations of pores and grain boundaries.

In Chapter 4, it was observed that under large confinement crushed ice behaviour changes from the friction-dominant deformation to a pressure-independent behaviour, where friction does not play any role at the macro-structural level. A viscoelastic model is more realistic to describe the strength and the deformation behaviour of crushed ice at high pressures.

In the present chapter, a theory to describe the mechanical behaviour of crushed ice under high pressure is presented. A linear-elastic solution based on the equivalent inclusion method is derived. A closed-form solution for nonlinear-elastic materials containing voids and obeying a power-law is also presented. Using the correspondence principles discussed in Chapter 2, elastic solutions are extended to the viscoelastic response of crushed ice. The viscoelastic response is also presented using the mechanical model and results are compared to the material response presented in Chapters 4. The pressure sintering behaviour of crushed ice is also studied.

6.2 Elastic Materials with Pores

A porous material can be treated as a composite material, where the pores are inclusions. Micromechanical models such as the equivalent inclusion method and the self-consistent method can be used for solving this problem. A general analysis for composite material is presented in Appendix B. Here a solution for dilute pores in a homogeneous and isotropic matrix based on Eshelby (1957) and Mura (1982) is presented.

Let the applied stress $\bar{\sigma}_{ij}$ and the resulting strain ϵ_{ij} be related through Hooke's law, i.e.,

$$\bar{\sigma}_{ij} = C_{ijkl}\epsilon_{ij}, \tag{6.1}$$

where C_{ijkl} is the stiffness of the material to be determined. Due to presence of pore a stress disturbance σ_{ij} and corresponding strain ϵ_{ij} is caused. The applied stress and strain are also the averaged total stress $\bar{\sigma}_{ij}+\sigma_{ij}$ and strain $\epsilon_{ij}+\epsilon_{ij}$ in the representative volume, and is presented as

$$\bar{\sigma}_{ij} = \frac{1}{V}\int_V(\sigma_{ij} + \sigma_{ij})dV, \tag{6.2a}$$

and

$$\bar{\epsilon}_{ij} = \frac{1}{V}\int_V(\epsilon_{ij} + \epsilon_{ij})dV. \tag{6.2b}$$

The strain ϵ_{ij} is related to the averaged strain ϵ_{ij} by Eshelby's tensor S_{ijkl} as

$$\epsilon_{ij} = S_{ijkl}(\epsilon_{kl} + \epsilon_{kl}). \tag{6.3}$$

The quantities S_{ijkl} are dependent on the geometry of the pore. Substituting ϵ_{ij} in Equation 6.2, and using pore-fraction c, which is the ratio of the volume of pore to the representative volume of the material, the result is

$$\bar{\sigma}_{ij} = (1-c)\bar{\sigma}^M_{ij}, \tag{6.4a}$$

$$\bar{\epsilon}_{ij} = \frac{c\bar{\epsilon}_{kl}}{\delta_{ik}\delta_{jl} - S_{ijkl}} + (1-c)\bar{\epsilon}^M_{ij}, \tag{6.4b}$$

where $\bar{\sigma}^M_{ij}$ and $\bar{\epsilon}^M_{ij}$ are averaged stress and strain in the matrix M, and are related by Hooke's law as

$$\bar{\sigma}^M_{ij} = C^M_{ijkl}\bar{\epsilon}^M_{kl}, \tag{6.5}$$

where C^M_{ijkl} is the known stiffness of the matrix. Eliminating $\bar{\sigma}^M_{ij}$ and $\bar{\epsilon}^M_{ij}$ from Equation 6.4 by using Equations 6.5 and 6.1, the stiffness of the porous media is

$$\frac{C_{ijkl}}{C^M_{ijkl}} = 1 - \frac{\delta_{ik}\delta_{jl}c}{\delta_{ik}\delta_{jl} - S_{ijkl}}. \tag{6.6}$$

For isotropic materials, Equation 6.6 can be presented in terms of the bulk modulus K and the shear modulus G as

$$\frac{K}{K^M} = 1 - \frac{c}{1 - \frac{1}{3}S_{iijj}}, \tag{6.7a}$$

$$\frac{G}{G^M} = 1 - \frac{c}{1 - 2S_{ijkl}} \quad \text{with } i = k \ \& \ j = l, \tag{6.7b}$$

where, K^M and G^M are the bulk and the shear moduli of the matrix. For spherical pores a closed-from solution for Eshelby's tensor S_{ijkl} is given by Mura (1982) and is presented in Appendix B. This provides

$$S_{ijkl} = \frac{4 - 5\nu^M}{15(1-\nu^M)} \quad \text{with } i = k \ \& \ j = l \tag{6.8a}$$

$$S_{iijj} = \frac{1+\nu^M}{1-\nu^M}. \tag{6.8b}$$

Substituting these values in 6.7, and making use of the relation between the elastic constants, $\nu^M = \frac{3K^M - 2G^M}{2(G^M + 3K^M)}$, the elastic moduli for porous material are written as

$$\frac{K}{K^M} = (1-c) - \frac{3}{4}\frac{K^M}{G^M}c, \tag{6.9a}$$

$$\frac{G}{G^M} = 1 - 5\frac{3K^M + 4G^M}{9K^M + 8G^M}c. \tag{6.9b}$$

In the absence of pores $c = 0$, $K = K^M$ and $G = G^M$. Equation 6.9b predicts, as observed in Chapter 4, a coupling of shear and hydrostatic responses.

6.3 Nonlinear-Elastic Materials with Pores

The solutions for a linear elastic material with pores as described in last section can be extended to nonlinear elastic materials using an incremental method, where at each increment of stress, linear theory is employed to determine stress-strain relationship, by assuming an incrementally linear behaviour for all phases. In this section, a closed-form solution for materials following power-law nonlinearity is presented. This analysis is based on the works of Budiansky et al. (1982), and Duva and Hutchinson (1984).

The pores in the material are assumed to be spherical, isolated and non-interactive. Consider a spherical pore of radius a that is surrounded by the matrix material of radius R (Figure 6.2). Magnitudes of these radii are such that the void volume fraction c of this spherical shell and the porous material is same, i.e.,

$$c = (a/R)^3 \tag{6.10}$$

The matrix is assumed to be isotropic and incompressible. Under uniaxial conditions, stress and strain are assumed to be related by a power-law equation

$$\epsilon = \mathrm{sign}(\sigma)\epsilon_0|\sigma/\sigma_0|^n, \tag{6.11}$$

where ϵ_0 and σ_0 are reference strain and stress respectively. For multiaxial stresses Equation 6.11 can be generalized to yield

$$\epsilon_{ij} = \mathrm{sign}(s)\frac{3}{2}\epsilon_0|s/\sigma_0|^{n-1}s_{ij}/\sigma_0, \tag{6.12}$$

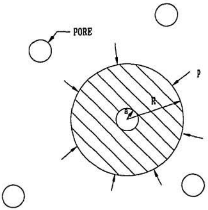

Figure 6.2: A model for the porous material.

where s_{ij} is deviatoric stress tensor, and s is von Mises stress. The complementary energy function W' for the power-law material can be obtained as

$$W' = \frac{\epsilon_0 \sigma_0}{n+1} \left(\frac{s}{\sigma_0} \right)^{n+1}, \tag{6.13}$$

where the definition of strain ϵ_{ij} in terms of W' as

$$\epsilon_{ij} = \frac{\partial W'}{\partial \sigma_{ij}} \tag{6.14}$$

was used. When dilute voids are introduced in this material, the potential of the system is increased. Let the total potential be given by

$$W'_T = W' + f_1(c) W'_v, \tag{6.15}$$

where W'_v defines the change in complementary energy caused by an isolated spherical pore in an infinite matrix, which is subjected to remote stress σ_{ij}, and $f_1(c)$ is a function of the pore-volume fraction c and maps the infinite matrix into the finite domain. Equation 6.15 is of the form of Equation A.1 of Schapery (1984).

6.3.1 Hydrostatic Solution

For materials following power-law nonlinearity, a closed-form solution is possible when the loading is hydrostatic. Let the spherical shell be subjected to a hydrostatic pressure p as shown in Figure 6.2. The boundary value problem is solved in spherical coordinates (r, θ, ϕ). Due to the symmetry of loading this problem is essentially one-dimensional. Let u_r be the radial displacement due to load p, then the strain components are

$$\epsilon_r = \frac{du_r}{dr} \tag{6.16}$$

$$\epsilon_\theta = \epsilon_\phi = u_r/r. \tag{6.17}$$

The incompressibility condition is

$$\epsilon_r = -2\epsilon_\theta, \tag{6.18}$$

or

$$\frac{du_r}{dr} + \frac{2}{r}u_r = 0 \tag{6.19}$$

This equation implies that the most general form of displacement u_r is

$$u_r = \frac{A}{r^2}. \tag{6.20}$$

The equilibrium equation is

$$\frac{d\sigma_r}{dr} + \frac{2}{r}(\sigma_r - \sigma_\theta) = 0. \tag{6.21}$$

The constitutive Equation 6.12 can be written as

$$\epsilon = \text{sign}(\sigma_r - \sigma_\theta)\epsilon_0|(\sigma_r - \sigma_\theta)/\sigma_0|^n, \tag{6.22}$$

Using Equations 6.22 and 6.20, the value of $\sigma_r - \sigma_\theta$ can be obtained. Substitute this value in the equilibrium Equation 6.21, the result is

$$\frac{d|\sigma_r|}{dr} + \text{sign}(\sigma_r)\frac{2}{r}\sigma_0\left(\frac{-2A}{\epsilon_0 r^3}\right)^{1/n} = 0. \tag{6.23}$$

This equation should satisfy the following boundary conditions

$$\text{at} \quad r = a, \quad \sigma_r = 0$$

$$\text{and at} \quad r = R, \quad \sigma_r = p. \tag{6.24}$$

Thus,

$$|p| = \text{sign}(p)\frac{2n}{3}\sigma_0\left(\frac{-2A}{\epsilon_0}\right)^{1/n}[-R^{-3/n} + a^{-3/n}], \tag{6.25}$$

or,

$$A = \text{sign}(p)\frac{\epsilon_0 a^3}{2}\left(\frac{3}{2n}|p/\sigma_0|\right)^n[1 - c^{1/n}]^{-n}. \tag{6.26}$$

A relation for change in pore volume ratio can be obtained from Equation 6.10 as

$$dc = 3c\left[\frac{da}{a} - \frac{dR}{R}\right]. \tag{6.27}$$

The quantities da/a and dR/R in this equation can be obtained from Equation 6.20. The result is

$$dc = 3cA\left[\frac{1}{a^3} - \frac{1}{R^3}\right]. \tag{6.28}$$

or,

$$dc = \text{sign}(p)\frac{3\epsilon_0 c(1-c)}{2}\left(\frac{3}{2n}|p/\sigma_0|\right)^n[1 - c^{1/n}]^{-n} \tag{6.29}$$

The dilatation and the void volume fraction are related as

$$dc = (1-c)d\epsilon_v. \tag{6.30}$$

Wilkinson and Ashby (1975) and Budiansky et al. (1982) have presented a similar formulation for power-law creeping solids unlike power-law nonlinear elastic material in the present analysis.

While sintering pores, which are filled with air, become isolated. Further sintering leads to increase in the pressure in the pores. The effect of this internal pressure is to slow down the sintering process. The internal pressure is given as

$$p_i = \left(\frac{a_0}{a}\right)^3 p_a = \left(\frac{c_0}{c}\right) p_a, \tag{6.31}$$

where a_0 and c_0 are average radius and void fraction at the moment when pores close, and p_a is the atmospheric pressure. In such cases effective pressure $(p - p_i)$ should be used in Equation 6.29.

6.3.2 Solutions for General Triaxial States

For power-law creep, Budiansky et al. (1982) obtained a solution for W_v' using the Rayleigh-Ritz method based on minimum principles applied to the velocity field. A numerical solution is required for the exact analysis. Approximate solutions were also given for high triaxial states when hydrostatic stresses are larger than shear stresses. Another approximate solution applicable for wide range of triaxial states and pore fractions was given by Cocks (1989). The elastic solutions for the materials following a power-law relationship can be deduced from their solution using correspondence principles. As the objective of the present work is to extend the resulting elastic solutions to the viscoelastic solutions for ice, only the approximate solution is considered for simplicity.

Like W', W_v' is also a homogeneous function of order $n+1$. Following Duva and Hutchinson (1984), this can be written in terms of von Mises stress s, and the hydrostatic pressure p, as

$$W_v' = \epsilon_0 \sigma_0 \left(\frac{s}{\sigma_0}\right)^{n+1} f(\alpha, n), \tag{6.32}$$

where

$$\alpha = \frac{3p}{2s},$$

and $f(\alpha, n)$ is a dimensionless function.

The dilatation can be obtained as

$$\epsilon_v = f_1(c)\frac{\partial W_v'}{\partial p} = f_1(c)\epsilon_0 \left(\frac{s}{\sigma_0}\right)^n \frac{\partial f}{\partial \alpha}, \tag{6.33}$$

where f_1 is a function of c. For high triaxiality, $\alpha \gg 1$, Budiansky at al. (1982) have presented an approximate expression for dilatation as

$$\epsilon_v = \text{sign}(\alpha)\frac{3}{2}f_1(c)\epsilon_0\left(\frac{s}{\sigma_0}\right)^n\left(\frac{|\alpha|}{n} - G\right)^n, \tag{6.34}$$

where

$$G = -\frac{(n-1)[n + g(\text{sign}(\alpha))]}{n^2}, \tag{6.35}$$

with $g(1) = 0.4319$ and $g(-1) = 0.4031$. For dilute concentrations, the function $f_1(c) = c$.

For $n = 1$ Equation 6.34 reduces to the exact results. For higher values of n Equation 6.34 predicts strong coupling of hydrostatic pressures and the shearing stresses on dilatation. It is also noted that this equation can predict dilatation even in the absence of the hydrostatic pressure. The high-triaxiality approximation gives good results for $\alpha \geq 3$, and about 30% error for $\alpha = 1.5$.

By Equations 6.33 and 6.34, the function f is obtained as

$$f(\alpha, n) = \frac{n}{n+1}\left(\frac{|\alpha|}{n} - G\right)^{n+1}. \tag{6.36}$$

Using Equation 6.36 in 6.32, total complementary energy for a porous material can be obtained from Equation 6.15 as

$$W'_T = \frac{\epsilon_0\sigma_0}{n+1}\left(\frac{s}{\sigma_0}\right)^{n+1}\left[1 + cn\left(\frac{|\alpha|}{n} - G\right)^{n+1}\right], \tag{6.37}$$

and the strain components as

$$\epsilon_{ij} = \epsilon_0\left(\frac{s}{\sigma_0}\right)^n\left[\frac{3s_{ij}}{2s} + c\left(\frac{|\alpha|}{n} - G\right)^n\left(-\frac{3nGs_{ij}}{2s} + \frac{1}{2}\text{sign}(\alpha)\delta_{ij}\right)\right]. \tag{6.38}$$

For nonlinear materials, the applicability of the dilute concentration results is restrictive. Under hydrostatic loading, where the exact solution exists, a comparison can be made. A pore fraction of $c = 0.001$ increases the dilatation-rate by 30%

above the predicted value when n=3. For large pore-fraction, the interaction of pores must be considered. Cocks (1989) has presented a semi-empirical solution for porous materials that covers the practical range of pore fractions. In ice-structure interaction problems, the pore fraction may be as high as 20%. This solution was obtained by interpolating the results for dilute solution and a concentrated solution. Here the complementary energy of the porous media is not a linear combination of the energies of the matrix material and the pores, but a coupled function of the pore-fraction and is given as

$$W'_T = \frac{\epsilon_0 \sigma_0 (1-c)}{(n+1)} \left(\frac{\bar{s}}{\sigma_0 (1-c)} \right)^{n+1} , \tag{6.39}$$

where

$$\bar{s} = s \left[1 + c \left(\frac{2}{3} + \frac{2n\alpha^2}{(n+1)(1+c)} \right) \right]^{1/2} . \tag{6.40}$$

The strain components can be obtained as

$$\epsilon_{ij} = \frac{3}{2} \epsilon_0 \left(\frac{\bar{s}}{\sigma_0 (1-c)} \right)^n \left[\frac{s_{ij}}{s^2} \bar{s} + \frac{cn}{(n+1)(1+c)} \left(\frac{p}{\bar{s}} \right) \left(\delta_{ij} - \frac{3\alpha}{s} s_{ij} \right) \right] . \tag{6.41}$$

6.4 Grain Boundaries and Fracture

Grain-boundaries are imperfections in a homogeneous material. They are also weak structures, and are subjected to high stress concentrations. When the material is loaded, sintered bonds are broken and large viscoelastic deformation occurs in a thin layer adjacent to the interacting surfaces. There is also dissipation of energy due to friction. The mechanical properties of this thin layer are different from that of the grain material, and they may be considered as disk-shaped inclusions. In Chapter 5, cracks were treated in this fashion showing the similarity between grain boundaries and cracks. Using the solutions of composite materials (Appendix B) the elastic moduli of a material with grain-boundary can be estimated.

The inelastic and anisotropic nature of the ice crystal—creep along the basal plane of ice is about two orders higher than along non-basal planes (Duval et al., 1983)—plays a very important role in the deformation. When loaded, this anisotropy leads to development of large internal stresses in unfavourably oriented grains and their crushing. After crushing stresses are shifted to the neighbouring grains to continue the process of crushing. The result is an increase in grain-boundary density and viscous behaviour of the material. During slower deformations and in a material at high temperature such as ice, new crystals can nucleate and grow at high stress concentration points. This process is called recrystallization. The requirement of the nucleus is that its boundary be mobile (McLean, 1957). When large confining pressures are also applied, which is the case in the "critical zones" in ice-structure interaction, the mobility of grain boundaries may change in unfavourably oriented grains due to pressure melting.

Deformation in a granular material is the result of both sliding and rotation of grains. The change in the grain size causes increases in the freedom of movement at the grain-boundaries and enables the rotation of grains. In this process grains with larger surface area, i.e., elongated grains, are broken. This can be observed from the thin sections of crushed ice prepared before and after a test as presented in Chapters 3 and 4. After tests, the grain size is reduced and they are round. At large deformations grain-boundaries and cracks are indistinguishable. In the present analysis there is no separate treatment of grain-boundaries in particular. The mobile grain-boundaries and their changes are presented by the theory of generalized J-integral of damaging material as presented in Chapter 5.

6.5 Pressure Sintering

In this section sintering of crushed ice under high pressure is examined. The material is assumed to follow power-law creep, $\dot{\epsilon} = \dot{\epsilon}_0(\sigma/\sigma_0)^n$, where $\dot{\epsilon}_0$ is the reference creep rate. The solution of this problem can be obtained by the results presented in Section 6.3 for elastic materials with pores and using the analogy between elastic and viscous solutions, i.e., strain is replaced by the strain-rate. The resulting equation for the sintering of crushed ice based on Equation 6.29 is

$$\dot{\epsilon}_v = \text{sign}(p - p_i)\frac{3\dot{\epsilon}_0 c}{2}\left(\frac{3}{2n}|(p - p_i)/\sigma_0|\right)^n [1 - c^{1/n}]^{-n}, \tag{6.42}$$

where p_i is pore pressure and is given by Equation 6.31. It is noted that the model of sintering presented in Equation 6.42 is valid only when pores are isolated, which is best representative of the final stage of sintering.

Maneo and Ebinuma (1983) studied the densification of snow and observed that pores isolate at the pore-fraction of 0.1. For pore-fractions higher than 0.1 and below 0.4, a cylindrical model of pore is appropriate. The solution for a cylindrical pore is similar to that of the spherical pores, and the final equation can be written as

$$\dot{\epsilon}_v = \text{sign}(p - p_i)2\dot{\epsilon}_0 c\left(\frac{2}{n}|(p - p_i)/\sigma_0|\right)^n [1 - c^{1/n}]^{-n}, \tag{6.43}$$

For the compaction of crushed ice, the simulated behaviour is presented in Figure 6.3 with the test data. Using the values of $\dot{\epsilon}_0 = 8.8 \times 10^{-5}$ that is 500 times that of polycrystalline ice, the power-law exponent n=3.2, and the constant σ_0=1, analysis was performed. The theory and the test data compare well. It should be noted that at the beginning of compaction, large deformations are due to fracture of the sintered bonds. In Figure 6.4 the simulated results are verified for test 8, where pressure pulses were applied on the specimen. The initial pulse is not modelled as the present theory does not cover compaction due to fracturing.

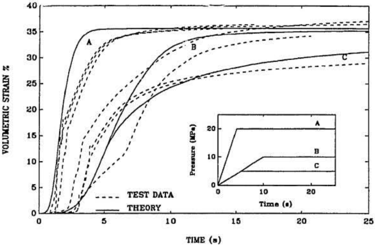

Figure 6.3: Compaction of crushed ice subjected to various hydrostatic pressures. The applied pressure is shown in inset.

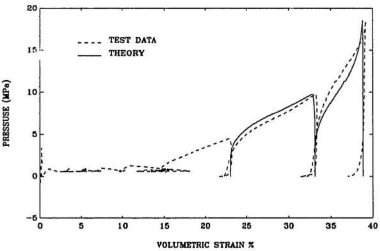

Figure 6.4: Model verification for cyclic compaction of the material.

6.6 Modified Superposition Method

As in Chapter 5, the modified superposition method can be used to obtain the viscoelastic response with pores and grain-boundaries. For a non-linear viscoelastic material

$$e_{ij} = \int_{0^-}^{t} D(t-\tau)\frac{\partial \epsilon_{ij}{}^{e}(s, p, S_k)}{\partial \tau}d\tau, \tag{6.44}$$

where $\epsilon_{ij}{}^{e}$ is a pseudo-strain and is function of the effective shear stress s, the hydrostatic pressure p, and the microstructural parameters $S_k, k = 1, 2, \ldots$ All non-linearity in the material is addressed by $\epsilon_{ij}{}^{e}$. The time-dependent structural parameters S_k account for the dilatation and cracking of sintered crushed ice.

The response of crushed ice has two basic components, the collapse of pores and the breaking of sintered bonds when subjected to shearing stresses. The total complementary energy of crushed ice is combination of the complementary energy of the cracking solid, and increase in the complementary energy due to voids. The treatment of cracked solids due to distributed microstructure was presented in Chapter 5, and is due to Schapery (1981). The increase in the complementary energy due to voids in a power-law nonlinear material was presented in Equation 6.41. Using these theories, the pseudo-strain $\epsilon_{ij}{}^{e}$ for crushed ice can be written as

$$\epsilon_{ij}{}^{e} = \frac{3}{2}\epsilon_0\left(\frac{\bar{s}}{\sigma_0(1-c)}\right)^n\left[\frac{s_{ij}}{s^2}\bar{s} + \frac{cn}{(n+1)(1+c)}\left(\frac{p}{\bar{s}}\right)\left(\delta_{ij} - \frac{3\sigma}{s}s_{ij}\right)\right]g(S), \tag{6.45}$$

where $g(S)$ is a damage function, and S is a damage parameter, which is function of the loading history. Equation 6.45 reduces to the damage theory based on MSP of Chapter 5 when the pore fraction $c = 0$.

Equation 6.45 has two microstructural parameters: the damage measure S, and the pore fraction c. As the response of crushed ice is result of changes in both parameters, kinetic equations are defined for these changes. The damage parameter

S can be defined by an equation similar to that in Chapter 5, as

$$S = \int_0^t f_3 \left(\frac{s}{\sigma_1}\right)^q d\tau \tag{6.46}$$

where q and σ_1 are positive constants. The parameter f_3 is function of all-around pressure σ_3 as

$$f_3 = f_1 (p_a / \sigma_3)^{r_1}, \tag{6.47}$$

where f_1 and r_1 are constants and p_a is the atmospheric pressure. Unlike polycrystalline ice, crushed ice lacks strength at $\sigma_3 = p_a$ unless it is sintered; Equation 6.47 represents the material behaviour for high confinements.

When shearing stress is also present, the compaction of a creeping solid can be described by Equation 6.38 by replacing strain with strain-rate. The volumetric creep relation is

$$\dot{\epsilon}_v = \frac{9nc\dot{\epsilon}_0}{2(n+1)(1+c)} \left(\frac{\bar{s}}{\sigma_0(1-c)}\right)^n \left(\frac{p}{\bar{s}}\right) g(S) \tag{6.48}$$

and can be used to obtain the new value of the pore fraction c from

$$\dot{c} = (1-c)\dot{\epsilon}_v. \tag{6.49}$$

It is noted that Equations 6.45 and 6.48 are derived for an incompressible matrix. Equations 6.46 and 6.49 are two desired kinetic equations for crushed ice.

6.6.1 Creep Compliance and Nonlinearity

The creep compliance $D(t)$ can be determined by constant-stress tests on ice. As this component does not contain the effect of the microstructures and their changes, the constants of the compliance can be obtained from the creep tests on polycrystalline ice as in Chapter 5. Crushed ice has much higher nonlinearity compared to polycrystalline ice. This is due to weak intragranular bonding. As the elasticity of crushed ice, as in polycrystalline ice, is linear, inclusion of an elastic term in the creep compliance,

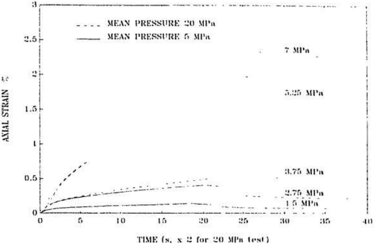

Figure 6.5: Strains from creep tests on crushed ice conducted at 5 and 20 MPa mean pressures. The applied stresses are shown on the curves.

which is to be used in Equation 6.44, will misrepresent the material behaviour. In this analysis only the delayed elastic and permanent creep terms are considered in the form

$$D(t) = D_1(t/t_0)^b + D_2(t/t_0), \tag{6.50}$$

where D_1, D_2, b and t_0 are positive constants.

The nonlinearity parameter n can be estimated by creep tests on crushed ice. Theoretically it should be possible to get this parameter from intact ice, but the strong nonlinearity that develops in crushed ice due to creep-dominant deformation is not reflected in intact ice. Under confining pressures, crushed ice undergoes a large degree of compaction (see test results in Chapter 4), thus the change of microstructure is also reflected in the creep tests. Here the nonlinearity and the compaction constants should be determined simultaneously. Using the creep data in Figure 6.5, n was 1.9 for 5 MPa mean pressure tests, and 2.1 for 20 MPa tests. A mean value 2 is used in

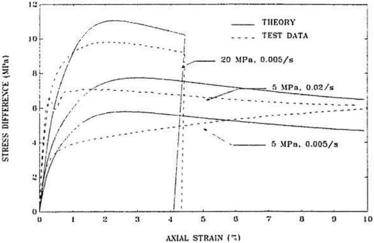

Figure 6.6: Stress-strain response of crushed ice obtained from MSP. The applied constant strain-rates and the confining pressures are shown on the curves.

the following analysis.

6.6.2 Prediction of Test Results

For the prediction of triaxial test results, the damage function and damage parameter S are assumed to be related exponentially as

$$g = e^{\lambda(S+S_0)} \tag{6.51}$$

where λ is a constant and S_0 is the initial damage. For a virgin material, the damage function g is unity. The predicted results for triaxial tests are shown in Figure 6.6. The value of the constants used in this analysis are presented in Table 6.1. The initial density of crushed ice at the time of the application of axial force is 0.8 kg/m^3 for 5 MPa tests and 0.85 kg/m^3 for 20 MPa tests. The model captures the principal features of the results, although some discrepancies exist, especially for tests conducted

Table 6.1: Model parameters required for the modified superposition method for crushed ice.

Delayed Elastic Constant	D_1	3×10^{-5}/MPa
Delayed Elastic Exponent	b	0.28
Secondary Creep Constant	D_2	1×10^{-6}/MPa
Nonlinearity Parameter	n	2
Reference Stress	σ_0	1 MPa
Reference Strain	ϵ_0	1
Reference Strain-Rate	$\dot{\epsilon}_0$	1×10^{-4}/s
Damage Constants	λ	1.2×10^{-5}
	f_1	100
	r_1	2
Initial Damage (5 MPa)	S_0	1.22×10^{5}
Initial Damage (10 MPa)	S_0	0
Damage Exponent	q	4.5

at low confining pressures.

6.7 Mechanical Model

In this section the mechanical model developed in Chapter 5 for the damaging material is extended for crushed ice. As discussed in Section 6.4, grain boundaries of crushed ice are treated as penny-shaped inclusions that are weaker in strength than the grain material, and have features of cracks. The effect of the porosity of crushed ice on the mechanical properties, as described in Section 6.2, is also added to the mechanical model.

Each strain component, the elastic, the delayed elastic, and the secondary creep is influenced by the pores and the grain-boundaries in crushed ice. As in polycrystalline ice, elastic strains are linear, while delayed elastic and creep strains are nonlinear. Because of the softness of the material, the permanent creep is dominant. The elastic and delayed elastic strains are of prime significance during rapid loadings.

6.7.1 Elastic Strain

The elastic properties of crushed-ice can be obtained from that of polycrystalline ice by damaging and introducing pores in it. The elastic moduli are given by Equations 6.9a and 6.9b. The damage state in the grain boundaries of crushed ice is similar to that of compression cracks in polycrystalline ice. In crushed ice the number of grain-boundaries increases due to further crushing of grains, while in polycrystalline ice the number of cracks increases due to damage. The difference lies in the rate of change in the microstructure. As the deformation in crushed ice is largely controlled by its creep behaviour, the rate of change of the grain size is smaller than the rate of change in number of cracks in virgin polycrystalline ice where initially the elastic and delayed elastic deformations are dominant. A macroscopic measure of damage seems appropriate for crushed ice. One such measure was described in Section 5.2. The bulk modulus of crushed ice is assumed to change with porosity only, and not due to damage. The Young's modulus E of crushed ice can be written in terms of the Young's modulus E_p of the porous matrix material, as

$$E = E_p/g(S), \tag{6.52}$$

where $g(S)$ is a damage function, and S is a damage parameter given by Equation 6.46.

The damage function and damage parameter S are assumed to be related exponentially as in Equation 6.51. The variation of the Young's modulus of crushed ice with respect to the damage parameter S is shown in Figure 6.7.

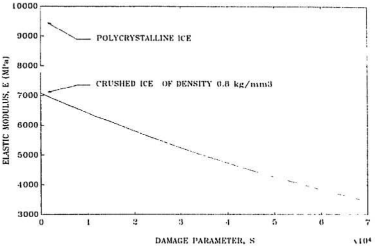

Figure 6.7: Variation of Young's modulus with the damage parameter S.

6.7.2 Delayed-Elastic Strain

The equivalent delayed elastic strain rate for the nonlinear Kelvin unit is given by

$$\dot{e}^d = \frac{s^d}{\mu_k(s^d)}\exp(\beta g), \tag{6.53}$$

where the viscosity η is function of the internal stress s^d that depends on the accumulated delayed-elastic strain, $e^d = \int_0^t \dot{e}^d dt$. In this equation the creep rate is enhanced by an exponential form of the product of a constant, β, and the damage parameter g. If the stiffness of the spring in the Kelvin unit is η_k, the internal stress can be obtained as

$$s^d = s - E_k e^d. \tag{6.54}$$

The stiffness, E_k, is related to the spring stiffness in the Kelvin unit in the virgin ice according to Equations 6.9b, 6.9a and 6.52.

The viscosity η_k is nonlinear function of the internal stress, and is obtained by equating Newtonian flow $\dot{e}^d = s/\eta_k$, and the power law flow, $\dot{e}^d = (s^d/\sigma_0)^n \dot{\epsilon}_0$. It is given as,

$$\eta_k(s^d) = \frac{\sigma_0^n}{s^{n-1}\dot{\epsilon}_0} \tag{6.55}$$

where σ_0 and $\dot{\epsilon}_0$ are reference stress and strain-rate respectively.

6.7.3 Secondary Creep

The weaker grain-boundaries in crushed ice enhance the secondary creep. A relation for a porous and viscous material following power-law nonlinearity can be obtained from a correspondence between the elastic solution of Equation 6.41 to a viscous solution by replacing strain with strain-rate, and can be presented as

$$\dot{\epsilon}_{ij} = \frac{3}{2}\dot{\epsilon}_0 \left(\frac{\bar{s}}{\sigma_0(1-c)}\right)^n \left[\frac{s_{ij}}{s^2}\bar{s} + \frac{cn}{(n+1)(1+c)}\left(\frac{p}{\bar{s}}\right)\left(\delta_{ij} - \frac{3\alpha}{s}s_{ij}\right)\right] g(S). \tag{6.56}$$

6.7.4 Dilatation

The results of triaxial tests on crushed ice as presented in Chapter 4 show that the volumetric response of crushed ice due to shear is always compaction. The major cause of this trend is presence of high porosity in crushed ice, which is undergoing volumetric creep due to hydrostatic and shear stresses. Other causes of volume change, e.g., cracking, which is the dominant mechanism of dilatation in polycrystalline ice, are negligible for this material.

In Section 6.5 it was shown that the compaction of crushed ice can be successfully described by a creeping material with pores. When shearing stress is also present, the compaction of a creeping solid can be described by Equation 6.48. The total volumetric strain is sum of the elastic strain obtained from the bulk modulus of Equation 6.9a and the contribution of the dilatation of the porous material following the power-law creep as given by Equation 6.48.

Table 6.2: Model parameters for crushed ice.

Young's Modulus of Ice	E^M	9500 MPa
Poisson's Ration	ν	0.3
Elastic Modulus in Kelvin Spring	E_k^M	7600 MPa
Damage Constant	λ	1.2×10^{-5}
Damage Exponent	q	5
Secondary Creep Reference Rate (20 MPa)	$\dot{\epsilon}_0$	$3.52 \times 10^{-7}/s$
Secondary Creep Reference Rate (5 MPa)	$\dot{\epsilon}_0$	$1.4 \times 10^{-6}/s$
Primary Creep Reference Rate	$\dot{\epsilon}_{k0}$	$10 \times \dot{\epsilon}_0/s$
Creep Exponent	n	3

6.7.5 Prediction of Test Results

In Figure 6.8 the simulated responses of crushed ice in simple shear stress path are shown. The predicted results for the triaxial strength-tests are shown in Figures 6.9 and 6.10. The value of the constants used in this analysis are presented in Table 6.2. Comparison with test data shows that the mechanical model can predict the material response, the shear and the volumetric, very well. For tests at high strain rate, dilatation due to opening of cracks reduces the effect of compaction, and an improvement in prediction can be made by including this effect. If long-term response is of main concern, better performance from this model can be obtained by sacrificing elasticity of the material.

6.8 Summary

Crushed ice can be described as a porous material with weak intragranular bonds. The response of crushed ice can be described by introducing porosity in the polycrystalline ice. To describe the behaviour of crushed ice, two models based on continuum mechanics were presented. The first model was based on the modified superposition principles, while the second model is mechanical. In both models, the porous mi-

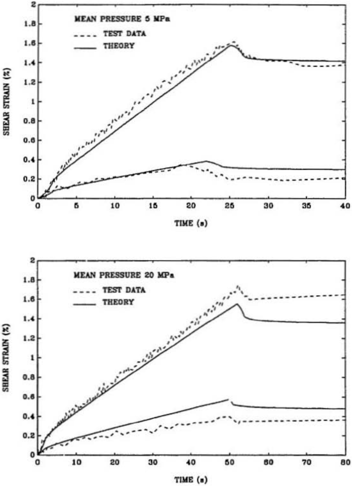

Figure 6.8: Creep and relaxation response of crushed ice as obtained from the mechanical model.

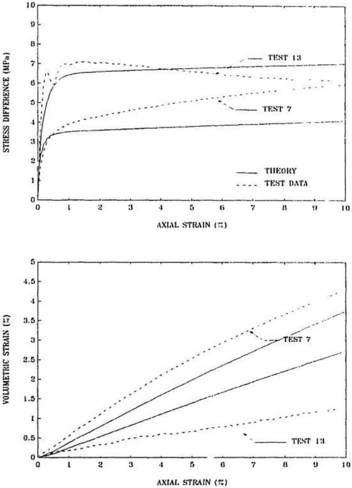

Figure 6.9: Stress-strain response of crushed ice obtained from the mechanical model subjected to constant strain-rate of 0.005/s (TEST 7) and 0.02/s (TEST 13) with the confining pressure of 5 MPa.

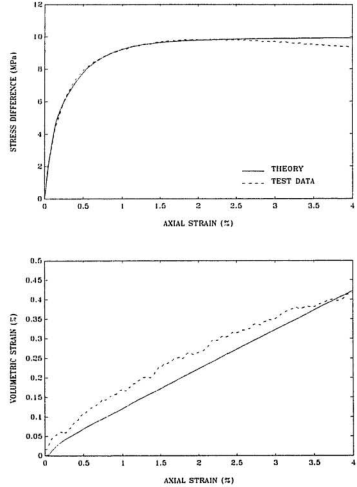

Figure 6.10: Stress-strain response of crushed ice obtained from the mechanical model subjected to constant strain-rate of 0.005/s and the confining pressure of 20 MPa

and its variation was included. Another microstructural variable, the grain boundary sliding effect, was also included by considering these as weak structures in the material. The performance of both models is good.

Chapter 7

Application to Extrusion Analysis

7.1 Introduction

During the process of ice-structure interaction ice particles are broken into discrete pieces due to crushing. These crushed particles form a distinct interfacial layer between the intact ice mass and the structure (Frederking et al., 1990). The thickness of this layer may vary spatially depending on the structure stiffness, ice inhomogeneity and the velocity of the interaction. The crushed material from the interface is extruded as ice moves towards the structure. The process of crushing and extrusion is cyclic and load on the structure is characterized by the deformation and flow of the crushed material.

In this Chapter, the flow properties of crushed ice under plane-strain extrusion conditions are examined. These tests were conducted with industry collaboration. The details of the test setup and some results are presented in Spencer et al. (1992) and Singh et al. (1993). For completeness, a brief description of test-setup is presented here. This is followed by discussion of test results and evaluation of various constitutive theories applicable to crushed ice extrusion problem. Finally, connections

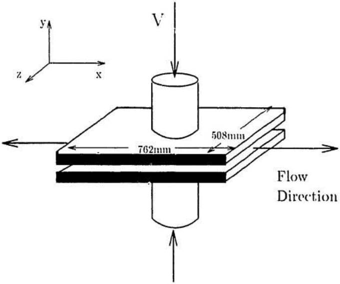

Figure 7.1: Geometry of extrusion tests. Flow in z-direction was prevented to obtain plane strain condition.

are made to the theories described in previous Chapters, and finite element analyses are conducted to compare the test results and the theoretical developments. A closed-form solution is also presented for the plane strain extrusion of viscous material following power-law nonlinearity.

7.2 Setup of Extrusion Tests

A schematic diagram of the test geometry is shown in Figure 7.1. The material was loaded at constant velocity in the y-direction. The flow of crushed ice was in the x-direction. The channel shape of the bottom platen prevented flow in the z-direction. The top platen was instrumented with eight pressure cells to measure the pressure distribution. Two potentiometers were mounted across upper and lower platen for displacement measurements.

A closed loop servo-controlled system was used, where averaged displacement across the platen was the feedback signal. Mean pressure was also measured at the actuator. The system as used here could apply load close to 4 MN, with servo-control feedback. Although the apparatus functioned extremely well, the high loads and loading rates, and the vibrations experienced during the tests constituted demanding conditions. For example, it was not possible to maintain perfectly the nominal loading rate during the vibrations. The crushed ice layer of 100 mm thickness and density of 0.55 g/cm^3 was squeezed between rigid parallel plates at various speeds ranging from 2.5 mm/s to 160 mm/s at -10°C.

7.3 Test Results and Discussion

During the initial stages of the extrusion, the mean platen pressure increased monotonically. At high pressures a sawtooth pattern developed in some tests. The extrusion of the crushed ice was nearly continuous for the slower tests (2.5 mm/s), while with the increase in the speed the dynamic activities became dominant. Again at the highest speed (160mm/s) extrusion was smooth. This transition from the dynamic process to a nearly static process at high speeds is typical in ice-structure interaction (Singh et al., 1990). Mean pressure and the displacement time-series for typical extrusion tests are presented in Figure 7.2. The dominant frequency of pressure variation changed with speed. As the layer thickness reduces during the test, a larger pressure is needed for the extrusion and the dominant frequency decreases. Sudden changes of pressures during extrusion cycles and a large pressure gradient along the extrusion plane resulted in vibrations in the platen for some tests. Post test inspection revealed a solid mass of fused ice in the central zone.

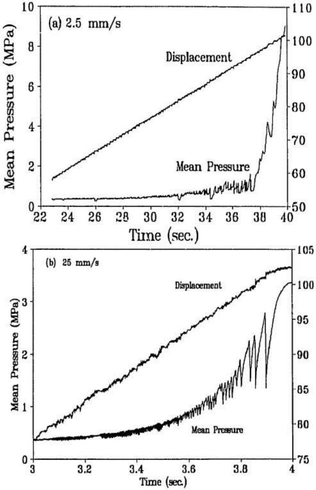

Figure 7.2: Mean pressure and the platen displacement for typical extrusion tests at speeds (a) 2.5 mm/s, (b) 25 mm/s, (c) 60 mm/s and (d) 160 mm/s.

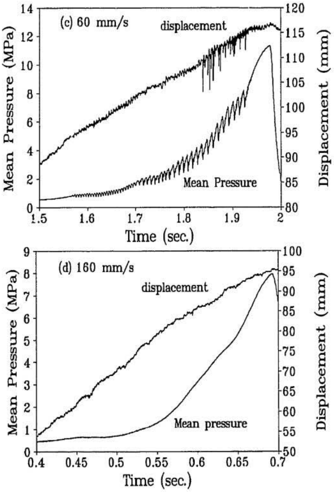

Figure 7.2: continued.

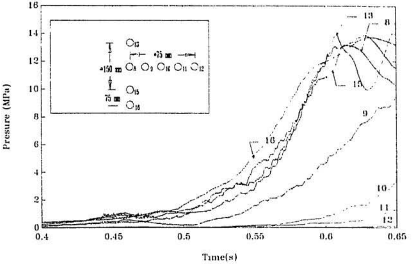

Figure 7.3: Pressure variation as recorded from various sensors with time for a typical test at 160 mm/s. The sensor locations are shown in inset.

7.3.1 Pressure Distributions

The pressure experienced by different transducers varied greatly depending upon their location in the extrusion channel. A typical pressure record from all pressure cells is shown in Figure 7.3. The pressure distributions along the z-axis (sensors 8, 13, 15 and 16) are nearly uniform and verify that a plane strain condition existed during extrusion. On the other hand, the pressure along the x-axis, the extrusion axis (sensors 8, 9, 10, 11 and 12), varied greatly. The largest pressure along the extrusion axis was recorded at the centre of the platen, while near the exit, pressure was negligible.

During the initial stage of the extrusion, pressure along the extrusion axis varied exponentially with the peak at the center. As higher pressure developed, the pressure distribution flattened out to a bell shape. In Figure 7.4, the change of the pressure distribution along the extrusion axis is presented for two tests. During the initial stage of extrusion, i.e., at the low-pressure stage, the load was generally carried by a narrow central zone of the platen. As the pressures began to rise, the pressure distribution usually flattened out to a parabolic shape, and the load carrying zone generally widened. Similar changes in the pressure distribution were observed during individual dynamic events. For a typical event in test X991 this change is presented in Figure 7.4b. The high-pressure fused zone carrying most of the load is denoted the "critical zone."

In the present tests, rapid decrease in mean pressure was associated with failure in ice. This failure was not simultaneous throughout the channel, but started just outside the critical zone. It is noted that in the failure zone, the pressure gradient is highest. As shear stress is proportional to the pressure gradient, high shear stresses occur in the failure zone. In Figure 7.5 the pressure variation during a typical dynamic cycle is presented. At points 1, the pressure distribution is convex in the critical zone and increases both in magnitude and area when the mean pressure increases. A drop in pressure outside the critical zone, i.e., about 150 mm from the centre, can be observed at point 2. The failure has been initiated at this moment, and moves towards the centre. At point 3, pressure in the critical zone, and at a distance of about 75 mm from centre, drops as failure progresses. This also causes a sudden pressure increase at the centre, and momentarily the pressure distribution becomes concave. The high-pressure gradient near the centre forces the ice in this area outwards towards the low pressure zones, and the pressure distribution again becomes convex in the critical zone as at point 4. This process is repeated for the next cycle.

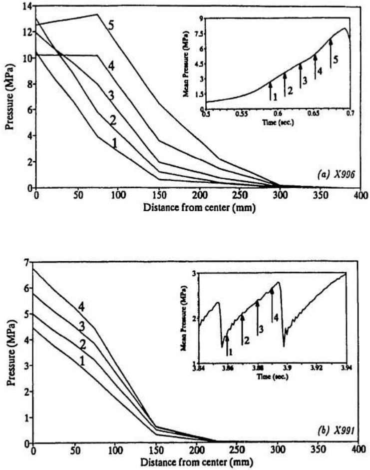

Figure 7.4: Pressure distribution transforming from friction-hill at the beginning of extrusion to a flatter parabolic shape at high pressure stage of extrusion for (a) 160 mm/s and (b) 25 mm/s speed test.

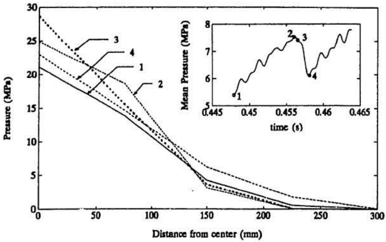

Figure 7.5: Variation in pressure distribution during a typical dynamic cycle of mean pressure for a test at 125 mm/s.

7.3.2 Effect of Speed on the Flow

The mean platen pressure changes with the crushed layer thickness as shown in Figure 7.6 for different speeds. For clarity, the dynamic activities are not shown in the figure. The results from a compaction test at speed of 2.5 mm/s, in which the ice was prevented from extruding, is also superimposed on the figure. As the platen speed increased, a lower final thickness was achieved for same mean pressure. From Figure 7.6 it can be seen that large deformations in crushed ice are associated with compaction, even in the absence of extrusion. For a given layer thickness, a much larger load was found in the slower tests. The formation of fused material in the critical zone is associated with the compaction process. For slower tests, the critical zone forms at an earlier stage in the test. For faster tests, rapid extrusion of material caused less compaction at earlier stages of the tests. The results illustrated in Figure 7.6 make

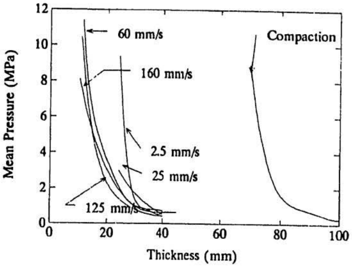

Figure 7.6: Change in the mean pressure with the crushed layer thickness for different speed tests.

an analysis of the effect of rate of loading difficult.

7.4 Analysis and Interpretation

As the flow behaviour of granular geomaterials is well represented by the Mohr-Coulomb failure criterion, it has been proposed for crushed ice (Hallam and Pickering, 1988; Sayed and Frederking, 1992). On the other hand, as solid ice exhibits viscoelastic behaviour, models for flow of crushed ice based on viscous flow have also been proposed (Kurdyumov and Kheisin, 1976, for extrusion during drop ball tests, and Jordaan and Timco, 1988, and Jordaan et al., 1991, for upswing during saw-tooth dynamics). The viscous flow theory exhibits a dependence of force on velocity, whereas the Mohr-Coulomb flow theory does not. In this section, these theories are evaluated for crushed ice. Physical changes in the material are also examined.

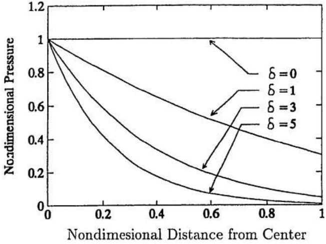

Figure 7.7: Pressure distribution predicted by the Mohr-Coulomb flow theory. The value δ is the wall friction.

For plane-strain extrusion, the material models based on Mohr-Coulomb flow and viscous flow behaviour predict different pressure distribution along the extrusion channel. The Mohr-Coulomb flow model predicts an exponentially increasing pressure distribution moving from the exit to a sharp peak at the platen center (Figure 7.7), while the viscous flow model predicts a convex pressure distribution (Figure 7.8).

7.4.1 Physical Changes in Crushed Ice and Formation of Critical Zone

The deformation of crushed ice at early stages of loading is dominated by granular flow and compaction. During the high-pressure stage of extrusion, a cycle of solidification and breaking occurs. In the critical zone within the crushed layer, groups of particles stick together under higher pressures, forming a fused mass of crushed ice. During

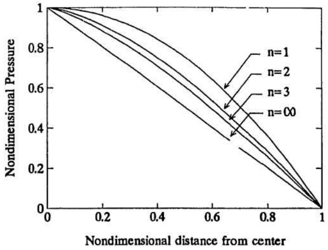

Figure 7.8: Pressure distribution predicted by the viscous flow theory. The value 'n' is the power-law nonlinearity coefficient.

this period, the pressure rises rapidly, and slow solid extrusion from the central region occu The process of sintering is closely related to pressure melting. During loading the local pressure at the particle contacts may be large enough to cause melting. Other important mechanisms for sintering at high temperature are due to diffusion. These could be dominant for slow extrusion processes. It is suggested here that the material behaviour could well be viscous on the 'upswings' of the dynamic process. Clearly the failure process leading to drops in load is not likely to result from viscous flow alone, although it may be aided by factors such as pressure melting.

As noted, after the tests, a solid mass of fused ice in the center of the platens was observed. This was also observed by Sayed and Frederking (1992). The density of this solid mass approached that of the polycrystalline ice, while outside this fused zone the density remained close to the initial value (Figure 7.9). With loading this fused zone expands from the centre of the platen. The boundary between the fused

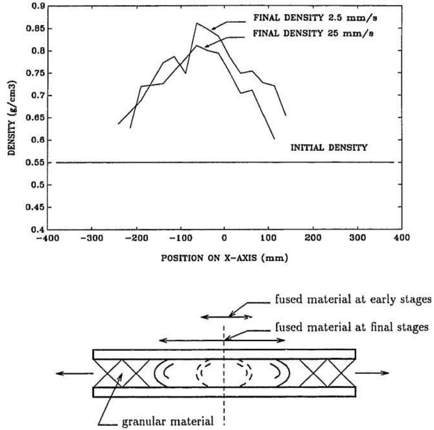

Figure 7.9: Variation of density along the extrusion axis.

zone and granular zone was distinct. The measured density after a particular test is shown in Figure 7.9, which also illustrates growth of the fused zone. Outside this zone, crushed ice is still granular.

The appearance of the fused ice was similar to that found in the layer adjacent to the indentor in field tests. Here, the ice undergoes a breakdown in structure to a fine-grained material characteristic of the layer. Thus, besides cracking, the crystal structure was degraded. There are therefore two kinds of damage: cracking and breakdown of structure. Both lead to increased compliance, and in particular, a substantial increase in the viscous response. The presence of high shearing stresses enhances the damage process. Such a stress state would exist near the edges of the critical zone, leading to breakdown into the fine particles.

7.4.2 Crushed Ice as a Mohr-Coulomb Material

In Figure 7.7, the pressure distribution based on a Mohr-Coulomb (M-C) flow theory (Savage et al., 1992, without the effect of gravity) was presented. For the velocity range of these tests, the effect of gravity is neglected. Comparing the pressure distributions shown in Figures 7.4 and 7.7 suggest that M-C model can predict the pressure near the exit for all cases. This model can also gives good estimates of the pressure at the central zone only during the early stages of the tests. This can be seen in Figure 7.10, where the predicted pressures from this model are presented for the early stages of extrusion. The value of the material cohesion is 1 kPa with a friction angle of 25 degrees, whereas a friction angle of 7 degrees between the ice and platen was used for M-C theory. Attempts to fit the M-C flow model with constant properties at advanced stages of extrusion were fruitless, as the pressure distribution was no longer concave near the centre.

Sayed and Frederking (1992) conducted similar plane-strain extrusion tests for

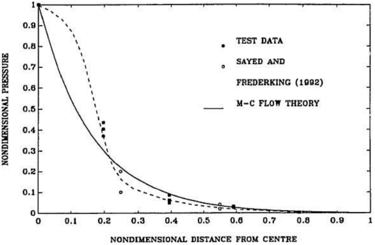

Figure 7.10: Comparison of measured pressure distributions of a test at early stages of extrusion to the Mohr-Coulomb flow theory. Test results form Sayed and Frederking (1992) are also presented.

crushed ice. In Figure 7.10, the pressure distribution from their test (test 12) is also shown in non-dimensional form, with one of the present test, and the M-C solution. The broken line shows an alternative interpretation of the pressure distribution corresponding to the early growth of a critical zone. It should be noted that in Sayed and Frederking's test-setup, the next sensor is at a distance of one fourth of half platen length from the central sensor; while in the present test-setup it is one fifth. It may be possible that the convex part of the pressure distribution in not always observed.

The response of crushed ice in the plane-strain condition is complex because of sintering of ice, the extent of damage in the material, and the dynamic characteristics, all of which change during a test. This complexity is enhanced by differential compaction in the material. In the triaxial tests on crushed ice as presented in Chapters 3 and 4, the confining pressures in triaxial tests were varied from 5 MPa to 20 MPa

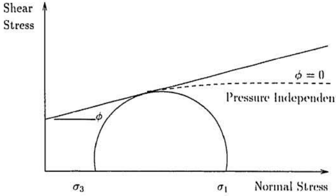

Figure 7.11: Frictional behaviour of crushed ice.

in various tests. This is in the range of the observed pressures near centre of the platen in the extrusion tests. For triaxial tests below 10 MPa confining pressure, the friction angle based on peak stresses was about 14 degrees (Figure 4.12), whereas for tests higher than 10 MPa, a friction angle close to zero degrees was observed. This shows that the material behavior has changed from Mohr-Coulomb flow, which is pressure-dependent, to a pressure-independent material, where friction does not play any role at macro-structural level. This change of material behaviour is illustrated in Figure 7.11. This change of behaviour is also possible with regard to friction between crushed ice and the steel platen. A small change in the value of friction, as also noted by Savage et al. (1992), will result in an order-of-magnitude difference in pressure prediction. Thus, any attempt to model crushed ice flow under high pressures must include the change in friction during the process.

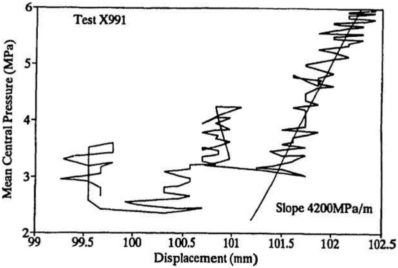

Figure 7.12: Mean central pressure variation with the displacement of the platen for a 25mm/s test.

7.4.3 Crushed Ice as a Viscous Material

For crushing events, the mean stiffness per unit area of ice increases with compaction. This stiffness is mainly due to the consolidated zone at the centre of the platen. The mean central pressure (averaged in central 300 mm of the platen) for a typical test at 25 mm/s is presented for corresponding platen displacement in Figure 7.12. The stiffness for the marked event is 4200 MPa/m. Other tests showing dynamics also provide similar results with some dependence on speed. Slopes of the mean pressure-time trace from individual dynamic activities are shown in Figure 7.13 for various tests. This slope increases with speed until the speed of 60 mm/s. The decrease of slope at high speed may be due to change of the driving mechanics of flow from quasi-static to inertia.

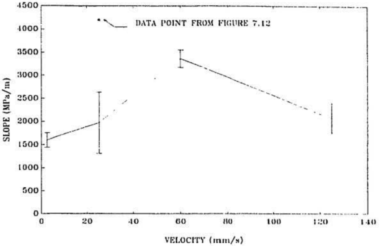

Figure 7.13: Variation of the rate of the mean pressure change for individual dynamic events with the velocity of loading. The vertical bar is one standard deviation.

To investigate the elastic behaviour of crushed ice, appropriate boundary value problems were solved using the finite element method. Only the central consolidated zone (see Figure 7.9) of 300 mm length was considered. The finite element mesh used in this analysis is shown in Figure 7.14. The contact between the material and the top platen is rigid, while symmetric boundary conditions were used along xz and yz-planes. The measured pressure distribution at the top surface and a lateral pressure as measured at 150 mm from the center was applied. These values of pressures and the averaged displacement of top surface nodes are compared to measured values presented in Figure 7.12. The best fit was obtained when the modulus of elasticity of crushed ice is 45 MPa. This value is more than two orders less than the modulus of the polycrystalline ice (about 8 GPa), suggesting that deformation mechanisms other than elastic are dominant.

Jordaan and Timco (1988) presented a closed-form solution of Newtonian viscous

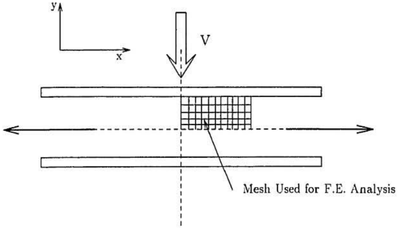

Figure 7.14: F.E. mesh used in the analysis.

flow for the plane-strain extrusion. Extending their work, we present here a solution for nonlinear flow. The geometry of flow is shown in Figure 7.15. The material was assumed to be incompressible and isotropic. The problem is further simplified by using the lubrication theory. In this, it is assumed that the crushed layer is thin ($h \ll L$), and the flow in x-direction greatly exceeds that in y-direction. This simplification results in uniform pressure distribution in y-direction.

The constitutive behaviour of crushed ice is assumed to obey power law as

$$\frac{\partial u_x}{\partial y} = \dot{\epsilon}_0 \tau^n, \tag{7.1}$$

where u_x is velocity of flow in x-direction, and τ is shear stress as shown in Figure 7.15. Let the inertia forces be negligible, the equilibrium equation can be written as

$$\frac{\partial p}{\partial x} + \frac{\partial \tau}{\partial y} = 0, \tag{7.2}$$

where pressure p is only function of x-direction. As the flow is symmetrical about $y = h$ plane, we will concentrate on the domain $x = 0$ to L and $y = h$ to $2h$.

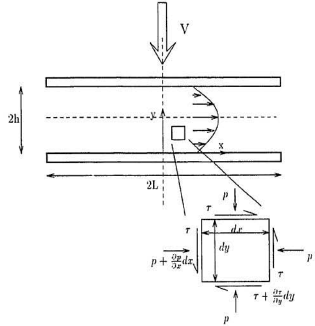

Figure 7.15: Geometry of flow. The pressure distribution along y-direction is assumed to be uniform.

Integrating Equation 7.2 in y-direction from h to y, and substituting for τ from Equation 7.1 the result is

$$\frac{\partial u_x}{\partial y} = \dot{\epsilon}_0 \left(\frac{\partial p}{\partial x}\right)^n (y-h)^n, \tag{7.3}$$

where the boundary condition $\tau = 0$ at $y = h$ was used. On further integration, between y and $2h$, with the boundary condition $u_x = 0$ at $y = 2h$, u_x is obtained as

$$u_x = \frac{\dot{\epsilon}_0}{n+1} \left(\frac{\partial p}{\partial x}\right)^n [(y-h)^{n+1} - (h)^{n+1}]. \tag{7.4}$$

From the continuity of flow, a relation between u_x and u_y, velocity of the platten motion can be written as

$$x u_y = -\int_h^{2h} u_x dy. \tag{7.5}$$

Substituting for u_x from Equation 7.4, and manipulating terms, an equation for the variation of the pressure p is

$$\frac{\partial p}{\partial x} = A x^{1/n}, \tag{7.6}$$

where

$$A = \left[\frac{u_y(n+2)}{h^{n+2}\dot{\epsilon}_0}\right]^{1/n}. \tag{7.7}$$

At the exit $x = L$, stress is p_0, thus by integrating Equation 7.6 between x and L and expression for the pressure distribution along the x-direction can be obtained as

$$p = \frac{An}{n+1}[L^{(n+1)/n} - x^{(n+1)/n}] + p_0. \tag{7.8}$$

The sign of p follows that of the platten velocity, i.e., when platens are converging, pressure throughout the extrusion channel is positive. This solution is presented in Figure 7.8 for various value of n. For $n = 1$, Equation 7.8 reduces to Jordaan and Timco's solution. In Figure 7.8, pressure distribution for $n = \infty$ is also presented. If the value of n is large, Equation 7.8 reduces to

$$p = A(L - x) + p_0. \tag{7.9}$$

It should be noted that when $n = \infty$, the material is plastic, and the pressure distribution is linear.

Mean pressure, p_m, on the platen can be obtained by integrating Equation 7.8 between $x = 0$ to $x = L$ as

$$p_m = \frac{An}{2n+1} L^{(n+1)/n} + p_0, \tag{7.10}$$

where p_0 is pressure at exit. In Equation 7.10, the effect of crushed-layer thickness is in parameter A, as shown in Equation 7.7. If the pressure at the exit is neglected, the mean pressure, p_m is

$$p_m \propto \left(\frac{1}{h}\right)^{(n+2)/n} \tag{7.11}$$

From the logarithmic plot of mean platen pressure and the inverse of the crushed layer thickness for the data presented in Figure 7.6, the slope was calculated for various tests. This slope varied greatly for pressures less than about 2 MPa, but at higher pressure it is nearly constant. For 2.5 mm/s speed test it was 8, and for 60, 125 and 160 mm/s speed tests it was 2.2. For a Newtonian fluid this slope would be 3, and for power-law nonlinear material with $n = 3$, the value would be 1.67. This suggests possible applicability of viscous flow model for higher speed tests. In slower tests, the effect of compaction has made interpretation difficult.

7.4.4 Crushed Ice as a Viscoelastic Material

In Figure 7.16, the pressure distributions at advanced stages of a test as presented in Figure 7.4 is compared with the pressure distribution predicted by the linear viscous theory (Jordaan and Timco, 1988) and the nonlinear viscous theory for $n = 3$ in Equation 7.8. These theories provide a good fit to the data for the central portion, i.e., for the fused zone.

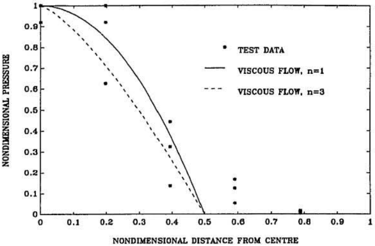

Figure 7.16: Comparison of pressure distributions of a typical test at advanced stages of extrusion to that predicted by linear and nonlinear viscous theories.

The viscous and viscoelastic theories predict a convex pressure distribution. Thus, it cannot represent the observed pressure distribution near the edges. As most of the force is concentrated in the critical zone, the viscous theory models the material well during high-pressure interactions. At the edges, the material in its loose state has yet to undergo the solidification process, which is not included in these theories. For a general solution of the extrusion problem, both Mohr-Coulomb and viscous flow theories should be combined to obtain the measured pressure distribution. It is also desirable that the effect of volumetric deformation, which is caused by pore collapse, should be included in this formulation.

Using the constitutive theory based on the mechanical model of crushed ice as presented in Chapter 6, a F.E. analysis was performed for the flow of crushed ice under plane-strain conditions. The material is assumed as a compressible creeping solid following a power-law relation between stress and strain rate. The density of crushed ice is $(1 - c)$ times the density of polycrystalline ice. Only the fused zone as shown in Figure 7.9 is analyzed, and outside this zone pressure is neglected. This assumption is consistent with the observed pressure distributions discussed earlier in this chapter. A 150 mm long and 20 mm thick slab of crushed ice with pore fraction of 0.2 is squeezed under plane strain conditions to a final thickness of 10 mm. The final state of deformation is similar to extrusion tests.

Unlike a fixed boundary at the indentor interface as in viscous flow theory of the last section, a frictional boundary condition is used. This provides a coupled response between viscoelastic ice and the frictional interface. Xiao et al. (1992) have shown the importance of this wall friction, the changes of which can result in dynamic forces on the structure. The wall friction varies with the speed (Barnes et al., 1971) of extrusion and the magnitude of stresses near the interface. In the present analysis, as the emphasis is laid on the compaction and flow of crushed ice, the coefficient of friction between ice and steel is assumed to be constant with the magnitude of 0.1.

The result of this analysis is presented in Figures 7.17 and 7.18 by contours plots of stresses along the compression axis and the pore fractions of crushed ice. From these figures the effect of the extrusion speed on the material behaviour can be observed. In the slower test, the material has elongated more than the faster test, the stresses and the pore fractions are low, and the deformation is dominant by the flow. The stresses and pore fractions at the top platen—in the extrusion tests pressure was measured at the top platen—are presented in Figure 7.19 for both tests along with the test data. It can be observed that the stress, or the pressure as it was termed frequently in this chapter, distribution is bell shaped. This distribution is nearly parabolic for the faster test and spread in wider area. This shows that the material does not have to be frictional to yield a bell-shaped distribution, the frictional interface can cause such distribution of stresses for low-speed extrusion tests.

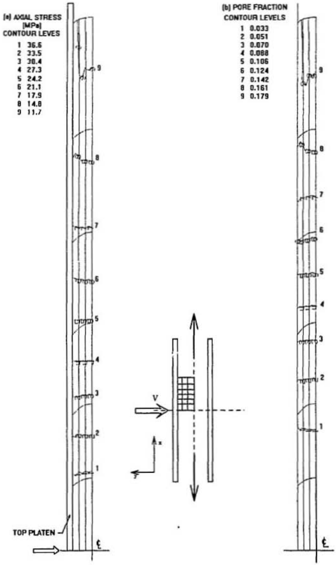

Figure 7.17: Contour plots of stresses in the direction of compression and pore fractions for a test speed of 2.5 mm/s. The contours are leveled from 1 to 9, and are presented on the deformed mesh.

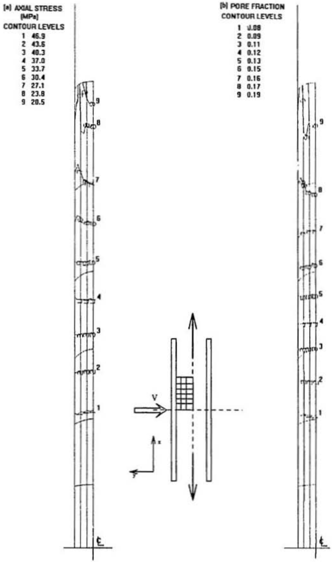

Figure 7.18: Contour plots of stresses in the direction of compression and pore fractions for a test speed of 25 mm/s. The contours are leveled from 1 to 9, and are presented on the deformed mesh.

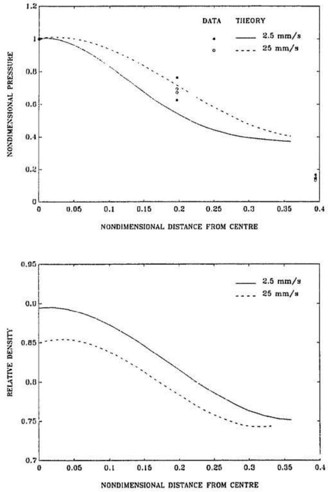

Figure 7.19: Variation of axial stresses (top) and density (bottom) in the critical zone at the top platen as obtained from Figures 7.17 and 7.18.

During the extrusion process, the pore fraction of crushed ice changes. At the exit the pore fraction is at its initial value, while towards the centre the pore fraction is reduced largely (Figures 7.17b and 7.18b). The variation of density at the top platen deduced from the pore fraction is presented in Figure 7.19. This variation in density is consistent with the observed variation of density as shown in Figure 7.9. The variation of density is also dependent on the speed. In the slower test, as more time is available for compaction that is time-dependent, the density near the centre is larger than that in the faster test.

7.5 Summary

The extrusion of crushed ice between parallel plates covers a wide range of the material behaviour. At low stresses, behaviour based on the Mohr-Coulomb model is appropriate to describe the state of the stresses in the material. On the other hand, phase change at the grain boundary at high pressures alters the material behaviour, increases ductility, and a viscous formulation is consequently suggested. A nonlinear viscous flow theory for plane strain condition is presented for such cases.

The viscous formulation at high stresses is supported by the change in the pressure distribution from the hill-type pressure distribution at the centre of the platen to a convex pressure distribution. As most of the forces are distributed in the convex manner at the central zone, viscoelastic theories model the material well during high pressure interactions. The critical zone, which is the zone of fused ice mass with density as high as that of polycrystalline ice, increased from the centre of the platen towards the exit in a progressive manner. The stiffness of the fused ice was computed, and was more than an order of magnitude smaller than that of polycrystalline ice. This shows that deformation in the critical zone is dominated by inelastic behaviour.

Using a F.E. analysis of the fused zone by assuming crushed ice as porous and viscous material a bell-shaped pressure distribution was observed. This suggests that material do not have to frictional for such distribution.

After the initial compaction of the material, a dynamic force pattern in time similar to those in medium-scale tests was observed. This shows that spalling and cracking are not necessary to produce the dynamic effect in the ice-structure interaction, and the key to this process remains in the crushed material and its boundary with the structure.

Chapter 8

Conclusions and Recommendations

The development of a constitutive theory for a nonlinear material involves understanding and modelling of various physical processes contributing to the observed material response. At some stage, empirical relations obtained from the material response may be required to determine material coefficients. For simplicity one may resort to simple phenomenological models based on curve fitting techniques, but these methods are often restricted to a narrow range of loading conditions, and fail to extrapolate to states for which test data may not be available.

The process of material modelling can be streamlined by following the framework of thermodynamics. The internal variables are essential in that they enable the microstructural properties to be included into a continuum theory. This thesis is an investigation in this direction. Although a major part of this thesis is devoted to the modelling of physical changes in ice during ice-structure interaction, yet the presented theory is applicable to broad range of materials where the microstructural features such as microcracks and cavities influence the material behaviour.

The strength and deformation behaviour of ice depends on the rate of loading, the density of microcracks, the toughness of grain-boundaries and other microstructures. After extensive microcracking when the cracks coalesce, pores are formed at triple junctions of weakly connected grains. This material is finally extruded from the structure interface as finely crushed ice. The confinement that is due to the geometry of ice and structure has great influence on the rate of change of these microstructures.

Triaxial tests were carried out on polycrystalline ice and crushed ice. These two materials represent two states in the ice failure and extrusion process. The tests were designed to reflect the conditions during high rate and pressure interaction between ice and a structure. The changes in the microstructure were closely examined by thin sections of samples before and after the tests. To describe various changes in the material two theories were formulated, and verified for both materials. A measure of damage and porosity was taken as internal variable. The damage measure includes microcracking and non-continuous grain-boundary sliding. Flow properties of crushed ice were also modelled by a closed-formed solution and a finite element method.

8.1 Conclusions

8.1.1 Triaxial Tests

Polycrystalline Ice

Under uniaxial stresses, ice is very brittle. The high rate of damage in constant strain-rate tests results in lower strength of ice. Cracks are open and aligned to the maximum principle stress-direction by extending several grains. The cracked material is highly anisotropic at large strains. The failure is usually by axial splitting in the sample due to extension of one or many critical cracks.

When confining pressure is also applied, cracks are arrested at natural boundaries such as triple junctions. This resulted in increase in strength. Cracks are distributed uniformly, and the material behaviour is nearly isotropic. The average length of cracks is of the order of the grain size. Further damage is more stable than in the uniaxial case. For confining pressure more than 10 MPa, the strength is independent of confining pressure. The dilatation under larger confinements is suppressed.

Thin sections of the damaged ice resemble those of crushed ice samples. Big grains are surrounded by finely-crushed grains that were recrystallized by pressure-sintering. Cracks are formed at critical inhomogeneities such as grain-boundaries.

Crushed Ice

High porosity of crushed ice makes it very sensitive to hydrostatic compression. This compaction is time-dependent, and is enhanced several fold when shear stresses are applied. Especially designed end-platens were successfully used with crushed ice to maintain homogeneous deformation in the sample during large strains. In the slower tests, material undergoes large compaction during axial loading, while in the faster test, the effect of compaction is reduced by dilatation caused by brittleness in the material. The rate effect is clearly visible for low strains. The strength is strongly pressure-dependent for pressures lower than 10 MPa. This is consistent with other frictional materials. For higher pressures, the strength is pressure-independent as in metals. In the test range (strain rate between $5 \times 10^{-5}/s$ to $2 \times 10^{-2}/s$), the strength is independent of rate of deformation of the sample.

Thin-section studies of samples after tests show that due to extensive crushing, the average grain size has reduced greatly from the original size. The larger grains are protected by fine grains that were created by crushing of critical grains. The pores are entrapped at the triple points of some larger grains and at their grain-boundaries.

8.1.2 Material Modelling

Constitutive equations to describe the damage in viscoelastic materials were presented by two theories. The first theory is a solution for nonlinear elastic media, which was extended to nonlinear viscoelastic media using the correspondence principles and a modified superposition integral. The second viscoelastic theory is based on mechanical model with nonlinear elements. Three components of deformation, i.e., the elastic, the delayed elastic, and the viscous creep, are separately identified and their changes with the amount of microcracking and porosity are modelled. The elastic properties of the damaged material were estimated by a self-consistent solution.

Polycrystalline Ice

The kinetic equation for microcracking and other changes in the microstructure in polycrystalline ice is described by a generalized J-integral. Both theories used in modelling compared well with the measured response of polycrystalline ice. The first theory is more systematic and requires fewer parameters. The main disadvantage of this theory is the universality of the nonlinearity. The mechanical model does not has such limitation and gives a physical description of various components of deformation.

Crushed Ice

Crushed ice can be described as a porous material with weak intergranular bonds. In both theories, the effect of porosity is included. Another microstructural variable, the grain boundary sliding effect, was also included by considering them as weak structures in the material. The performance of both models is acceptable, though only the mechanical model can address the nonlinearity, linear elastic properties, and the volume change during the deformation.

Extrusion Analysis

The extrusion of crushed ice between parallel plates covers a wide range of the material behaviour. At low stresses, behaviour based on the Mohr-Coulomb model is appropriate to describe the state of the stresses in the material. On the other hand, phase change at the grain boundary at high pressures alters the material behaviour, increases ductility, and a viscoelastic formulation is consequently suggested.

The viscous formulation at high stresses is supported by the change in the pressure distribution from the hill-type pressure distribution at the centre of the platen to a convex pressure distribution. As most of the forces are distributed in the convex manner at the central zone, viscoelastic theories model the material well during high pressure interactions. The critical zone, which is the zone of fused ice mass with density as high as that of polycrystalline ice, increased from the centre of the platen towards the exit progressively.

After the initial compaction of the material, a dynamic force pattern in time similar to those in medium-scale tests was observed. This shows that spalling and cracking are not necessary to produce the dynamic effect in the ice-structure interaction, and the key to this process remains in the crushed material and its boundary with the structure.

8.2 Recommendations for Further Research

Development of a constitutive theory for a nonlinear material with changing microstructure is a major task. This thesis has described many important features of such a material with special attention given to the ice-structure interaction problem. Based on the experience gained in this study, recommendations for future study can be made in the following areas:

1. Uniaxial tests are common means to obtain the response of many polycrystalline and composite materials. In uniaxial tests, microstructural inhomogeneities develop at very low strains, and can complicate the modelling process. Further in real problems, uniaxial stress states are seldom encountered, and deformation is large and cracking is stable. In these cases, triaxial tests are suggested. For correct modelling of the material behaviour either in creep tests, or, in strength tests, volumetric strains must be measured.

2. During triaxial testing of ice, the cracking activities are suppressed, but other microstructural changes that are stable such as change in grain size due to dynamic recrystallization occur. These physical processes are poorly understood for high pressure and strain-rate tests. Triaxial tests should be designed and conducted to monitor these changes.

3. The amount of dilatation directly affects damage behaviour and its progress. Further improvements can be made in the dilatation relation for the cracking processes, where the work potential does not exist, and formulation of coupled kinetic equations for damage and dilatation, similar to that presented for crushed ice. In crushed ice, improvements in kinetic equations can be made by including compressibility of ice grains.

4. Interaction of grain boundaries and pores in crushed ice should be studied. The assumption of dilute and non-interaction for these microstructures is questionable for crushed ice just outside the critical zone, where the density of crushed ice is low, or the pore concentration is large due to continuous failure.

References

Abele, G. and Gow, A.J. (1975), "Compressibility Characteristics of Undisturbed Snow," U.S. Army Cold Region Research Laboratory, CRREL Research Report 336, 56p.

Ashby, M.F. and Hallam, S.D. (1986), "The Failure of Brittle Solids Containing Small Cracks Under Compressive Stress States," Acta Metall., Vol.34, pp.497-510.

Barnes, P.B., Tabor, D. and Walker, J.C.F. (1971), "The Friction and Creep of Polycrystalline Ice," Proc. Roy. Soc. London, Series A, pp.127-155.

Biot, M.A. (1954), "Theory of Stress-Strain Relation in Anisotropic Viscoelasticity and Relaxation Phenomena", J. Appl. Mech. Vol.25, pp.1385-91.

Bridgman, P.W. (1950), "The Thermodynamics of plastic Deformation and Generalized Entropy", Reviews of Modern Physics, Vol.22, pp.56-63.

Budiansky, B. (1965), "On the Elastic Moduli of Some Heterogeneous Materials," J. Mech. Phys. Solids, Vol.13, pp.223-227.

Budianski, B., and O'Connell, R.J. (1976), "Elastic Moduli of Cracked Solid," Int. J. Solids Structures, Vol.12, pp.81-97.

Budiansky, B., Hutchinson, J.W., and Slutsky, S. (1982), "Void Growth and Collapse in Viscous Solids," in mechanics of Solids, The Rodeny Hill 60th Anniversary Volume, Pergamon Press. 13-45.

Carroll, M., and Holt, A.C. (1972), "Static and Dynamic Pore-Collapse Relations for Ductile Porous Materials," J. Applied Physics, Vol.43, pp.1626-36.

Chen, I.W., and Orgon, A.S. (1979), "Steady State Power-Law Creep in Heterogeneous Alloys with Coarse Microstructures," Acta Metallurgica, Vol.27, pp.785-91.

Christensen, R.M. (1979), "Mechanics of Composite Materials," John Wiley & Sons.

Christensen, R.M. (1990), "A Critical Evaluation of Micromechanics Models," J. Mech. Phys. Solids, Vol.38, pp.379-404.

Christensen, R.M., and Lo, K.H. (1979), J. Mech. and Phys. of Solids, Vol.27, pp.315, Erratum, Vol.34, pp.639.

Christofferson, J., Mehrabadi, M.M. and Nemat-Nasser, S. (1981), "A Micromechanically Based Description of Granular Material Behaviour," J. Applied Mechanics. Vol.48, pp.339-344.

Cocks, A.C.F. (1989), "Inelastic Deformation of Porous Materials," J. Mech. Phys. Solids, Vol.37, pp.693-715.

Cocks, A.C.F., and Leckie, F.A. (1987), "Creep Constitutive Equations for Damaged Materials," Advances in Applied Mechanics, Vol.25, pp.239-294.

Coleman, B.D., and Gurtin, M.E. (1967), "Thermodynamics with Internal State Variables," J. Chemi. Phy Vol.47, pp.597-613.

Cowin, S.C. (1978), "Microstructural Continuum Models for Granular Materials," Proc. US-Japan Seminar on Continuum Mechanical and Statistical Approaches in the Mechanics of Granular Materials, Gakujutsu Bukyukai, Tokyo, Japan, pp.162-170.

DiMaggio, F.L., and Sandler, I.S. (1971), "Material Model for Granular Soils," J. Engr. Mech., ASCE, Vol.97, pp.935-950.

Dougill (1976), "On Stable Progressively Fracturing Solids," J. Applied Mathematics and Physics, ZAMP, Vol.27, pp.423-437.

Duva, J.M., and Hutchinson, J.W. (1984), "Constitutive Potentials for Dilutely Voided Nonlinear Materials," Mechanics of Materials, Vol.3, pp.41-54.

Duval, P., Ashby, M.F., and Anderman, I. (1983), "Rate-Controlling Processes in the Creep of Polycrystalline Ice," J. Phys. Chem., Vol.87, pp.4066-74.

Duthinh, D. (1992), "Pressure of Crushed Ice as Mohr-Coulomb Material Against Flat, Axisymmetric Indentor," J. of Cold Regions Engineering, Vol.6, pp.139-151.

Eshelby, J.D. (1957), "The Determination of Elastic Field of an Ellipsoidal Inclusion, and Related Problem," Proc. Royal Society, London, A241, pp.376-396.

Elliott, G.M. and Brown, E.T. (1985), "Yield of a Soft, High Porosity Rock," Geotechnique, Vol.35, pp.413-423.

Feda, J. (1982), "Mechanics of Particulate Materials The Principles," Elsevier.

Findley, W.N., Lai, J.S., and Onaram, K. (1976), "Creep and Relaxation of Nonlinear Viscoelastic Material," North-Holland Publishing Company.

Finn, D., Jordaan, I.J., Singh, S.K. and Spencer, P. (1989), "Flow of Crushed Ice: Physical and Mechanical Properties and Behaviour, Vol.2: Analysis of Data." Ocean Engineering Research Centre, Memorial University of Newfoundland. 60p.

Frederking, R.M.W., Jordaan, I.J., and McCallum, J.S. (1990), "Field Tests of Ice Indentation at Medium Scale, Hobson's Choice Ice Island," Proc. 10th IAHR Symposium on Ice, Espoo, Finland, Vol.2, pp.931-944.

Fukue, M.F. (1979), "Mechanical Performance of Snow Under Loading," Tokai University Press, Japan.

Fung, Y.C. (1965), "Foundations of Solid Mechanics," Prentice-Hall.

Gagnon, R.E., and Sinha, N.K. (1991), "Energy Dissipation Through Melting in Large Scale Indentation Experiments on Multi-Year Sea Ice," Proc. OMAE, Vol.IV, pp.157-161.

Gale, A.D., Wong, T.T., Sego, D.C. and Morgenstern, N.R. (1987) "Stress- Strain Behaviour of Cohesionless Broken Ice," 9th International Conference on Port and Ocean under Arctic Condition. Vol.3, pp.109-119.

Green, A.E., and Rivlin, R.S. (1957), "The Mechanics of Nonlinear Material with Memory, Part I," Archive of Rational Mechanics and Analysis, Vol.1, pp.1.

Hallam, S.D., Pickering, J.G. (1988), "Modelling of Dynamic Ice Loading of Offshore Structures," Proc., Int. Conf. on Tech. for Polar Areas, POLARTECH88, Vol.1, pp.235-248.

Hashin, (1962), "The Elastic Moduli of Heterogeneous Materials," J. Applied Mechanics, pp.143-150.

Hashin, (1983), "Analysis of Composite Materials," J. Applied Mechanics, Vol.50, pp.481.

Hansen, A.C. and Brown, R.L. (1986), "The Granular Structure of Snow: An Internal State Variable Approach," J. Glaciology, Vol.32, pp.434-438.

Hansen, A.C. and Brown, R.L. (1988), "An Internal State Variable Approach to Constitutive Theories for Granular Materials with Snow as an Example," Mechanics of Material, Vol.7, pp.109-119.

Hill, R. (1965), "A Self-Consistent Mechanics of Composite Materials," J. Mech. Phys. Solids, Vol.13, pp.213-222.

Horii, H., and Nemat-Nasser, S. (1983), "Overall Moduli of Solids with Microcracks: Load-Induced Anisotropy," J. Mech. Phys. Solids, Vol.31, pp.155-171.

Johnson, J.N., and Green, S.J. (1976), "The Mechanical Response of Porous Media Subjected to Static Loads," The Effect of Voids on the Material Deformation, ASME. AMD Vol.16, pp.93-123.

Jones, S.J. (1982), "The Confined Compressive Strength of Polycrystalline Ice," J. Glaciology, Vol.28, pp.171-177.

Jones, S.J., and Chew, A.M. (1983), "Creep of Ice as a Function of Hydrostatic Pressure," J. Phys. Chem., Vol.87, pp.4064-66.

Jordaan, I.J. and McKenna, R.F. (1988), "Constitutive Relation for Creep of Ice," Proc., IAHR Ice Symposium, Sapporo, Japan, Vol.III, pp.47-58.

Jordaan, I.J. and McKenna, R.F. (1989), "Modelling of Progressive Damage in Ice," U.S. Army Cold Region Research Laboratory, CRREL Special Report 89-5, pp.125-165.

Jordaan, I.J. and McKenna, R.F. (1991), "Progress of Deformation and Fracture of Ice in Compression," in Ice-Structure Interaction, Springer-Verlag, Berlin, pp.283-309.

Jordaan, I.J. and Timco, G.W. (1988), "Dynamics of the Ice Crushing Process," J. of Glaciology, Vol.34, pp.318-326.

Jordaan, I.J., Kennedy, K.P., Mckenna, R.F. and Maes, M.A. (1991), "Loads and Vibration Induced by Compressive Failure of Ice," Proc. Sixth International Specialty Conference on Cold Region Engineering, ASCE, pp.638-649.

Jordaan, I.J., Stone, B.M., McKenna, R.F. and Fuglem, M.K. (1992), "Effect of Microcracking on the Deformation of Ice," Canadian Geotechnical J., Vol.29, pp.143-150.

Kalifa, P., Duval, P. and Ricard, M. (1989), "Crack Nucleation in Polycrystalline Ice Under Compressive Stress States," OMAE 89.

Kestin, J., and Rice, J.R. (1970), "Paradoxes in the Application of Thermodynamic to Constrained Solids," in Critical Review of Thermodynamics, Mono Book Corp., Baltimore, pp.275-299.

Kolymbas, D., and Wu, W. (1990), "Recent Results of Triaxial Tests with Granular Materials," Powder Technology, Vol.60, pp.99-119.

Krajcinovic, D. (1989), "Damage Mechanics," Mechanics of Materials, Vol.8, pp.117-197.

Kurdyumov, V.A. and Kheisin, D.E. (1976), "Hydrodynamic Model of the Impact of a Solid on Ice," Prikladnaya Mekhanika, Vol.12, pp.103-109.

Lade, P.V. (1988), "Effect of Void and Volume Changes on the Behaviour of Frictional Materials," Int. J. Num. Anal. Meth. Geom, Vol.12, pp.351-370.

Laws, N., and Brockenbrough, J.R. (1987), "The Effect of Micro-Crack Systems on the Loss of Stiffness of Brittle Solids," J. Mech. Phys. Solids, Vol.23, pp.1247-68.

Leckie, F.A. (1978), "The Constitutive Equations of Continuum Creep Damage Mechanics," Phil. Tran. Royal Soc., London, Series A, Vol.288, pp.27-47.

Mackenzie, J.K. (1950), "The Elastic Constants of a Solid Containing Spherical Holes," Proc. Phys. Soc. Lon., B, Vol.63, pp.2-11.

Maeno, N. and Ebinuma, T. (1983), "Pressure Sintering of Ice and its Implication to the Densification Snow at Polar Glaciers and Ice Sheets," J. Phy. Chemi, Vol.87, pp.4103-4110.

Malvern, L.E. (1969), "Introduction to the Mechanics of a Continuous Media," Prentice-Hall.

McCormick, P.G. and Ruoff, A.L. (1971), "Creep Under High Pressures," Chapter 8 in Mechanical Behaviour of Materials Under Pressure, edited by H.Ll.D. Pugh, Applied Science Publishers, pp.355-390.

Mclean, D. (1957), Grain Boundaries in Metals, Oxford at the Clarendon press.

Mehrabadi, M.M., Nemat-Nasser, S. (1983), "Stress, Dilatancy and Fabric in Granular Materials," Mechanics of Materials. Vol.2, pp.155-161.

Mroz Z. (1980), "Deformation and Flow of Granular Materials," Proc. International Union of Theoretical and Applied Mechanics Conference, pp.119-132.

Mura, T. (1982), "Micromechanics of Defects in Solids," Martinus Nijhoff Publishers.

Nemat-Nasser, S. (1989), "Compression-Induced Ductile Flow of Brittle Materials and Brittle Fracture of Ductile Materials," Proc. 12th Int. Congress of Applied Mechanics, CANCAM 89, Ottawa, pp.10-21.

Nemat-Nasser, S. and Mehrabadi, M.M. (1984), "Micromechanically Based Rate Constitutive Description of Granular Materials," in Mechanics of Engineering Materials, eds. C.S. Desai and R.H. Gallagher, John Wiley & Sons. pp.451-463.

Oda, M. (1972), "The Mechanics of Fabric Changes During Compressional Deformation of Sand," Soil and Foundation Vol.12, pp.45-63.

Oda, M., Konishi, J. and Nemat-Nasser, S. (1980), "Some Experimentally Based Fundamental Results on the Mechanical Behaviour of Granular Materials," Geotechnique, Vol.30. pp.476-495.

Perla, R. (1982), "Preparation of Section Planes in Snow Specimens," J. of Glaciology, Vol.28, pp.199-204.

Raju. V.S., Sadasivam, S.K., and Venkataraman, M. (1972), "Use of Lubricated and Conventional End Platens in Triaxial Tests of Sands," Soils and Foundations, Vol.12, pp.35-43.

Rice J.R. (1968), "Mathematical Analysis in the Mechanics of Fracture," Fracture: An Advanced Treatise, Vol.II, pp.191-310.

Rice, J.R. (1971), "Inelastic Constitutive Relations for Solids: An Internal- Variable Theory and Its Application to Metal Plasticity," J. Mech. Phys. Solids, Vol.19, pp.433-455.

Rice, J.R. (1975), "Continuum Mechanics and Thermodynamics of Plasticity in Relation to Micro-scale Deformation Mechanism," in Constitutive Equations in Plasticity, ed. A.S. Argon, MIT Press, Cambridge, MA. pp.23-79.

Rice, J.R. (1978), "Thermodynamics of Quasi-Static Growth of Griffith Cracks," J. Mech. Phys. Solids, Vol.26, pp.289-366.

Rigsby, G.P. (1958), "Effect of Hydrostatic Pressure on Velocity of Shear Deformation of Single Ice Crystals," J. Glaciology, Vol.3, pp.271-278.

Rowe, R.W. (1962), "The Stress-Dilatancy Relation for Static Equilibrium of an Assemblage of Particles in Contact," Proc. Roy. Soc. London,Series A, Vol.259, pp.500-527.

Savage, S.B., Sayed, M. and Frederking, R.M.W. (1992), "Two-Dimensional Extrusion of Crushed Ice. Part 2: Analysis," Cold Reg. Sci. Technol., Vol.21, pp.37-47.

Sayed, M. and Frederking, R.M.W. (1992), "Two-Dimensional Extrusion of Crushed Ice. Part 2: Experimental," Cold Reg. Sci. Technol., Vol.21, pp.25-36.

Schapery, R.A. (1969), "Further Development of a Thermodynamic Constitutive Theory: Stress Formulation," Purdue University, Report No. AA & ES.69-2. 48p.

Schapery, R.A. (1969), "On the Characterization of Nonlinear Viscoelastic Materials," Polymer Engineering and Science, Vol.9, pp.295-310.

Schapery, R.A. (1981), "On Viscoelastic Deformation and Failure Behaviour of Composite Materials with Distributed Flaws," Advances in Aerospace Structures and Materials, ASME, AD-01, pp.5-20.

Schapery, R.A. (1984), "Correspondence Principle and a Generalized *J* Integral for Large Deformation and Fracture Analysis of Viscoelastic Media," Int. J. Fracture, Vol.25, pp.195-223.

Schapery, R.A. (1986), "Time-Dependent Fracture: Continuum Aspect of Crack Growth," Encyclopedia of Materials Science and Engineering, Vol.7, pp.5043-53.

Schapery, R.A. (1990), "A Theory of Mechanical Behaviour of Elastic Media with Growing Damage and Other Changes in Structure," J. Mech. Phys. Solids, Vol.38, pp.215-253.

Schapery, R.A. (1990a), "Analysis of Damage Growth in Particulate Composite Materials," Microcracking Induced Damage in Composites, AMD Vol.111, pp.55-64.

Schapery, R.A. (1991), Models for the Deformation Behaviour of Viscoelastic Media with Distributed Damage and their Applicability to Ice," in Ice-Structure Interaction, Springer-Verlag, Berlin, pp.191-249.

Schofield, A.N., and Wroth, C.P. (1968), "Critical State Soil Mechanics," McGraw-Hill.

Schulson, E.M. (1990), "The Brittle Compressive Fraction of Ice," Acta Metall. Mater., Vol.38, pp.1963-76.

Singh, S.K., Timco, G.W., Frederking, R. and Jordaan, I.J. (1990), "Tests of Ice Crushing on a Flexible Structure," International Conference on Offshore Mechanics and Arctic Engineering, Houston, Vol.IV, pp.89-94.

Singh, S.K., Jordaan, I.J., Xiao, J., and Spencer, P.A. (1993), "The Flow Properties of Crushed Ice," Proc. International Conference on Offshore Mechanics and Arctic Engineering, Glasco, U.K., Vol.4, pp.11-19.

Sinha, N.K. (1989), "Microcrack-Enhanced Creep in Polycrystalline Material at Elevated Temperature," Acta Mechanica, Vol.37, pp.3107-18.

Spencer, P.A., Masterson. D.M.. Lucas, J. and Jordaan, I.J. (1992), "The Flow Properties of Crushed Ice I : Experimental Observation and Apparatus," Proc. Symposium on Ice, Int. Association of Hydraulics Research, Vol.I, pp.158-168.

Standler, E., Frederking, R.M.W., Jordaan, I.J., Sinha, N.K. (1993), "Structure and Texture of Failure Zone in Medium-Scale Indentation," under preparation.

Steel, A., Morin, P.J., and Clark, J.I. (1991), "Behaviour of Laboratory-Made Spray Ice in Triaxial Compression Testing," J. Cold Regions Engineering, ASCE, Vol.4, pp.192-204.

Stone, B.M., Jordaan, I.J., Jones, S.J. and McKenna, R.F. (1989), "Damage of Isotropic Polycrystalline Ice under Moderate Confining Pressures," Proc. 10th Int. Conf. on Port and Ocean Engineering under Arctic Conditions, Luea, Sweden, Vol.1, pp.408-119.

Vesic, A.S., and Clough, G.W. (1968), "Behaviour of Granular Materials Under High Pressure," J. Soil Mech. Foundations, ASCE, Vol.94, pp.661-668.

Weertman, J. (1969), Trans. Am. Soc. Metals, Vol.62, pp.502.

Wilkinson, D.S., and Ashby, M.F. (1975), "Pressure Sintering by Power-Law Creep," Acta Metallurgica, Vol.23, pp.1277-85.

Xiao, J., Jordaan, I.J., Singh, S.K. (1992), "Pressure Melting and Friction in Ice-Structure Interaction," Proc. Symposium on Ice, Int. Association of Hydraulics Research, to be published in volume 3.

Appendix A

Photographs of Samples

The photographs of samples after a test are presented here. The test number and the scale are shown. For the detail information about type of sample and the loading history see Table 3.1.


Test 3
1 cm

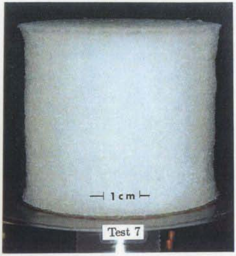
1 cm
Test 7

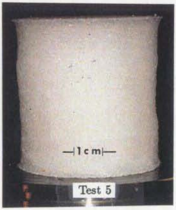
1 cm
Test 5

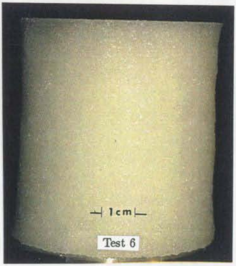
1 cm
Test 6

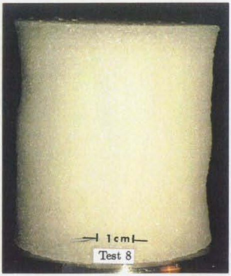

1cm
Test 8

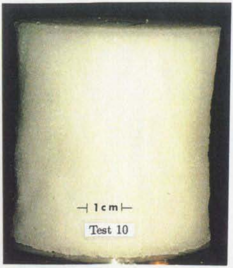

1cm
Test 10

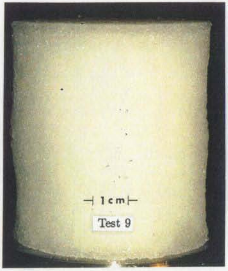

1cm
Test 9

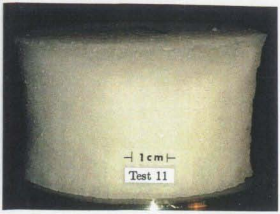

1cm
Test 11


1cm
Test 12

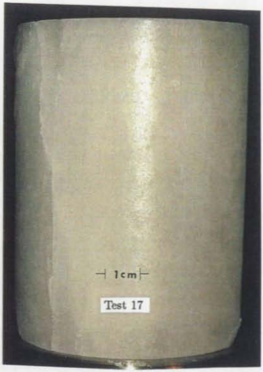
1cm
Test 17

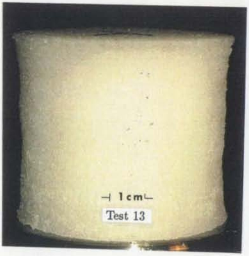
1cm
Test 13

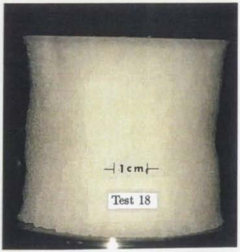
1cm
Test 18

Appendix B

Effective Moduli of Composites

The elastic properties of composites are dependent on the elastic properties and the volume fractions of the matrix and the particulate phases. The geometric features of the microstructure can be the crystal grain structure in polycrystalline materials, where each grain is anisotropic and different grains have different orientations, or, ellipsoidal-shaped inclusions embedded in a continuous matrix phase as in composites. The microcracks can be considered as ellipsoidal inclusions where one dimension is very small. In porous materials, the inclusion phase has no stiffness.

A review of various micromechanical models is presented in Christensen (1979, 1990), Mura (1982) and Hashin (1983). These are the composite-sphere method (Hashin, 1962), the self-consistent methods (Budiansky, 1965; Hill, 1965), the generalized self-consistent method (Christensen and Lo, 1979) and equivalent inclusion methods (Eshelby, 1957; Mura, 1982). For dilute composites, these methods give similar results; while for high concentration composites, the generalized self-consistent method provides the best performance. For dilutely porous materials, such as compacted crushed ice, any of these methods is expected to provide good results. The equivalent inclusion method is selected for its simplicity of computation and is discussed in detail. The concepts used in the self-consistent methods and the generalized self-consistent methods are also summarized. The concept of equivalent homogeneity, which is common to these models, is described first.

B.1 Equivalent Inclusion Method

The equivalent inclusion method is based on Eshelby's (1957) solution for a uniformly stressed infinite continuum containing an ellipsoidal inclusion. The stress disturbance in the applied stress due to the inclusion is obtained by solving an equivalent homogeneous problem.

For the problem of a composite material in which the particulate phases are surrounded by a homogeneous matrix, each particulate phase is considered to be an isolated ellipsoidal inclusion. The interaction of inclusions is neglected in this approach. The geometry of the inclusion problem is shown in Figure B.1a, where an infinite material M of elastic modulus C^M_{ijkl} contains an ellipsoidal inclusion I of elastic modulus C^I_{ijkl}. The external applied stress $\bar{\sigma}_{ij}$ and the resulting strain $\bar{\epsilon}_{ij}$ are related by Hooke's Law. Due to the inclusion I, a stress disturbance σ_{ij} and corresponding strain ϵ_{ij} develops in the matrix and varies from place to place. The total stress and strain are

$$\text{total stress} = \bar{\sigma}_{ij} + \sigma_{ij} \tag{B.1}$$

$$\text{total strain} = \bar{\epsilon}_{ij} + \epsilon_{ij} \tag{B.2}$$

respectively. In Figure B.1, the concept of this decomposition is also shown. The stress components σ_{ij} are in self-equilibrium and vanish at the outer boundary:

$$\partial\sigma_{ij,j} = 0 \tag{B.3}$$

This condition ensures non-interaction of inclusions.

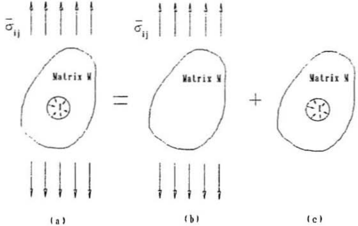

Figure B.1: Micro-structural model and the decomposition scheme.

Hooke's law is written for inclusion and matrix as,

$$\bar{\sigma}_{ij} + \sigma_{ij} = C^{I}_{ijkl}(\bar{\epsilon}_{kl} + \epsilon_{kl}) \quad \text{in } I \tag{B.4}$$

$$\bar{\sigma}_{ij} + \sigma_{ij} = C^{M}_{ijkl}(\bar{\epsilon}_{kl} + \epsilon_{kl}) \quad \text{in } M \tag{B.5}$$

Now an equivalent problem is created by imaginary cutting, straining and welding operation as described by Eshelby (1957) in an infinitely extended homogeneous matrix with elastic moduli C^{M}_{ijkl}. Cut and remove the domain I from this matrix. Allow the unconstrained transformation to take place, then apply surface traction on the domain I to restore its original shape, put back the domain I in the hole and weld it. Finally an equal and opposite body force is applied to balance the surface traction. When this material is subjected to the applied strain $\bar{\epsilon}_{ij}$, an arbitrary homogeneous strain $\epsilon_{ij}{}^{*}$ is created in the inclusion I due to constraint imposed by the surrounding matrix. Mura (1982) has given this strain a generic name eigenstrain. This strain in not related to any elastic deformation. The resulting total stress and total strain are $\bar{\sigma}_{ij} + \sigma_{ij}$ and $\bar{\epsilon}_{ij} + \epsilon_{ij}$ respectively, while the elastic strain is $\bar{\epsilon}_{ij} + \epsilon_{ij} - \epsilon^{*}_{ij}$ in I. Hooke's law yields,

$$\bar{\sigma}_{ij} + \sigma_{ij} = C^M_{ijkl}(\bar{\epsilon}_{kl} + \epsilon_{kl} - \epsilon^*_{kl}) \text{ in } I \tag{B.6}$$

$$\bar{\sigma}_{ij} + \sigma_{ij} = C^M_{ijkl}(\bar{\epsilon}_{kl} + \epsilon_{kl}) \text{ in } M \tag{B.7}$$

The necessary and sufficient condition for the equivalency of the stress and strain in the above two set of problems is

$$C^I_{ijkl}(\bar{\epsilon}_{kl} + \epsilon_{kl}) = C^M_{ijkl}(\bar{\epsilon}_{kl} + \epsilon_{kl} - \epsilon^*_{kl}) \text{ in } I. \tag{B.8}$$

The strain ϵ_{ij} is related to the eigenstrain $\epsilon_{ij}{}^*$ by Eshelby's tensor S_{ijkl} as

$$\epsilon_{ij} = S_{ijkl}\epsilon^*_{kl}. \tag{B.9}$$

The quantities S_{ijkl} are dependent on the geometry of the inclusions. This is the strain equivalent of the stress concentration factor. Using Equation B.8 and B.9, the eigenstrain $\epsilon_{ij}{}^*$ can be obtained as,

$$\epsilon_{ij}{}^* = \frac{C^M_{ijkl} - C^I_{ijkl}}{g}\bar{\epsilon}_{kl}, \tag{B.10}$$

where the scalar

$$g = \delta_{ik}\delta_{jl}C^M_{ijkl} + S_{ijkl}(C^I_{ijkl} - C^M_{ijkl}). \tag{B.11}$$

The total stress $\bar{\sigma}_{ij} + \sigma_{ij}$ and total strain $\bar{\epsilon}_{ij} + \epsilon_{ij}$ in the inclusion I can be calculated by substituting Equation B.10 in Equation B.8, and using Equations B.4 and B.5:

$$\bar{\sigma}_{ij} + \sigma_{ij} = \frac{C^M_{ijkl}C^I_{ijkl}}{g}\bar{\epsilon}_{ij} \tag{B.12}$$

$$\bar{\epsilon}_{ij} + \epsilon_{ij} = \frac{C^M_{ijkl}}{g}\bar{\epsilon}_{kl} \tag{B.13}$$

The averaged stresses in the representative volume V can be written as

$$\bar{\sigma}_{ij} = \frac{1}{V}\int_V(\bar{\sigma}_{ij} + \sigma_{ij})dV = \frac{1}{V}\int_I(\bar{\sigma}_{ij} + \sigma_{ij})dV + \frac{1}{V}\int_M(\bar{\sigma}_{ij} + \sigma_{ij})dV. \tag{B.14}$$

Substituting Equation B.12 in this equation, total stress is obtained as

$$\bar{\sigma}_{ij} = c\,\frac{C^M_{ijkl}C^I_{ijkl}}{g}\bar{\epsilon}_{ij} + (1-c)\bar{\sigma}^M_{ij}, \tag{B.15}$$

where c is the volume fraction of the inclusion, and $\bar{\sigma}^M_{ij}$ is average stress in the matrix. Similarly, total strain is obtained as

$$\bar{\epsilon}_{ij} = c\,\frac{C^M_{ijkl}}{g}\bar{\epsilon}_{kl} + (1-c)\bar{\epsilon}^M_{ij}, \tag{B.16}$$

where $\bar{\epsilon}^M_{ij}$ is averaged strain in the matrix M and is related to average stress in the matrix by Hooke's law as

$$\bar{\sigma}^M_{ij} = C^M_{ijkl}\bar{\epsilon}^M_{kl}. \tag{B.17}$$

Eliminating $\bar{\sigma}^M_{ij}$ and $\bar{\epsilon}^M_{ij}$ from Equations B.15 and B.16 using Equation B.17, averaged stress $\bar{\sigma}_{ij}$ is

$$\bar{\sigma}_{ij} = C_{ijkl}\bar{\epsilon}_{kl} = C^M_{ijkl}\left[1 + \frac{c}{g}\delta_{ik}\delta_{jl}(C^I_{ijkl} - C^M_{ijkl})\right]\bar{\epsilon}_{kl} \tag{B.18}$$

or,

$$\frac{C_{ijkl}}{C^M_{ijkl}} = 1 + \frac{\delta_{ik}\delta_{jl}(C^I_{ijkl} - C^M_{ijkl})c}{\delta_{ik}\delta_{jl}C^M_{ijkl} + S_{ijkl}(C^I_{ijkl} - C^M_{ijkl})} \tag{B.19}$$

This equation can be specialized for various geometries of inclusions, such as spherical inclusions, penny-shaped inclusions and cylindrical inclusions.

B.2 Self-Consistent Methods

For elastic composite and polycrystalline materials self-consistent methods (Budiansky, 1965; Hill, 1965) provide an approximate but reliable estimate of bulk and shear moduli. Budianski and O'Connell (1976) have presented a self-consistent formulation to include microcracks. This method is similar to the equivalent inclusion method and is based on Eshelby's (1957) solution for a uniformly stressed infinite continuum containing an ellipsoidal inclusion.

In the case of the problem of a composite material in which the particulate phases are surrounded by an effective and homogeneous matrix, each particulate phase is considered to be an isolated ellipsoidal inclusion. The inclusion is assigned the properties and orientation of the particulate phase and the matrix properties coincides with that of the composite material. Such mapping of the composite material is possible as the mean stress and displacements at its boundary are equal to those at the boundary of the equivalent idealized continuum. The consistency condition refers to unchanged density and displacement at the outer boundary. Following the steps in Section B.1, a solution for the elastic moduli can be found as

$$\frac{C_{ijkl}}{C^M_{ijkl}} = 1 + \frac{C_{ijkl}}{C^M_{ijkl}} \left[\frac{(C^I_{ijkl} - C^M_{ijkl})c}{C^M_{ijkl} + S_{ijmn}(C^I_{mnkl} - C_{mnkl})} \right] \tag{B.20}$$

Unlike Equation B.19, B.20 has the moduli of the composite in the right side also, thus it forms a coupled set of equations. In isotropic materials, this requires that the bulk modulus of the composite should be known to obtain the shear modulus. For rigid inclusions and for the constant ratio of bulk to shear modulus (a constant Poisson's ratio of 1/5), a uncoupled set of equations is obtained.

For spherical pores a closed-from solution for Eshelby's tensor S_{ijkl} is given by Mura (1982) as

$$S_{1111} = S_{2222} = S_{3333} = \frac{7 - 5\nu^M}{15(1 - \nu^M)}, \tag{B.21a}$$

$$S_{1122} = S_{2233} = S_{3311} = S_{1133} = S_{2211} = S_{3322}, = \frac{5\nu^M - 1}{15(1 - \nu^M)}, \tag{B.21b}$$

$$S_{1212} = S_{2323} = S_{3131} = \frac{4 - 5\nu^M}{15(1 - \nu^M)}. \tag{B.21c}$$

Other components of S_{ijkl} are zero.